

Microstructure and deformation of two-phase γ -titanium aluminides

F. Appel*, R. Wagner

Institute for Materials Research, GKSS-Research Center, D-21502 Geesthacht, Germany

Accepted 5 September 1997

Abstract

During the past decade considerable research efforts have been directed towards achieving balanced engineering properties of two-phase γ -titanium aluminide alloys for future applications as structural materials. For optimization of mechanical properties such as yield and creep strengths, tensile ductility and fracture resistance, a basic understanding of the temperature dependent micromechanisms of plasticity and fracture, and their interplay with various microstructural constituents is required. In this review article, the current knowledge on dislocation types and slip systems, the development of deformation substructures, factors controlling the mobility and multiplication of dislocations, interface related plasticity, solid solution and precipitate strengthening mechanisms as well as microscopic aspects of creep and fracture will be addressed. These topics will be related to specific microstructures and associated engineering properties. © 1998 Elsevier Science S.A. All rights reserved.

Keywords: Two-phase γ -titanium aluminides; Microstructure; Deformation

1. Introduction

The increasing demand for better fuel economy, higher operating efficiency, and for the related reduction of CO, CO₂ and NO_x emission in automotive engines as well as in industrial and in aviation gas turbines has prompted intensive search for weight-saving structural materials with higher operational temperature capabilities [1–5]. In this context, γ -titanium aluminides γ (TiAl) are considered as top candidate materials being on the verge for high-temperature structural use [6–14]. This is essentially due to some attractive properties such as low density ($\rho \sim 3.8 \text{ g/cm}^3$), high specific strength σ/ρ (Fig. 1a), high specific stiffness E/ρ (Fig. 1b), high temperature strength retention, and resistance against ‘titanium fire’.

According to the binary Ti-Al phase diagram (Fig. 2) [15] γ (TiAl) can solidify in a single phase state only when the Al content exceeds ~53 at.%, i.e., the composition of the peritectic point at which the peritectic reaction $L + \alpha \rightarrow \gamma$ takes place. Like many intermetallic phases, at room temperature single phase γ (TiAl) suffers also from both poor ductility (i.e., tensile fracture strains) and poor fracture toughness. Because of these inherent shortcomings no effort has been made to develop structural materials on the basis of single phase γ (TiAl).

In contrast, considerably improved ductility and toughness can be achieved in two-phase alloys with compositions in the ($\gamma + \alpha$) two-phase region of the phase diagram (Fig. 2) [16,17]. Thus, during recent years extensive research has been carried out to develop two-phase γ (TiAl) based alloys consisting of γ (TiAl) (face-centered tetragonal L1₀ structure, Fig. 3a) and α_2 -Ti₃Al (hexagonal DO₁₉ structure, Fig. 3b) for structural applications. The objective has essentially been to achieve balanced

* Corresponding author.

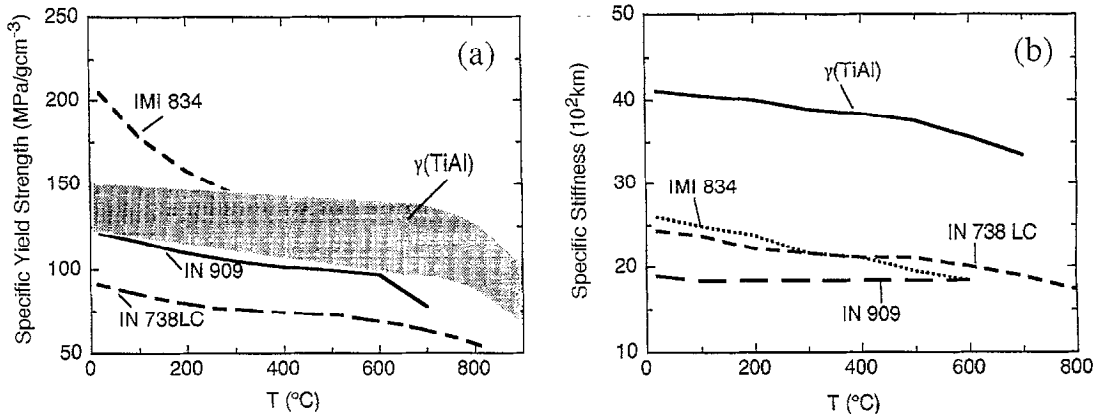


Fig. 1. Variation of the specific yield strength (a), and the specific stiffness (b) with temperature of typical two-phase γ alloys in comparison with a low expansion iron based alloy (IN 909), a nickel based super alloy (IN 738 LC), and a conventional titanium alloy (IMI 834) [14].

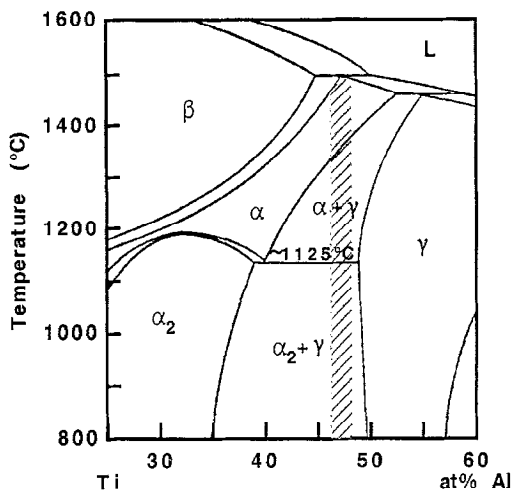


Fig. 2. Central portion of the binary Ti-Al phase diagram [15] showing the compositional ranges (hatched) for two-phase engineering materials.

mechanical properties such as ductility, tensile strength, toughness, and creep strength via improved alloy chemistry and microstructural control [12–14].

Among other intermetallic alloys currently being considered for structural applications, the phase diagram of Ti-Al is unique: An alloy with near-equiatomic composition, i.e., Al contents ranging from ~46 to ~49 at.%, (concentrations are given in at.% throughout this article) passes through three different phase fields, when heated beyond 1000°C, i.e., $\alpha_2 + \gamma \rightarrow \alpha + \gamma \rightarrow \alpha$, with the α single-phase field extending up to 1470°C. Thus, a vast variety of different microstructures can be generated (cf. Section 2) depending on the processing technology, and on the particular phase field chosen for the heat-treatments [11,12].

In the recently emerging class of γ Ti(46–48)Al based alloys with about 2% additions of Nb and about 2% of some other elements (e.g., Cr, Mn, W, Ta, Si, B), microstructures can be established which lead to tensile ductilities as high as 4% at room temperature [12,18]. However, as will be outlined in Section 3, microstructures offering acceptable ductilities, often show poor toughness ($K_{Ic} \sim 10$ MPa \sqrt{m}) and reduced creep strength whereas microstructures with both improved toughness

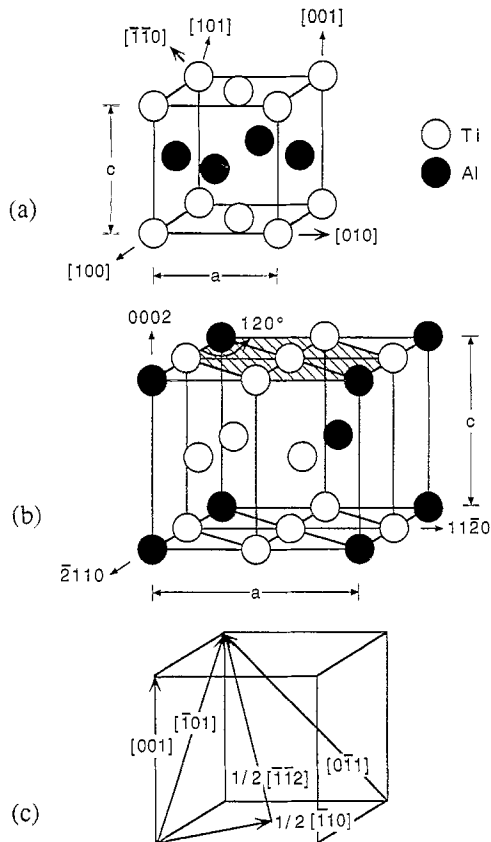


Fig. 3. Atomic arrangement (a) in the ordered face-centered tetragonal (fct) $L1_0$ structure of γ (TiAl) and (b) in the ordered hexagonal DO_{19} structure of α_2 -Ti₃Al. (c) Burgers vectors of ordinary $1/2\langle 110 \rangle$ and $\langle 001 \rangle$ dislocations and of $1/2\langle 112 \rangle$ and $\langle 011 \rangle$ superdislocations.

(~ 30 MPa \sqrt{m}) and creep strength lead to unsatisfactory ductilities [12–14]. This *inverse correlation* between tensile properties and resistance to fracture renders microstructural optimization for achieving balanced engineering properties to be very difficult and not yet fully accomplished. This is in contrast to most materials, where the micromechanisms of brittle failure are usually expressed in both tensile ductility and fracture toughness. It may be taken as an indication that the response of two-phase γ (TiAl) to an applied load is controlled by a rather complex microstructure-dependent interplay between the micromechanisms of deformation and the mode of crack generation and propagation. It is the objective of the present article to review some recent advances in the understanding of the micromechanisms of deformation in different microstructures of two-phase γ -based alloys. Reference to single-phase γ -alloys is only made if the body of experimental information contributes to a better mechanistic understanding of the relevant two-phase materials.

The paper is organized such that some important microstructures which can be generated by different processing technologies and subsequent heat-treatments (Section 2) and the related macroscopic tensile properties (Section 3) are briefly discussed. In Section 4, deformation processes which are controlled by the core structure of dislocations are covered before we address to the microprocesses of plasticity (Sections 5 and 6). This involves a discussion of both the thermally activated dislocation glide processes and the dislocation source mechanisms. These processes are related to the limited creep strength of two-phase γ -alloys (Section 8), and also contribute to the strengthening of the material via the interaction of dislocations with grain boundaries, internal boundaries and precipitates (Section

7). The effects of microstructure and crack tip plasticity on the crack growth resistance are discussed in Section 9.

For additional information on the relationship between microstructure and macroscopic properties, reference must be made to some comprehensive review articles (e.g., [12–14,19,20]).

2. Alloy chemistry, processing and microstructures

In this section, the broad variety of different microstructures which can be generated in two-phase γ (TiAl) alloys will be outlined to an extent which is necessary for the discussion of the microstructure-specific deformation as well as the strengthening and fracture mechanisms in Sections 5–9. More detailed descriptions of the microstructure, evolution in cast and in wrought two-phase γ -alloys having different chemistry can be found in, e.g., Refs. [14,19–22], and in Refs. [10–13,23].

2.1. Effects of alloying chemistry on mechanical properties

The effect on the mechanical properties of various ternary additions (X) has been empirically identified in many studies [13,22,24–28]. V, Mn, Mo and Cr generally have been found to increase the ductility, and thus are constituents of all advanced γ -based engineering alloys [11]. At ambient temperatures, Mo, Ta, Nb, V, Cr and Mn were identified to strengthen the γ -phase. Both the refractory elements Ta, Mo, W and carbon are seen to enhance the high temperature strength retention [11,24]. Carbon, however, is only beneficial for improving the creep strength if an appropriate carbide precipitate dispersion has been established through adequate heat-treatments [29–31] (cf. Sections 7 and 8). The addition of ternary solute atoms must be confined to less than 3% in order to avoid the formation of a high volume fraction of the β (B2) TiAl(X) phases [24].

Furthermore, the specific effect of a ternary addition on the properties depends on the Al concentration and on the given microstructure. Therefore, owing to the complex interplay between alloy composition and phase stability, the specific effect that a particular alloying element has on a single property can hardly be separated. Some effects have been compiled that have been identified from experimental studies on the influence of ternary additions and interstitial impurities on the properties of two-phase γ (TiAl(X)) alloys [24].

2.2. Processing and microstructure evolution

Alloys which are currently being considered for engineering applications are processed by conventional techniques including ingot metallurgy [11,18,23,32–35], investment casting [14,21,36–39], and powder metallurgy [40,41]. The as-cast microstructure is usually rather coarse and, depending on the local cooling rate, rather inhomogeneous. It consists of columnar grains which, during solidification grow from the shell of the mold towards the center of the ingot or the component. The prevailing lamellar constituent consisting of γ -TiAl lamellae with interspersed α_2 -Ti₃Al platelets are surrounded by interdendritic Al rich (~54 at.% Al) γ regions (Fig. 4a). As expected from the heat flow during solidification and the ongoing $\alpha \rightarrow \gamma + \alpha_2$ phase transformation (see below), the lamellae are preferentially oriented parallel to the cold shell of the mold, i.e., the lamellar colonies display a pronounced texture. Hot-isostatic pressing (HIP), typically at about 1200°C in the ($\alpha + \gamma$) phase field, is necessary to close the porosity retained from the casting. This leads to a *duplex*—termed ‘D’—microstructure which is composed of the γ grains and lamellae colonies (Fig. 4b), and a few small α_2 precipitates in γ grains. The duplex microstructure, which yields the highest ductility in castings (up to 2% [14,42])

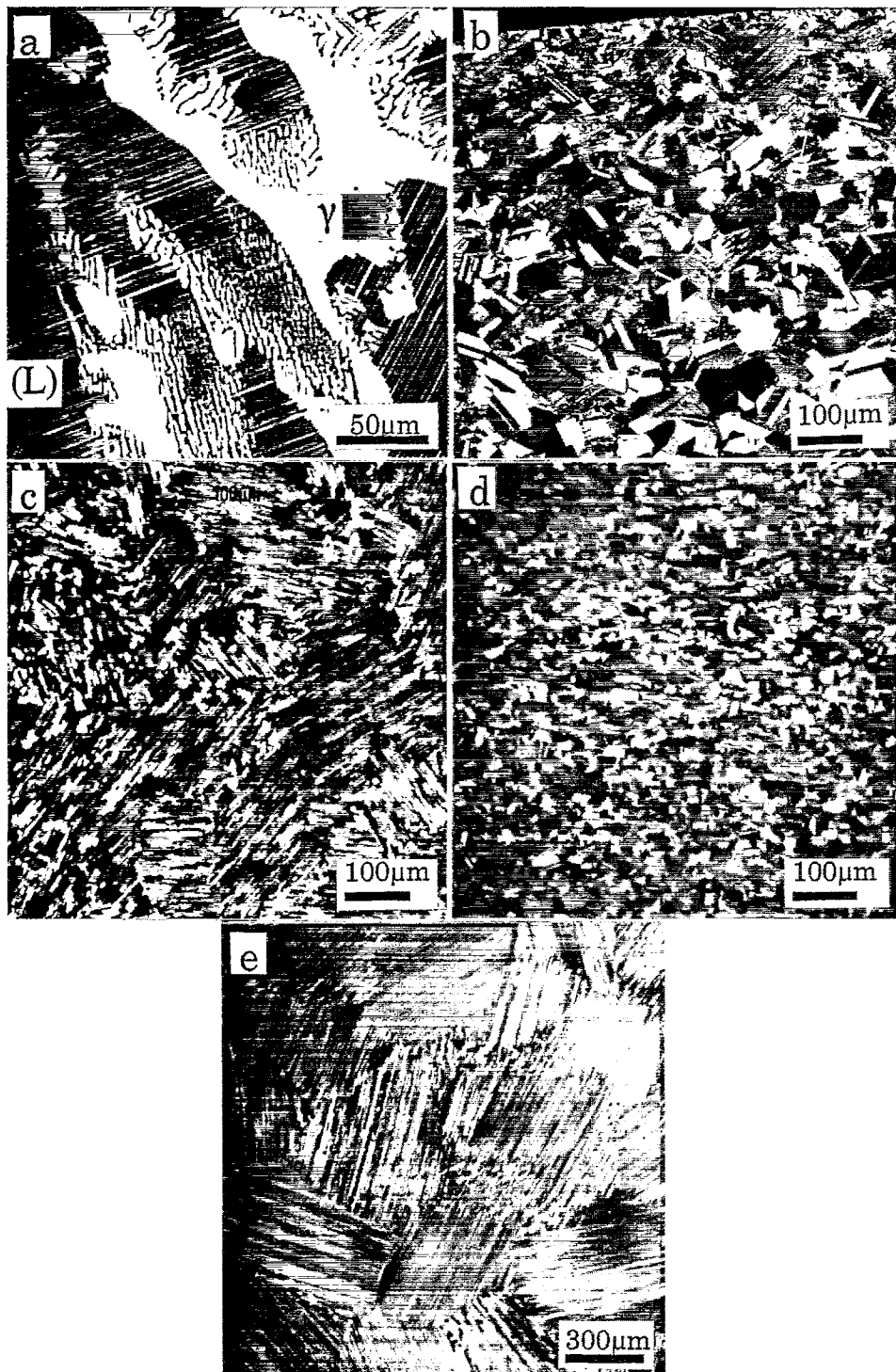


Fig. 4. (a) As-cast microstructure in a 200-kg ingot of Ti-48Al-2Cr. The lamellar ($\gamma + \alpha_2$) regions are surrounded by Al rich interdendritic γ . (b) Duplex microstructure after investment casting and HIP at 1200°C. (c) Nearly-lamellar microstructure in cast and HIPed Ti-47Al-4(Nb, Mn, Cr, Si, B). (d) Near γ (globular) microstructure in Ti-47Al-2Cr-0.2Si after two-step isothermal forging (80% height reduction/step) at 1220°C. Mean grain size $d \sim 10 \mu\text{m}$. (e) Fully-lamellar microstructure. Forged as in (d), followed by a heat-treatment at 1370°C/1 h \rightarrow 900°C/6 h \rightarrow 20°C. Mean grain size $\sim 326 \mu\text{m}$.

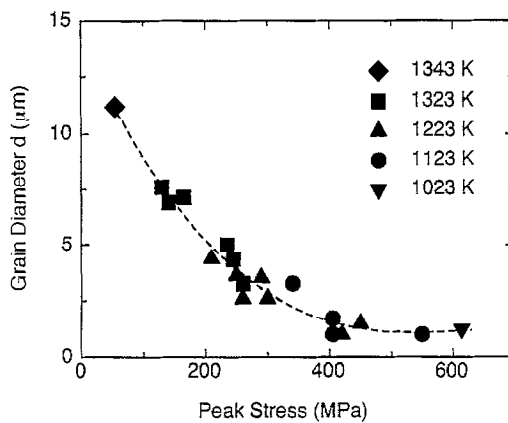


Fig. 5. Variation of grain size with peak stress as obtained from dynamic recrystallization during hot working (after [43]).

but also poorest toughness, can be refined for improved microstructural homogeneity by small additions of B and Si [14,38,39]. In particular, boron proved to be very beneficial for obviating uncontrolled growth of α grains when cast γ -alloys are heat-treated about 10°C below or about 20°C above the α transus temperature T_α (Fig. 2) for generating *nearly-lamellar* (Fig. 4c)—termed ‘NL’—or, respectively, *fully-lamellar* (Fig. 4e)—termed ‘FL’—microstructures upon cooling [11,23]. Fully-lamellar microstructures lead to improved creep strength and fracture toughness but to considerably reduced tensile elongation as compared to duplex microstructures [12,14].

Basically, the same kind of microstructures as observed in differently heat-treated cast material can be generated in wrought material though at a much more refined level, and with considerably improved homogeneity. Thus, wrought processing followed by heat-treatments provides the basis for a controlled microstructural design aiming for improved specific properties and, in particular, balanced properties [12,23,43].

In the ingot metallurgy process, cast ingots are vacuum arc remelted, HIPed and subsequently hot worked in the ($\alpha + \gamma$) phase field by isothermal forging [33,44], hot-die forging [34,35], extrusion [45] or rolling [35]. In order to destroy the rather coarse and inhomogeneous cast microstructure, and thus, for achieving a uniform microstructure, in general a two-step hot-working process is required [12,34]. Due to the high strain rate sensitivity of the flow stress (Sections 3.2 and 5.1), the hot-working parameters (temperature, strain rate, extrusion ratio, canning technology, etc.) have to be optimized carefully. Two-step isothermal forging of cast ingots in the ($\alpha + \gamma$) field leads to recrystallized uniform fine-grained microstructures. The resulting grain size decreases with flow stress according to a power law (Fig. 5) such as observed for conventional metals undergoing dynamic recrystallization [43,46]. Hot working and subsequent heat-treatment at a temperature slightly below or above the eutectoid one ($\sim 1125^\circ\text{C}$, Fig. 2) leads to ‘near- γ ’ microstructures—termed ‘NG’—consisting of equiaxed γ grains and some fine α_2 grains or precipitates (Fig. 4d). The uniformity of the equiaxed grain size depends on the chosen hot working conditions. It is considerably improved by multistep processing.

2.3. Lamellar colonies and interfacial boundaries

As they yield the best balance of mechanical properties, duplex and fine-grained nearly-lamellar microstructures are considered as being relevant for engineering materials [12,14]. Both microstructures comprise a high volume fraction of the *lamellar constituent*.

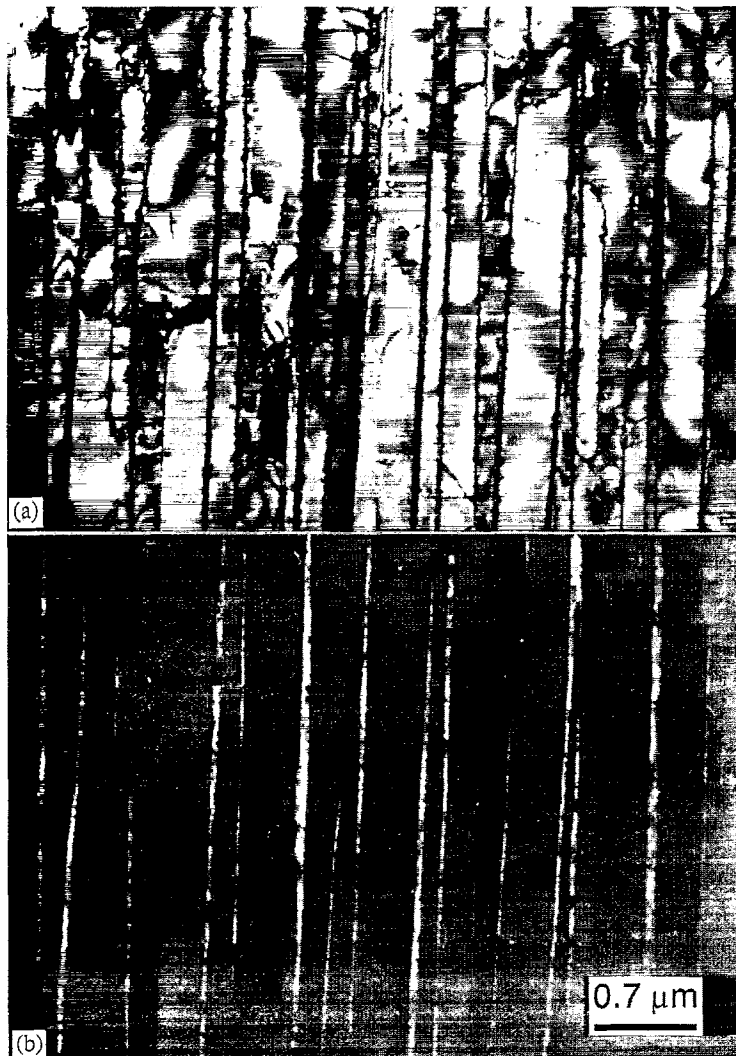


Fig. 6. TEM micrographs of lamellar ($\gamma + \alpha_2$) colonies in a cast Ti-48Al alloy. (a) Bright field. (b) Dark field displaying only the α_2 plates [49].

The lamellar structure is formed when Ti-rich two-phase alloys are heat-treated or hot-worked in the vicinity of the α transus line (Fig. 2) [47,48]. It displays a plate-like morphology which consists of parallel plates of the γ (TiAl) and the α_2 (Ti_3Al) phase (Fig. 6). The orientation relationship between the two phases is well documented [50–52] to be

$$(111)_{\gamma} \parallel (0001)_{\alpha_2} \text{ and } \langle 1\bar{1}0 \rangle_{\gamma} \parallel \langle 11\bar{2}0 \rangle_{\alpha_2}, \quad (2.1)$$

with the $(111)_{\gamma}$ plane being parallel to the lamellae boundaries. As will be outlined in Section 6.1, in the lamellar morphology, the γ phase is formed as domain structure composed of six differently oriented variants [52,53]. In addition to α_2/γ interfaces, this leads to different types of γ/γ interfaces with different interfacial structures. The latter which influence ductility, flow stresses, creep strength and crack propagation in NL and FL microstructures will be discussed in more detail in Section 6.1.

The lamellar spacing (λ_L) can be varied between some 10 nm and several micrometers depending on the cooling rate [12,23,52,53]. The lamellar grain size (colony size) can be varied in a controlled

manner in hot-worked material through dynamic recrystallization and subsequent heat-treatments [43,54,55]. γ (TiAl) alloys with a refined fully-lamellar microstructure—termed ‘RFL’—are seen to have appropriate combinations of controlled colony size and lamellar spacing leading to balanced properties [12,43]. However, the generation of a RFL microstructure requires a uniform cooling rate which might be difficult to achieve in thicker sections of a large component. In castings, the lamellar colony sizes are more difficult to control and often too coarse for achieving an appropriate balance of properties [14].

2.4. Unidirectionally solidified polysynthetically twinned (PST) crystals

As successfully demonstrated by Umakoshi et al. [56], Umakoshi and Nakano [57] and Fujiwara et al. [58], ingots of two-phase γ -alloys can be remelted and unidirectionally solidified in an optical floating zone furnace to result in a fully-lamellar material with all γ plates and interspersed α_2 plates being parallel. The specific orientation and lamellar spacing of these single-crystal-like ‘polysynthetically twinned (PST) crystals’ can be varied with respect to the solidification direction and with the solidification rate, respectively [51,58]. The structure of the lamellar boundaries is similar to that described in Section 2.2 for interfaces in the lamellar colonies of ‘polycrystalline’ material.

Tensile deformation of PST crystals with different angles ϕ between the tensile axis and the lamellar boundaries has significantly contributed to elucidate the plastic anisotropy and deformation structures [51,59,60] of the lamellar microstructure (cf. Sections 3 and 7.1).

In summary, it may be stated that hitherto a unique alloy composition has not emerged yet which, with respect to the achieved property profile, were to stand out against other alloy chemistries currently being studied worldwide. However, there is common agreement that γ (TiAl) alloys being developed for engineering applications must contain some Nb for improving the oxidation and corrosion resistance, and some Cr and/or Mn for better ductility. From a microscopic point of view, the influence of the latter two elements has not been elucidated yet. For increasing the strength level, there is a tendency to choose Al contents below 48 at.%. B and Si probably will be added to cast alloys for grain refinement and stabilization. Microstructural optimization shows a trend for fully-lamellar microstructures with colony sizes below 200 μm .

3. Tensile and fracture properties of two-phase γ -alloys

Like in other brittle materials, the deformation behavior of γ -alloys is largely controlled by its resistance to crack propagation and, thus, must be assessed in tensile testing.

3.1. Tensile properties at RT

The RT yield strength σ_y of two-phase γ -alloys typically varies between ~ 300 and ~ 650 MPa. It depends largely on the microstructure and the grain/colony size (d), and to a lesser extent on the alloy chemistry (Fig. 7). PST crystals (cf. Section 2.4) exhibit a strong dependence of σ_y on the orientation angle ϕ between the lamellar boundaries and the load axis (Fig. 8). As the deformation occurs on $\{111\}$ planes (cf. Section 4), $\phi=45^\circ$ represents the soft direction with $\sigma_y \sim 90$ MPa; this value most likely corresponds to the easiest mode of glide in the γ phase. For the hard orientations, $\phi=0^\circ$ and $\phi=90^\circ$, the related yield stresses are significantly higher, i.e., ~ 290 and 500 MPa, respectively [13,62].

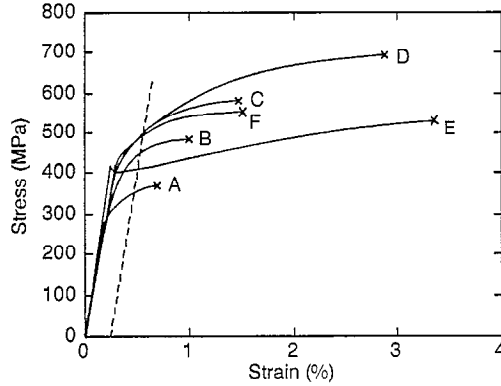


Fig. 7. Stress strain curves of different two-phase γ -alloys. Samples A, B, and C from forged Ti-47Al-1Cr-1V-2.5Nb had FL microstructures with colony sizes decreasing from 700–1300 μm (A) to 250–500 μm (C). D had a NL microstructure with a lamellar colony size of 70–140 μm and γ grains of 10–30 μm (data from Ref. [23]). Sample E from forged Ti-47Al-2Cr-0.2Si had a NG microstructure. Note the pronounced yield drop effect often observed in hot-worked material. Sample F from investment-cast and HIPed Ti-47–4% (Mn, Cr, Nb, B, Si) [Müllauer et al., unpublished work].

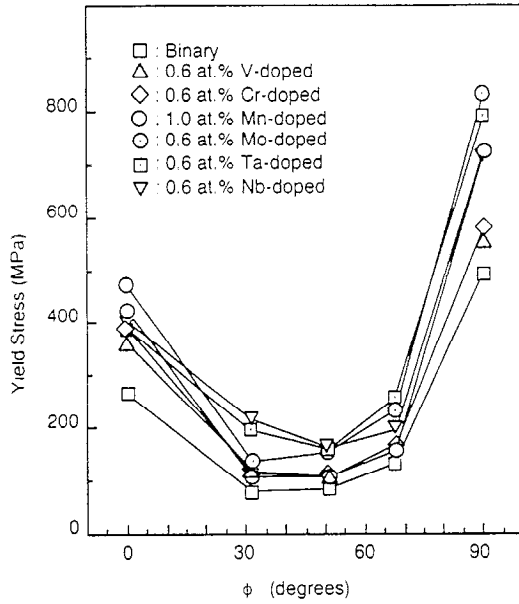


Fig. 8. Variation of the RT yield stress with orientation angle ϕ of two-phase PST γ -Ti49Al-alloys with various ternary alloying additions (after [13]).

As shown in Fig. 7, the yield strength of a polycrystalline fully-lamellar (FL) microstructure increases from ~ 300 MPa to 500 MPa when the size of the lamellar colonies is decreased from ~ 1200 to 300 μm [23,57].

This observation which has been assessed also for fine grained near gamma (NG) and duplex (D) microstructures [18,19,61] has been interpreted in terms of a Hall-Petch relationship (Fig. 9):

$$\sigma_y = \sigma_o + k_y d^{-1/2}. \quad (3.1)$$

For equiaxed (NG) microstructures, the Hall-Petch constant k_y was determined to range from ~ 0.9 to ~ 1.4 [18,19,61] (Fig. 9a). For polycrystalline FL microstructures and for PST crystals, there exist some controversies on whether the lamellar colony size (d_L), the lamellar spacing (λ_L) or the domain size (d_d) within one lamella acts as the microstructural length parameter to affect σ_y .

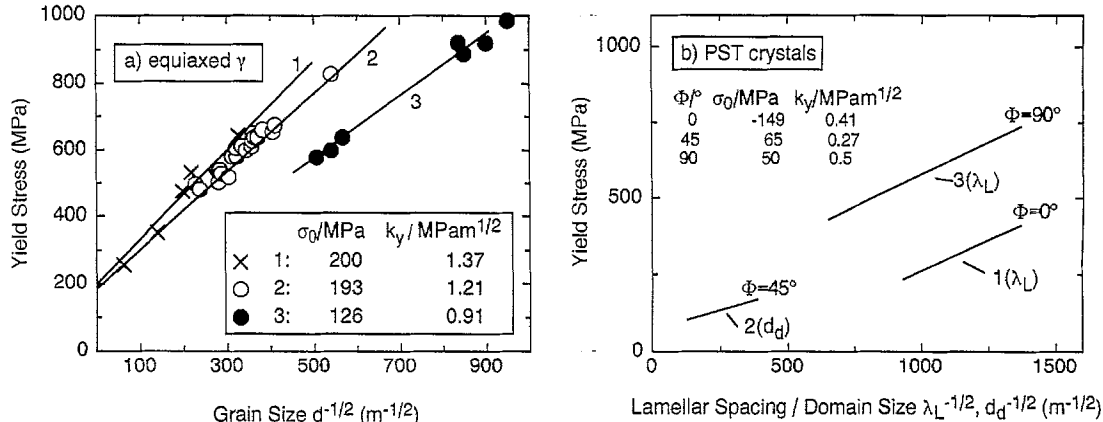


Fig. 9. Dependence of the yield stress on different microstructural length parameters as plotted in terms of the Hall–Petch relation. (a) For equiaxed γ -alloys; the grain size has been used as the relevant structural length parameter. Curve 1 from Ref. [19], 2 from Ref. [18], and 3 from present work. (b) For PST crystals with different orientations. For $\phi=0^\circ$ and 90° (curves 1, 3 [56,57]) the lamellar spacing, and for $\phi=45^\circ$ (curve 2 [56]) the domain size have been correlated with the yield stress.

Through correlation of σ_y with d_L , Kim and Dimiduk [11], Kim [12] and Wurzwallner et al. [34] obtained an unusually high value of $k_y^{\text{FL}} \sim 5 \text{ MPa} \sqrt{\text{m}}$. Recently, this value was corrected to $k_y^{\text{FL}} \sim 2.5 \text{ MPa} \sqrt{\text{m}}$ for $\lambda_L \sim 1 \mu\text{m}$, and assumed to increase with decreasing λ_L [63].

For PST crystals, k_y^{PST} was determined from a correlation of the ϕ -dependent flow stress (Fig. 8) with their lamellar spacings λ_L or domain sizes d_d (Fig. 9b) [56,57]. For the soft orientation ($\phi=30^\circ$), k_y^{PST} was evaluated to be somewhat lower (0.27 MPa $\sqrt{\text{m}}$) than for the hard orientations where $k_y^{\text{PST}}(\phi=0^\circ) \sim 0.41$ and $k_y^{\text{PST}}(\phi=90^\circ) \sim 0.5$. However, as inferred from Fig. 9b, for $\phi=0^\circ$ this Hall–Petch type analysis yields a negative value for σ_o in Eq. (2.1). Both this unphysical result and the unusually high value of k_y^{FL} for polycrystalline FL microstructures cast much doubt on employing just one microstructural length parameter when explaining the observed increase of σ_y on refining the lamellar microstructure. This open question will be addressed further in Section 7.1.

Koeppe et al. [18] also found a Hall–Petch type relationship when correlating the fracture stress (σ_f) with the size of coarse γ grains which were embedded into the fine-grained duplex microstructure of a single-step forged Ti–48Al–2Cr alloy. Substantiated by fractographic analyses, they concluded that fracture is initiated by cleavage of coarse γ grains according to a Hall–Petch type related mechanism followed by intergranular propagation of the crack within the fine-grained duplex constituent of the microstructure. Thus, the fracture stress is reached when the stress concentration ahead of a pile-up exceeds the theoretical strength.

Aiming for high tensile ductilities (ε_f) at RT in duplex material, the microstructure must be very homogeneous with a uniform grain size [18]. These structures can be generated in two-step hot worked materials (cf. Section 2.2) leading to ductilities as high as $\varepsilon_f \sim 3.5\%$ (Fig. 7). In contrast, the highest ductilities reported for investment cast duplex material are less than 2% (Fig. 7) due to the coarse and non-uniform cast microstructure which is difficult to be removed by subsequent heat treatments [14,21,42]. The ductility of FL microstructures is low. Like σ_y , it increases with decreasing colony size though barely exceeding 1% plastic tensile strain (Fig. 7) [23,32].

Like yield strength, the tensile elongation of PST crystals also depends strongly on the orientation angle ϕ (Fig. 10, insert). It is highest for the soft direction ($\phi=30^\circ$) where shear deformation is not impeded by the lamellar boundaries, and may easily exceed the maximum ductility of polycrystalline fully-lamellar material by a factor of more than twenty [60]. This result renders the γ phase in

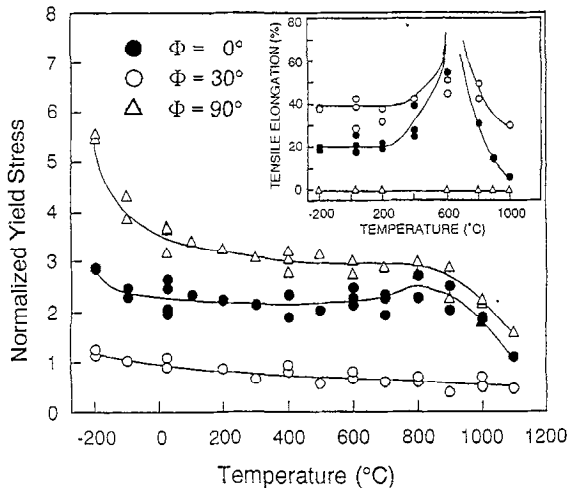


Fig. 10. Temperature dependence of the yield stress and tensile elongation (insert) of PST crystals with different orientation angles. The yield stress has been normalized with σ_y (20°C ; $\phi = 30^\circ$) in order to emphasize the much higher strength levels of the hard orientations $\phi = 0^\circ$ and $\phi = 90^\circ$ [64].

equilibrium with the α_2 phase to be rather deformable. As oxygen is considered to embrittle the γ phase, the high deformability in two-phase γ -alloys is seen to result from the partitioning of oxygen from the γ to the α_2 phase with its much higher oxygen solubility [25,65] (cf. Sections 7.2 and 7.3).

3.2. Tensile properties at elevated temperatures

The tensile ductility of two-phase γ -alloys is characterized by a rather sharp brittle-to-ductile transition at a temperature T_{bd} which for typical strain rates $\dot{\varepsilon} \sim 1 \times 10^{-4} \text{ s}^{-1}$ ranges from ~ 620 to $\sim 800^\circ\text{C}$ depending on the microstructure (Fig. 11). T_{bd} is lowest for NG and D microstructures and highest for FL ones. Its pronounced shift towards higher temperatures with increasing $\dot{\varepsilon}$ indicates the brittle-to-ductile transition to be controlled by thermally activated processes (cf. Section 5.1).

Below T_{bd} , the ductility remains about constant and increases steeply with increasing temperature above T_{bd} (Fig. 11). The ductilities of fine-grained D, NG and of FL microstructures commonly exceed 30% at 800 and 900°C , respectively, when tested at low strain rates ($\dot{\varepsilon} \leq 10^{-4}/\text{s}$) (Fig. 12b)

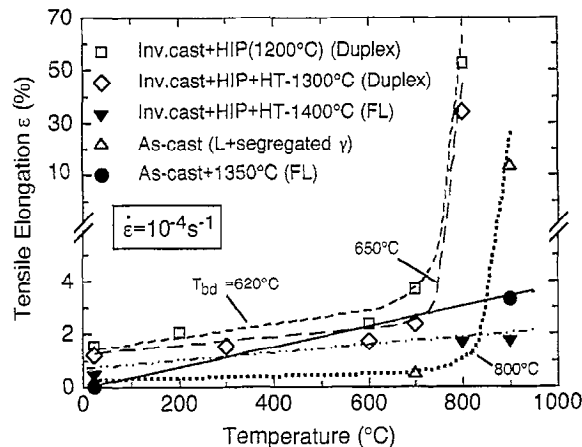


Fig. 11. Variation of tensile ductility with temperature for different microstructures.

[11,13,14,66,67]. This result already points towards the creep strength being a problem, in particular for materials with D or NG microstructures (cf. Section 8).

For $\phi=0^\circ$ and $\phi=30^\circ$, PST crystals also exhibit a brittle-to-ductile transition (Fig. 10). It is considerably less pronounced for $\phi=30^\circ$ as for this orientation the RT ductility is already 40%. For $\phi=90^\circ$, where the RT tensile elongation is small, no transition becomes discernible up to 1100°C [64]. This behavior is quite similar to that of polycrystalline γ -alloys with FL microstructures (cf. Fig. 11).

Below T_{bd} , the yield strength σ_y is only weakly dependent on temperature regardless of microstructure and alloy composition (Fig. 12). Above $T_{bd} \sim 700$ to 750°C, σ_y decreases rapidly although strength retention is superior for lamellar than for globular microstructures. For the hard orientations ($\phi=0^\circ$ and $\phi=90^\circ$), PST crystals show a similar behavior as polycrystalline alloys with FL microstructures (Figs. 10 and 12). For the soft orientation ($\phi=30^\circ$), the yield stress decreases rather continuously and does not exhibit a sudden softening beyond $\sim 800^\circ\text{C}$ [64].

As exemplified in Fig. 13a for a testing temperature of 700°C, the yield strength is also strongly dependent on the strain rate [67], which points towards the stress being controlled by the dislocation mobility [68–70] (cf. Section 5.1). This, in fact, holds true for the entire temperature regime of 20 to $\sim 800^\circ\text{C}$ which is relevant for future applications of γ -alloys.

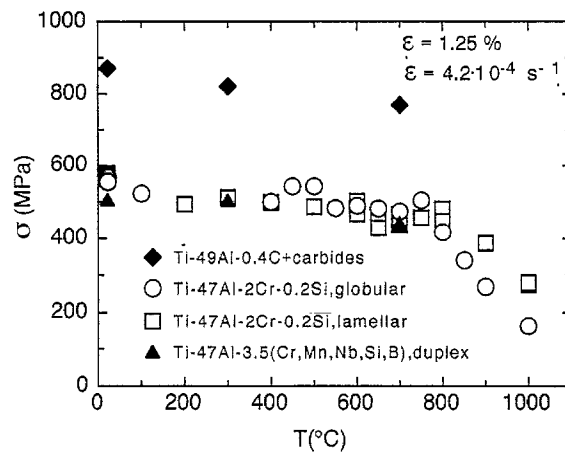


Fig. 12. Variation of the flow stress with testing temperature for different two-phase γ -alloys.

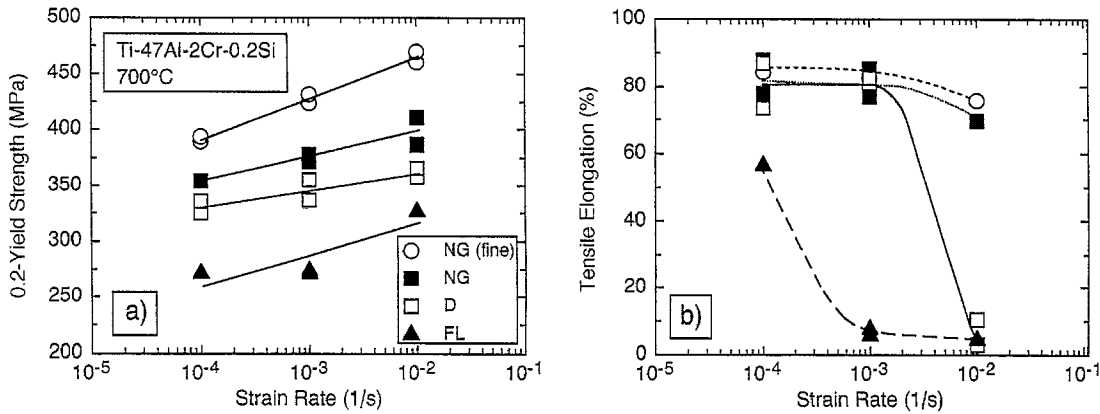


Fig. 13. Dependence of 0.2% off-set yield stress (a) and tensile elongation (b) on strain rate at 700°C for hot rolled Ti-47Al-2Cr-0.2Si with fine-grained near-gamma (NG), duplex (D) and coarse-grained fully-lamellar (FL) microstructures (data from Ref. [67]).

Unlike single phase γ -alloys [19,71,72], two phase γ -alloys and PST crystals usually do not exhibit the anomalous dependence of σ_y on testing temperature (Figs. 10 and 12); i.e., the yield stress anomaly which is often associated as being typical for intermetallic alloys [73,74] has not become evident in most experimental studies of two-phase γ -alloys even though it has been observed occasionally [75]. The two-phase alloys usually exhibit a broad plateau of the flow stress [68] in the temperature range from 20 to $\sim 700^\circ\text{C}$ (e.g., Fig. 12).

3.3. Fracture resistance

The fracture behavior of $\gamma(\text{TiAl})$ has frequently been analyzed in terms of fracture resistance (K_R) curves [76–81]. When tested at RT, the K_R curves of D and NG material run almost flat (Fig. 14) indicating brittle behavior with little resistance to crack growth or tearing. The initiation value which under plane strain conditions corresponds to the fracture toughness K_{lc} , ranges from $\sim 11 \text{ MPa}/\text{m}$ for D alloys with about equal fractions of the two microstructural constituents (L, γ) [12,14,44,82–86] (Fig. 14), and increases to $\sim 18 \text{ MPa}/\text{m}$ for γ -alloys with lamellar grains prevailing [13,78]. With increasing temperature, the fracture toughness is found to increase continuously to values exceeding $30 \text{ MPa}/\text{m}$ for NG and $20 \text{ MPa}/\text{m}$ for D alloys at 700°C [87] (Fig. 15). At this temperature, crack propagation is more stable as manifested by the increasing crack extension (Fig. 15).

At 20°C , the fracture toughness of polycrystalline FL alloys ranges from 20 to $30 \text{ MPa}/\text{m}$ (Figs. 14 and 15) and, thus, is considerably larger than for D and NG material. The observed pronounced K_R curve behavior (Fig. 14) [44,76,80] suggests crack initiation to be followed by stable crack growth. This behavior is even more pronounced at temperatures above T_{bd} with the toughness after extensive crack growth being considerably higher than for D and NG alloys. However, unlike the latter, FL alloys do exhibit a less pronounced dependence of the fracture toughness on temperature (Fig. 15).

Compared to duplex microstructures, the fully-lamellar alloys exhibit a higher fracture toughness and a more stable crack growth behaviour. These features suggest that tough $\gamma(\text{TiAl})$ alloys for engineering applications should be designed on the basis of a lamellar microstructure [5,12,44]. However, the lamellar colonies should have a random orientation and the colony size has to be kept rather small and uniform. Coarse grained lamellar materials suffer from a large variability of toughness [83,87]. The large variability is seen to be caused by the anisotropy of the crack resistance within the

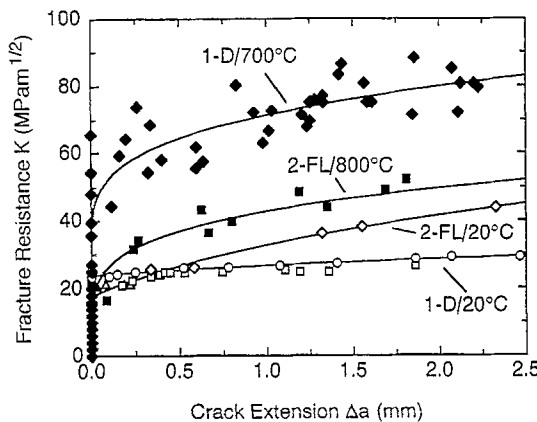


Fig. 14. Curves 1: Crack growth resistance curves of investment-cast Ti–48Al–2Cr (duplex) at 20 and 700°C □, ○ compact tension (CT)-50 specimens with fatigue precracks and displacement rates of $10 \mu\text{m}/\text{h}$ and $600 \mu\text{m}/\text{h}$, respectively. △: CT-50 specimens with ECM-slit notch (radius $\sim 50 \mu\text{m}$) and $600 \mu\text{m}/\text{h}$. ♦: CT-2.6 specimen, $10 \mu\text{m}/\text{h}$ [14]. Curves 2: K_R curves of FL Ti–47Al–2.6Nb–2(Cr + V) at 20 and 800°C ; displacement rate $4.2 \times 10^{-2} \text{ s}^{-1}$. Data from Ref. [79].

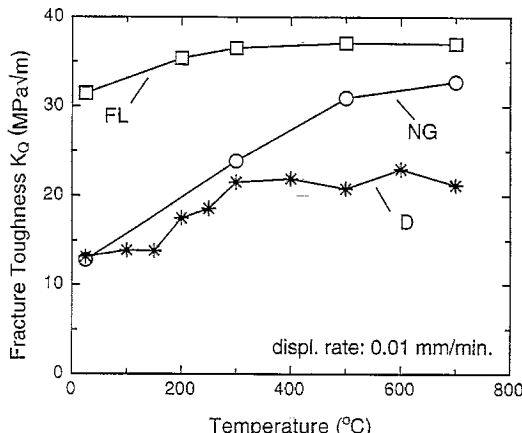


Fig. 15. Dependence of the fracture toughness on temperature for two-phase γ -alloys with different microstructures. ■, Ti-47Al-2Cr-0.2Si, lamellar ($d_L \sim 330$ nm, $\lambda_L \sim 0.05-1$ μ m); ○, Ti-47Al-2Cr-0.2Si, near gamma ($d_\gamma \sim 11$ μ m); * Ti-47Al-1Cr + Nb, Mn, Si, B, duplex ($d_\gamma \sim 30$ mm, $d_L \sim 200$ nm).

lamellar morphology [88]. This has been evidenced from studies on crack propagation parallel and perpendicular to the lamellar boundaries in PST crystals [89,90] and in as-cast materials with a preferred orientation of the lamellar colonies [83,87,91]. For cracks propagating parallel, the fracture toughness is relatively low (~ 12.5 MPa \sqrt{m}) and shows a large scatter when compared to cracks propagating perpendicular to the lamellar interfaces, the toughness of which is rather high ($\sim 20-25$ MPa \sqrt{m}) and the variability small [87]. The anisotropic nature of crack propagation in lamellar microstructures has also been recognized by electron microscopic studies of crack tip plasticity [92] as will be outlined in Section 9.

To conclude this section, it may be stated that in both cast and wrought alloys having homogeneous duplex or equiaxed microstructures, the ductilities achieved must no longer be seen as a hindrance to engineering applications. In contrast, the colony sizes in fully-lamellar microstructures which reveal superior toughnesses, must yet be optimized for providing ductilities which reassure the designer. The strength becomes strongly rate dependent at elevated temperatures. For strain rates higher than 10^{-4} s $^{-1}$ flow stresses of more than 500 MPa are retained up to service temperatures of $\sim 700^{\circ}\text{C}$.

4. Deformation structures

The plastic deformation of titanium aluminide alloys exhibits characteristics typical of deformation behaviour of other intermetallic compounds. These characteristics involve lack of ductility, strong temperature and orientation dependencies of the yield stress [16,20,50,93–96], anomalous increase of the yield stress with temperature, complex slip geometry and break-down of Schmid's law [95]. Since such phenomena are considered to be typical of deformation processes controlled by the core structure of dislocations [97,98], the present knowledge of the operative slip systems and of the fine structure of dislocations will be considered in more detail.

4.1. Burgers vectors and slip systems

The deformation behavior of γ (TiAl) is closely related to its $L1_0$ structure. The possible Burgers vectors are illustrated in Fig. 3c. Owing to the ordered structure ordinary dislocations of type $\langle 100 \rangle$ and $1/2\langle 110 \rangle$, respectively, and superdislocations of type $\langle 011 \rangle$ and $1/2\langle 112 \rangle$ occur [20]. Since the

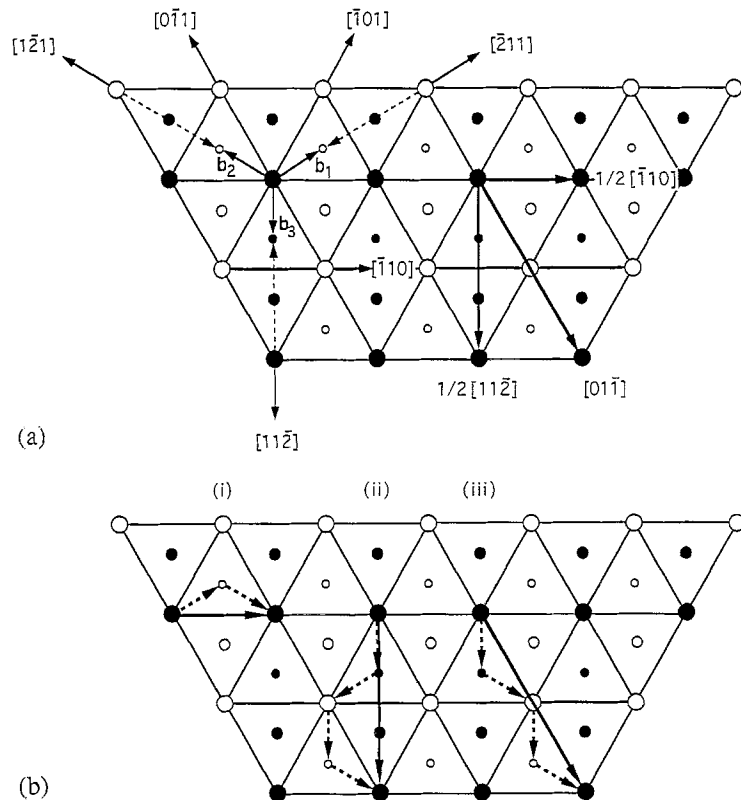


Fig. 16. Potential slip and twinning systems of the $L1_0$ structure. (a) Schematic drawing of three-layer sequence of atom stacking on the (111) plane shown by small, medium and large circles. The open and shaded circles denote Ti and Al atoms, respectively. $b_1 = 1/6[\bar{2}11]$, $b_2 = 1/6[1\bar{2}1]$ and $b_3 = 1/6[11\bar{2}]$ are the Burgers vectors of partial dislocations. b_3 is perpendicular to the Burgers vector $b = 1/2[\bar{1}10]$ for ordinary slip and represents the Shockley partial dislocations for true twinning, whereas b_1 and b_2 represent pseudo-twinning. (b) Core configurations of dislocations completely dissociated according to Eqs. (4.2)–(4.4) with Burgers vectors: (i) $b = 1/2[\bar{1}10]$, (ii) $b = 1/2[11\bar{2}]$, (iii) $b = [01\bar{1}]$.

$c:a$ axial ratio is close to unity, it is customary to describe dislocations in terms of the cubic notation. The parentheses used with the Miller indices follow the convention introduced by Hug et al. [99], which denotes all distinct permutations of $\pm h \pm k$. As shown in Fig. 3c and Fig. 16, Burgers vectors $1/2\langle 110 \rangle$, $1/2\langle 112 \rangle$ and $\langle 011 \rangle$ realize glide one the close packed {111} planes. Dislocations of these types have been observed mainly to contribute to deformation of $\gamma(\text{TiAl})$. $\langle 100 \rangle$ dislocations seem to be involved only at very high deformation temperatures [100], which is not the scope of the present study.

Plastic deformation of $\gamma(\text{TiAl})$ can also be realized by mechanical twinning associated with $1/6\langle 11\bar{2} \rangle \{111\}$ shear [94,101,102]. There is only one distinct true twinning along $b_3 = 1/6[11\bar{2}]$ on (111) that does not alter the ordered $L1_0$ structure (Fig. 16). Shear in the reversed direction along $-2b_3$ is the so called complementary or anti-twinning mode. The other partials designated as b_1 and b_2 in Fig. 16 lead to pseudo-twinning [102]. As far as twin boundary energies and the mobilities of the related twinning partial dislocations are considered, true twinning is prevalent in $\gamma(\text{TiAl})$ [104,105].

The perfect and superdislocations mentioned above are liable to adopt different core configurations, thus, reducing their energy. In a first step, superdislocations can decompose into perfect and superdislocations with smaller Burgers vectors [99]. The newly formed dislocations are not bounded

by a planar fault and can move independently. Decomposition of $\langle 011 \rangle$ superdislocations according to

$$[01\bar{1}] \rightarrow 1/2[11\bar{2}] + 1/2[\bar{1}10] \quad (4.1)$$

has been proposed by Greenberg [106]. Since the Burgers vectors of the reaction products are perpendicular to each other, no energy is gained according to Frank's rule. Nevertheless, the mechanism has been justified by first-principles total energy calculations and anisotropic elastic modelling [107,108] and has been observed for particular orientations of $\langle 011 \rangle$ dislocations in different binary and ternary alloys [99,109–111]. In a next step of energy reduction, ordinary and superdislocations may dissociate in their $\{111\}$ slip planes, which give rise to the formation of stacking fault ribbons limited by partial dislocations. Due to the tetragonal symmetry of the $L1_0$ structure, three types of planar faults can be defined in the $\{111\}$ planes: (i) superlattice intrinsic or extrinsic stacking faults (SISF or SESF); (ii) antiphase boundaries (APB); and (iii) complex stacking faults (CSF), which combine APB and SISF or SESF.

On the (111) plane shown in Fig. 16, the planar faults SISF, APB and CSF are related to the displacement vectors $1/6\langle 11\bar{2} \rangle$, $1/2\langle 10\bar{1} \rangle$ and $1/6\langle \bar{1}\bar{2}1 \rangle$, respectively. Because of the large variety of potential Burgers vectors and planar faults, various planar and non-planar core configurations can be formed. Fig. 16b shows complete dissociation of $1/2[\bar{1}10]$, $1/2[11\bar{2}]$ and $[01\bar{1}]$ dislocations confined to a single (111) plane according to the following schemes [20,99]

$$1/2[\bar{1}10] \rightarrow 1/6[\bar{2}11] + CSF + 1/6[\bar{1}\bar{2}\bar{1}], \quad (4.2)$$

$$1/2[11\bar{2}] \rightarrow 1/6[11\bar{2}] + SISF + 1/6[\bar{2}\bar{1}\bar{1}] + APB + 1/6[11\bar{2}] + CSF + 1/6[\bar{1}\bar{2}\bar{1}], \quad (4.3)$$

$$[01\bar{1}] \rightarrow 1/6[11\bar{2}] + SISF + 1/6[\bar{1}\bar{2}\bar{1}] + APB + 1/6[11\bar{2}] + CSF + 1/6[\bar{1}\bar{2}\bar{1}]. \quad (4.4)$$

The extent and mode of dissociation is expected to have significant effects on the dislocation mobility, which is particularly important for brittle materials like TiAl. Experimental observations and theoretical investigations of core structures in γ (TiAl) reported in the literature will therefore be summarized in the following. The dissociation of $\langle 011 \rangle$ dislocations in a Ti–54Al alloy has first been studied by Hug et al. [99] using TEM-weak beam observations. Accordingly, the dislocation splits into a triplet involving an APB and SISF as

$$[01\bar{1}] \rightarrow 1/6[11\bar{2}] + SISF + 1/6[\bar{1}\bar{2}\bar{1}] + APB + 1/2[01\bar{1}]. \quad (4.5)$$

The dissociation corresponds to the situation sketched in Fig. 16b with the CSF bounded partials being not dissociated. After room temperature deformation, the two planar defects have been found to be situated on the same (111) plane so that the split configuration is planar and assumed to be glissile. At elevated temperatures, the screw segments of the $\langle 011 \rangle$ dislocations were found to adopt a non-planar configuration with the APB lying on a cube plane [99]. The Kear and Wilsdorf [112] configuration of dissociated dislocations is considered to be highly sessile. The earlier investigations of Hug et al. have been essentially confirmed by recent TEM observations on binary and ternary alloys [113–115]. The observed change in dissociation configuration with temperature is analogous to the Kear and Wilsdorf locking mechanism currently thought to explain the flow stress anomaly in some $L1_2$ alloys [116,117]. An alternative mode of non-planar dissociation of $\langle 011 \rangle$ dislocations has been observed in a Ti–54Al alloy after deformation at 600°C by high resolution electron microscope (HREM) observations [103]. The dislocations have been found to split into (111) and $(\bar{1}\bar{1}\bar{1})$ planes bound by an APB on (010) . This configuration is considered to be sessile.

Planar and non-planar dissociation have also been reported for $1/2\langle 11\bar{2} \rangle$ superdislocations. In a two-phase Ti–46Al alloy deformed at room temperature, these dislocations have been found to dissociate into a triplet of $1/6[11\bar{2}]$, $1/6[2\bar{1}\bar{1}]$ and $1/2[01\bar{1}]$ dislocations bound by a SISF and an APB and confined to a single (111) plane [118]. The dissociation mode corresponds to the route sketched in Fig. 16b, however, the two partials with the CSF in between are not dissociated. Alternatively, the $1/2\langle 11\bar{2} \rangle$ dislocations can dissociate into an extrinsic and intrinsic stacking fault bounded by three identical $1/6\langle 11\bar{2} \rangle$ partial dislocations [115,119,120]. The partials have been found to be situated on adjacent (111) planes so that a non-planar configuration occurs, which is assumed to be sessile. The mechanism has been observed in binary [115] and ternary [119] alloys deformed at room temperature and in an undeformed ternary alloy [120]. At room temperature, the dissociated configuration is considered to be sessile. At elevated temperatures, the dislocations become glissile and disappear as they nucleate microtwins [119].

According to Eq. (4.2), ordinary $1/2\langle 110 \rangle$ dislocations may dissociate into Shockley partials bounding a CSF. Observations by weak beam TEM revealed that the separation of the partials is below the resolution limit of this method [121]. The compact core has also been confirmed by recent HREM observations of $1/2\langle 110 \rangle$ dislocations in alloys of Ti–48.5Al–5Ga [103] and Ti–52Al [121]. Fig. 17 demonstrates the HREM image of an $1/2\langle 110 \rangle$ dislocation in Ti–48.5Al–5Ga. The observations suggest that the mobility of ordinary dislocations is impeded by inherent lattice friction effects and not by a non-planar core dissociation [103].

Theoretical investigations of core structures in γ (TiAl) are based on atomistic simulations [113,122–127], first-principles quantum mechanical calculations and continuum mechanical modelling [107,108,128]. Atomic simulations using embedded atom method (EAM), the potentials of which had been fitted to structural and elastic parameters of γ (TiAl) have revealed stable (111) APB, (100) APB, (111) CSF, and (111) SISF faults [113,122–126]. The fault energies are summarized

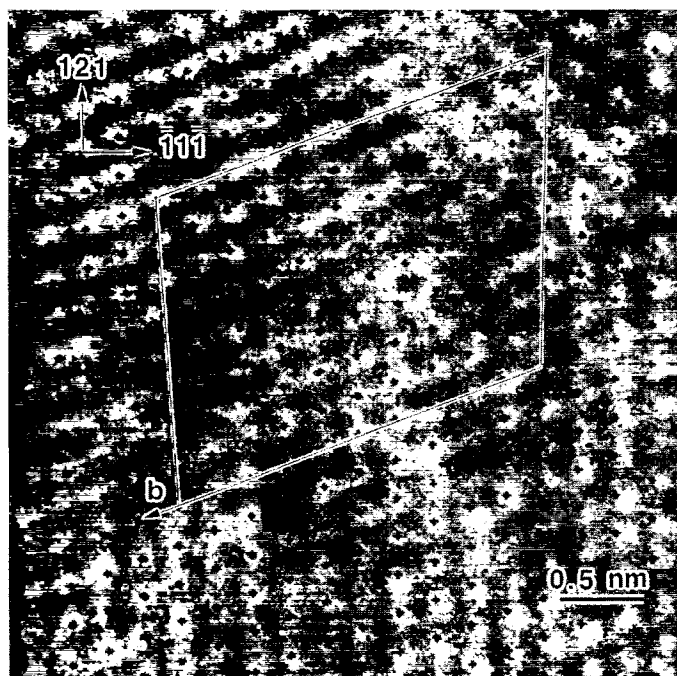


Fig. 17. An ordinary $1/2\langle 110 \rangle$ dislocation in a Ti–46.5Al–5Ga alloy. The projected Burgers vector of the dislocation is $1/4[1\bar{2}1]$, as is evidenced from the presence of one extra $\{\bar{1}\bar{1}\}_{\gamma}$ plane, (Micrograph: Hemker et al. [103]).

Table 1
Shear fault energies of γ (TiAl) in units of mJ/m^2 together with the method of observation

Alloy	$\text{APB}_{(100)}$	$\text{APB}_{(111)}$	$\text{CSF}_{(111)}$	$\text{SISF}_{(111)}$	$\text{SESF}_{(111)}$	Method	Reference
Ti-50Al	430	510	600	90	80	LDF	[107,108]
Ti-50Al	350	670	280	110	110	LDF	[128,129]
Ti-50Al	91	550	320	220		EAM	[124]
Ti-50Al	268	322	308	60		EAM	[123]
Ti-50Al	51	275	275	3		FS	[125]
Ti-54Al		130–160		70–85		WB	[99]
Ti-54Al	210	253		140		WB	[128]
Ti-52Al			470–620			HREM, EAM	[122]
Ti-52Al					142	WB	[130]

LDF (local density functional theory); EAM (embedded atom method); FS (Finnis–Sinclair Simulation); WB (weak beam TEM); HREM (high resolution TEM).

in Table 1 together with results obtained with the local density functional (LFD) theory [107,108,128,129] and experimental data [99,130,131]. It is interesting to note that the APB energies predicted are lower in {111} planes than in {010} planes. Thus, the observed core transformation of the ⟨011⟩ dislocations by cross slip of the APB's from (111) to (010) appears to be thermodynamically justified.

The theoretical studies essentially confirm the experimental observations described above, though differences in the details do exist. The predicted core dissociations follow the plausible trend that the highest planar fault energies produce the smallest spreadings. The high values of the APB and CSF energies imply that the dissociation involving these faults are often below the resolution limit of weak beam TEM [108,124,129,130]. The calculations particularly confirm the compact core structure of the $1/2\langle 110 \rangle$ dislocations as observed in HREM–TEM [115,122]. For superdislocations planar and non-planar core configurations are predicted. The adopted configuration depends on the dislocation character, with edge dislocations tending to form planar cores [123]. ⟨011⟩ superdislocations are expected to dissociate according to Eq. (4.4) with the APB located on either the (111) or (100) plane. Alternatively, the dislocations may dissociate into non-parallel {111} planes forming stacking fault ribbons on these planes [123,125,130]. The $1/2\langle 112 \rangle$ superdislocations are expected to spread into two adjacent {111} planes so that a superlattice extrinsic fault is formed within the core. The fault can be considered as microtwin, which may operate as nucleation center for twinning [120,125]. The energy of planar faults as a function of composition in binary and ternary TiAl alloys have been investigated by first principles electronic structure calculations [129]. Accordingly, in two-phase alloys, the APB, CSF and SISF energies are significantly lower when compared with fault energies calculated for stoichiometric alloys. Of the ternary additions Cr, Nb and Mn considered, Mn has the strongest effect in reducing (111) APB, CSF and SISF energies. Deformation induced defect structures are therefore expected to depend on alloy composition.

From the atomistic simulations, significant effects of the core structure on the dislocation mobility are expected. Dislocations with planar cores seem to move relatively easily, whereas those with non-planar cores appear to be effectively locked. For non-planar cores of $1/2\langle 110 \rangle$ screw dislocations a friction stress of 250 MPa has been estimated, which is almost one order of magnitude greater than those of 30° mixed and edge orientations [123,126]. Significantly higher friction stresses have been predicted for the corresponding characters of ⟨011⟩ superdislocations [123]. The results support the predictions of Greenberg et al. [132] that the dislocation mobility in TiAl is impeded by strong anisotropic Peierls stresses due to the directional bonding of the material, a view which has been addressed in subsequent experimental investigations [133].

4.2. Microscopic observations

Plastic deformation of crystalline materials leads to the formation of three dimensional dislocation arrays, which are characteristic of the mechanisms governing the mobility, multiplication and annihilation of perfect and twinning dislocations. Deformation induced structures have therefore been widely studied in order to gain a better understanding of the ductility and fracture problems associated with these micromechanisms. The investigations cover a wide range of parameters such as alloy composition, microstructure and deformation temperature. In view of the extensive body of literature, the frame of reference established here will involve deformation structures in two-phase alloys. However, the γ phase present in these alloys can have different Al contents [134] which may have significant implications on the mechanical properties and the deformation substructure developed. Thus, particular emphasis will be placed on alloying effects on PST crystals (cf. Fig. 8) which always have a fully-lamellar microstructure.

TEM observations of deformed two-phase alloys have revealed the presence of all types of perfect and twinning dislocations described in Section 4.1. For the evaluation of the microstructures reported, however, the following limitations should be considered. Processing of two-phase alloys often comprises a significant hot working of the material due to the application of metallurgical techniques such as forging, rolling or extrusion (cf. Section 2.2). The thermomechanical treatments mostly lead to formation of dense defect structures so that the starting materials prior to deformation exhibit dislocation densities higher than 10^7 cm^{-2} . Deformation induced defect structures seem therefore to be manifested only after a significant straining of at least 2%. In most TEM observations, no special measures were taken to prevent loss or rearrangement of dislocations on unloading or during foil preparation. Because of the high structural stability of the material and the relatively low defect mobilities, however, the changes taking place after deformation at ambient temperatures do not appear seriously to alter the dislocation structure. A drawback possibly more serious than those mentioned above, is that the presentations of TEM observations mainly rely on descriptive or relative terms so that no rigorous quantitative analysis of deformation induced defect structure is available. Regarding these problems, results obtained on two-phase PST crystals seem to be beneficial since their microstructure is much better defined when compared with polycrystalline materials. Thus, observations of deformation structures in PST crystals will be first reported.

The dislocation substructure developed in PST crystals was investigated after tensile and compression to strains mostly ranging between $\varepsilon = 1\text{--}3\%$ [59,64,135]. The experiments were performed on differently oriented samples so that shear processes parallel and across the lamellar interfaces were initiated (cf. Section 3.1). The Schmid factors for the operative slip systems were assessed from a knowledge of the foil normal in given domains so that information on the relative ease and activity of the different deformation modes could be obtained. At room temperature, twinning has been found to be the principal deformation mode, which can easiest be activated, followed by glide of ordinary $1/2\langle 110 \rangle$ dislocations and at last by glide of $\langle 011 \rangle$ superdislocations [135]. The differences of the related yield stresses is expected to be relatively small, however, so that the deformation mode in a certain lamella can be selected according to the respective Schmid factor. In addition, the activation of the more difficult glide along $\langle 011 \rangle$ is believed to be assisted by constraint stresses which may develop when adjacent domains or lamellae are sheared by twinning along $1/6\langle 11\bar{2} \rangle \{111\}$ or $1/2\langle 110 \rangle \{111\}$ glide. Thus, at sufficiently large strains, all three deformations are thought to operate. The results have essentially been confirmed by TEM observations after room temperature deformation of ternary Ti–48Al based PST crystals doped with 0.6 V or Zr, respectively (cf. Fig. 8) [136]. Dislocation structures of PST crystals generated by elevated temperature deformation contain mainly $1/2\langle 110 \rangle$ dislocations and to a lesser extent $\langle 011 \rangle$ and $1/2\langle 112 \rangle$ dislocations [135]. An important



Fig. 18. Deformation structure observed after room temperature compression to strain $\varepsilon=3\%$ showing glide of ordinary $1/2\langle 110 \rangle$ dislocations and $1/6\langle 11\bar{2} \rangle \{111\}$ order twinning. Ti-48Al-2Cr, foil orientation and deformation axis close to $\langle 101 \rangle$.

feature is that the propensity of twinning strongly decreases at temperatures above 1073 K. Specimens deformed under these conditions in tension exhibited dynamic recrystallization in their necked parts.

Observations of deformation structures of polycrystalline two-phase alloys documented in the literature suggest a more complex picture. As far as room temperature deformation is concerned, most results have revealed that glide of ordinary dislocations is the primary deformation mode followed by true twinning [20,76,118,137–142]. Fig. 18 demonstrates the deformation substructure typically observed in a Ti-48Al-2Cr alloy after room temperature deformation to strain $\varepsilon=3\%$. The material investigated has a nearly-lamellar microstructure with a high degree of preferred orientation of the lamellae so that the orientation of the deformation axis could be assessed with respect to the micrograph. In the present case, the deformation axis was parallel to the lamellar boundaries. Trace analysis and stereographic examinations of the dislocation substructure revealed that in this orientation of the lamellae often two oblique $1/2\langle 110 \rangle \{111\}$ slip systems were activated with the Burgers vectors being inclined to the interfaces (see Section 7.4). Estimations of dislocation densities with the help of the intersection method [143] typically yield values of 10^8 – 10^9 cm^{-2} . The contribution of superdislocations to room temperature deformation has been differently estimated. Relatively low densities of $1/2\langle 112 \rangle$ and $[011]$ superdislocations have been reported in [76,117,137–142], whereas an abundant occurrence of these dislocations and faulted dipoles has been observed in recent studies on binary and

ternary two-phase alloys [75]. In some cases (e.g., Fig. 18), the twins are found to be bounded by more than one set of twinning partials. This gives rise to the speculation that anti-twinning operations may occur. Hitherto, there has been little information about this process, clearly further investigations are required. Although the effects of the α_2 phase on the mechanical properties of the titanium aluminides is well established, very little information is available on the deformation behavior of the α_2 constituents of two-phase alloys. In part, this is certainly due to the small scale of α_2 grains or lamellae and the dense mismatch structures usually associated with them. Nevertheless, work in this area is progressing. During room temperature deformation local plasticity by dislocations with $b = 1/3\langle 11\bar{2}0 \rangle$ on prismatic planes has been recognized [144]. At 800°C, a more homogeneous activation of this type of slip system was observed. In addition, glide and climb of dislocations with $b = 1/3\langle 2c + a \rangle$ and $b = [c]$ occurs. This activation of c -component dislocations was thought to reduce the strong plastic anisotropy of $\alpha_2(\text{Ti}_3\text{Al})$.

Twining has been often observed to occur on multiple $1/6\langle 11\bar{2} \rangle \{111\}$ systems with non-parallel shear vectors leading to extensive intersections among twin bands [141,145–148]. Twin intersections are particularly important since they represent a potential locking mechanism that reduces the propagation of twinning dislocations. Fig. 19 shows the intersection of twin bands in a high resolution TEM micrograph of a Ti–48.5Al–1.5Mn alloy deformed in tension at room temperature. The horizontal twin (1) which probably pre-existed, was sheared by the incident twin (2). Deflection of twin (1) can be described as following the trace of the (001) basal plane such that the intersection region is essentially congruent with the lattice of the most deflected twin (1). What is believed to be



Fig. 19. Intersection of deformation twins propagating in a γ lamella of a two-phase Ti–48.5Al–1.5Mn alloy deformed at $T=300$ K in tension to failure. The horizontal twin (1) probably pre-existing is sheared by the vertical twin (2). Note that the lattice in the intersection region coincide with the lattice of the deflected twin (1), for comparison the traces of the (001) basal planes were indicated. The high density of one plane steps at the interface between twin (1) and the matrix (arrowed) indicates the immobilization of twinning partial dislocations. Another vertical twin (3) is immobilized at twin (1). Foil orientation close to $\langle 110 \rangle$.

interesting and important is that a significant internal stress and high density of defects seem to remain in the intersected region as indicated by the strong contrast variation observed, and it is speculated that these structural features can give rise to nucleation of recrystallization at elevated temperatures. The intersection process seems also to provide some resistance against twin propagation. This is indicated by the high density of one-plane steps (arrowed) in the interface between twin (2) with the matrix. This suggests that $1/6\langle 11\bar{2} \rangle$ twinning dislocations are immobilized in front of twin (1). Another vertical twin (3) is stopped at twin (1). Crystallographic configurations of intersecting twin bands have been analyzed in [145,146]. Though differences exist in some details, the structural features described here appear to be essentially consistent with the mechanism designated as type I in [145,146]. Possible mechanisms of twin intersections in the $L1_0$ structure have been discussed in a recent review [149].

Regarding high temperature deformation, the most striking feature of polycrystalline two-phase alloys is the strong increase of the propensity of twinning, when compared with PST crystals [75,76,141]. Fig. 20a demonstrates the deformation structure observed in a Ti–48Al–2Cr alloy deformed in tension at 1073 K. The twins are generally very narrow, as demonstrated in Fig. 20b by the frequency distribution of their widths [150]. Owing to the high density of twins, however, a significant deformation can locally be realized as estimated from the twinning shear given in [101,102].

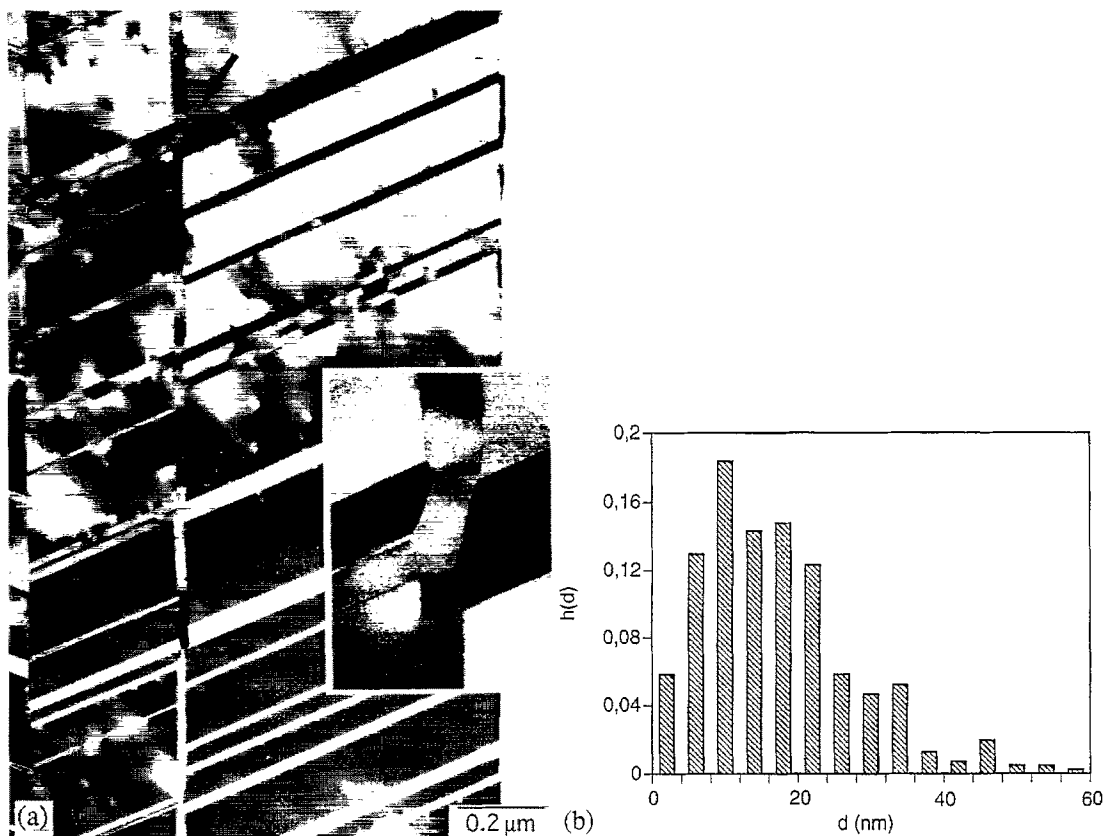


Fig. 20. Deformation twinning at elevated temperatures. (a) Deformation twins in a Ti–48Al–2Cr alloy generated during tensile deformation at $T=1073$ K to strain $\varepsilon=8.9\%$. Note the immobilization of the twins at the lamellar interfaces. The inset shows the region designated by the arrow in a higher magnification to demonstrate earlier stages of recrystallization. The process usually starts in front of the twins immobilized at the interfaces. (b) Frequency distribution $h(d)=\Delta N/N_0$ of the widths h of deformation twins generated during tensile deformation at $T=1073$ K to strain $\varepsilon=8.9\%$. ΔN is the number of twins found in the width intervals, and $N_0=884$ is the total number of the investigated twins.

In γ grains or γ lamellae which are suitably oriented for true twinning, the mechanism may therefore be considered as the principal deformation mode at elevated temperatures. As shown in Fig. 20a, the slip paths of the twins are essentially limited by the width of the lamellae, an observation which suggests that the lamellar interfaces are very effective barriers for the translation of shear deformation. In front of the immobilized twins recrystallization was frequently observed, an earlier stage of which is shown in the insert of Fig. 20a. It is speculated that the nucleation of new grains is supported by the high shear stresses expected in front of the blocked twins. Dislocation structures generated in two-phase alloys by elevated temperature deformation contain preferentially $1/2\langle 110 \rangle$ dislocations in configurations which suggest that climb occurs under these deformation conditions [75]. Climb of ordinary dislocations at 700°C was directly evidenced by *in situ* heating studies on a Ti–48Al–2Cr alloy performed inside the TEM [151,152].

4.3. Slip/twin interactions due to constraint stresses

The preceding discussion has shown that if a wide range of deformation conditions is considered, all of the deformation modes discussed in Section 4.1 can contribute to deformation. In particular, strain is accomplished in part by true twinning along $1/6\langle 11\bar{2} \rangle \{111\}$, an observation which is consistent with the low stacking fault and twin boundary energies when compared with the APB and CSF energies (Table 1). Thus, in terms of the van Mises criterion for the plastic deformation of polycrystalline material, on principle a sufficient number of independent slip systems is available. However, a general feature of the deformation of γ (TiAl) and $(\alpha_2 + \gamma)$ TiAl alloys is that only one or two slip systems are being activated under most conditions. It is tempting to speculate that the selection of these deformation modes is determined by the differences of the individual critical flow stresses, as has been proposed in [135,136,153,154]. Due to the small number of slip systems being activated significant constraint stresses may develop during straining. This can have serious implications for the activation of more difficult shear processes. Thus, the evolution of deformation substructure will be considered under these two aspects.

In the microstructure of two-phase alloys generated at room temperature, ordinary $1/2\langle 110 \rangle$ dislocations are predominant, which is consistent with their relatively low Peierls stress when compared with superdislocations (Section 4.1). Glide along $1/2\langle 110 \rangle$ often occurs simultaneously with true twinning. A quantitative evaluation of twin densities and widths in moderately deformed materials ($\varepsilon = 3\%$) indicates that appreciable shear deformations up to 5% can be achieved locally. As the critical shear stress law is not a well defined concept for twinning [149], it is difficult to decide which of the two mechanisms will be activated in a certain grain or lamella. However, the shear stress across the twinning plane K_1 and resolved in the twinning direction η_1 must be positive. Thus, owing to the small number of twinning systems available in the $L1_0$ structure (Section 4.1), many grains are certainly unfavorably oriented for twinning. Changes of the deformation mode between true twinning and $\langle 110 \rangle$ glide are therefore a characteristic feature, commonly observed at adjacent grains or lamellae [141,150]. Fig. 21a demonstrates this behaviour in a Ti–48Al–2Cr alloy with a lamellar microstructure. The slip path of the twin propagating in lamella γ_1 is limited by the lamellar boundaries. Apart from a narrow secondary twin, in lamella γ_2 the shear deformation is accomplished by glide of ordinary dislocations situated on $(1\bar{1}\bar{1})$ planes (see also Fig. 20a and Fig. 46c). The dislocations have the Burgers vector $b = 1/2\langle 110 \rangle$, which is not contained in the interface. The glide processes start from dislocation loops, which are probably emitted from the interface due to the coherency stresses [155]. This mechanism will be described in more detail in Section 6.1.

In grains or lamellae which are unfavorably oriented for $1/2\langle 110 \rangle$ glide or true twinning, significant constraint stresses can be developed due to the shape change of deformed adjacent grains.

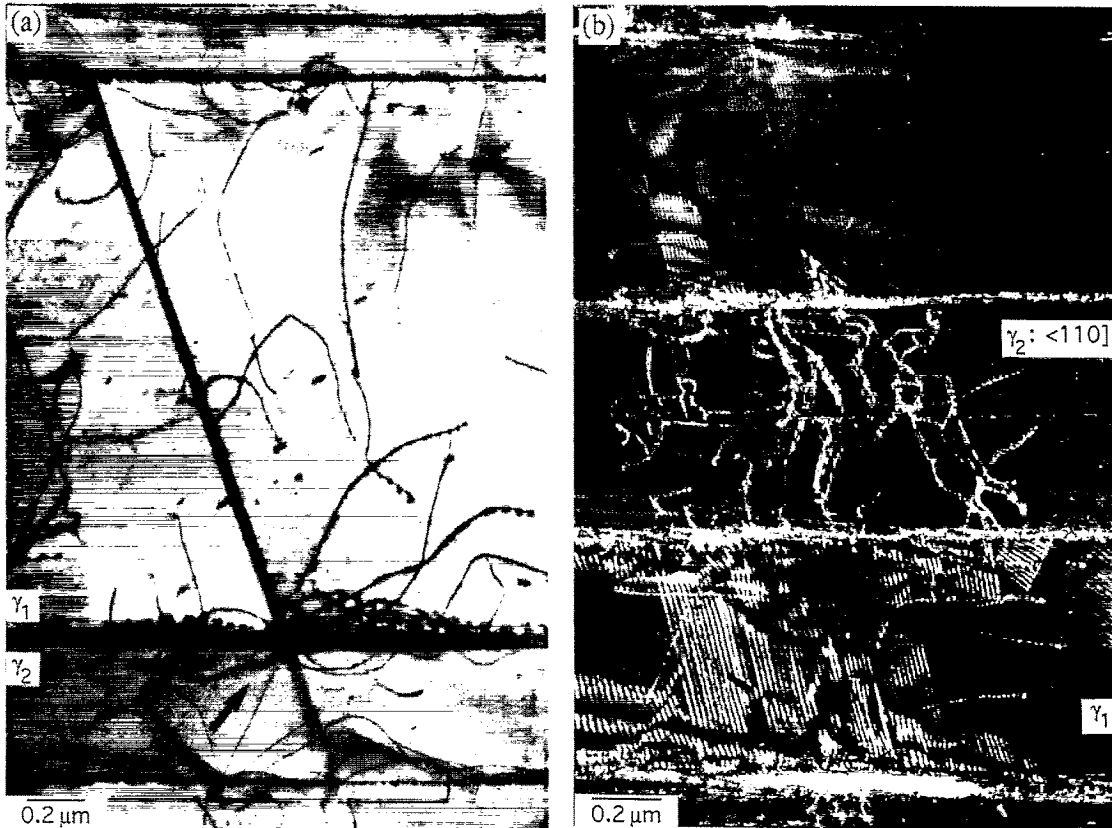


Fig. 21. Transmission of shear deformation across lamellar boundaries of a Ti-48Al-2Cr alloy. (a) Change of the deformation mode between true twinning and glide of ordinary dislocations in adjacent lamellae. Tensile deformation at $T = 300$ K to strain $\varepsilon = 0.25\%$. Foil orientation close to $\langle 101 \rangle$. (b) Generation of superdislocations in a lamellar Ti-48Al-2Cr alloy. Foil orientation and deformation axis close to $\langle 101 \rangle$. Due to its $\langle 110 \rangle$ orientation, lamella γ_2 is unfavorably oriented for the glide of $1/2\langle 110 \rangle$ dislocations. The generation of the superdislocations (mostly of type $1/2\langle 112 \rangle$) in lamella γ_2 is probably supported by the high constraint stresses exerted by the deformation twins immobilized at the interface γ_1/γ_2 . Compression at $T = 300$ K to strain $\varepsilon = 3\%$.

The constraint stresses are believed to assist overcoming of the high Peierls stresses expected for the superdislocations (Section 4.1) so that glide processes of these dislocations are locally initiated. An inability to meet this condition leads to small strain to failure. Thus, after sufficient straining, all of the potential deformation modes should be observed if a sufficient volume of deformed material is examined [154]. As an example, Fig. 21b demonstrates the generation of superdislocations in a γ lamella which was unfavorably oriented for the glide of ordinary dislocations.

It is interesting to note that the contribution of superdislocations to deformation is not significantly enhanced at elevated temperatures. A possible explanation is that the superdislocations become locked under these deformation conditions due to the dissociation reactions discussed in Section 4.1. This view is supported by observations on single phase alloys, which have also revealed glide of ordinary dislocations at elevated temperatures, although the materials at ambient temperatures preferentially deform by superdislocations [133,156]. Thus, deformation of the two-phase alloys at elevated temperatures probably is also realized by only a small number of independent slip systems. Unlike the situation at room temperature, however, the constraint stresses seem to be more easily accommodated, which probably contributes to the higher ductility observed under these deformation conditions. It is speculated that the accommodation processes are supported by the observed thermally activated non-

conservative dislocation mechanisms [75,151,152,156,157] (cf. Section 5.1). Furthermore, at elevated temperatures, the accommodation of constraint stresses can be accomplished by the formation of a three-plane deformation structure [141,158,159]. The mechanism was first recognized by Singh and Howe [158] in Ti–48.7Al heavily deformed at room temperature. The formation of the structure seems to involve an anti-twinning operation on every third {111} plane leading to a repeat distance of 0.7 nm and the ABC/BCA/CAB stacking being typical of the 9R structure. As mentioned in Section 4.1, anti-twinning is considered to be difficult when compared with true twinning so that it should preferentially operate at high stresses or with the assistance of thermal activation. Hence, the formation of the 9R structure is considered to be a potential mechanism for the accommodation of constraint stresses at elevated temperatures. It is believed that such conditions frequently occur during the deformation of two-phase alloys with a lamellar microstructure. The lamellar boundaries present in these materials have been found to be strong barriers for the propagation of shear processes [57–60,135,141,142,150] so that significant constraint stresses can be developed, even during straining at elevated temperatures. In correspondence to this picture, the 9R structure was frequently observed adjacent to lamellar boundaries. Fig. 22 demonstrates the 9R structure in a HREM image of a Ti–48.5Al–1.5Mn alloy with a lamellar microstructure deformed at 1173 K. Since the twinning processes occur on (111) planes parallel to the interfaces, shear deformation along the lamellae is realized. It is speculated that the mechanism is preferentially activated in the so called soft orientation of lamellar microstructures where shear stresses parallel to the lamellae are applied. In this way, the formation of the 9R structure may contribute to the plastic anisotropy observed in these microstructures. The mechanism was also observed after creep deformation of two-phase alloys, as will be described in Section 8. It should be noted, however, that similar three-plane structures have also been observed in

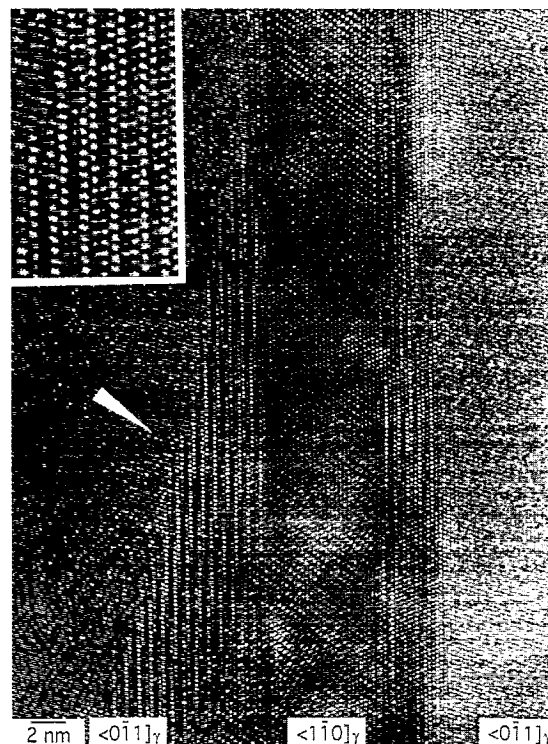


Fig. 22. Translation of shear deformation along lamellar interfaces. The three plane deformation structure adjacent to the interface (insert) exhibit the stacking sequence being typical of the 9R structure. Ti–48.5Al–1.5Mn alloy deformed in tension at 1173 K to failure at $\varepsilon_f = 8.9\%$.

a massively transformed, but undeformed Ti–48.7Al alloy [160]. Based on a close examination of the contrast phenomenon, the structure has alternatively been interpreted as arising from overlapping twin related γ variants. The problem clearly needs further investigation.

To conclude this section, it should be appreciated that various potential deformation mechanisms may contribute to the plastic deformation of two-phase titanium aluminides. These involve glide of perfect dislocations with Burgers vectors $b = 1/2\langle 110 \rangle$, $b = 1/2\langle 112 \rangle$ and $b = \langle 011 \rangle$, respectively, and $1/6\langle 11\bar{2} \rangle\{111\}$ order twinning. The fine structure of ordinary and superdislocations is determined by the planar defects involved in the dissociation. The high values of the APB and CSF energies imply narrow and often non-planar spreading of the dislocation cores.

The core structure of $\langle 011 \rangle$ superdislocations can undergo glissile to sessile transformation as the APB plane changes from (111) to (010) . This mechanism certainly contributes to the anomalous high flow stress observed at elevated temperatures. The core structure of ordinary $1/2\langle 110 \rangle$ dislocations is very compact, which suggests that cross slip is relatively easy. The dislocation mobility is expected to be relatively low and strongly anisotropic regarding screw and edge components. In particular, high friction stresses are expected for non-planar core configurations of screw dislocations. This dislocation character can therefore dominate in deformation induced defect structures.

The relative contribution of the individual deformation mechanisms seems to be determined by the differences in the related critical flow stresses. Under most experimental conditions, deformation of two-phase alloys seems to be facilitated by ordinary $1/2\langle 110 \rangle$ dislocations and $1/6\langle 11\bar{2} \rangle\{111\}$ order twinning. The experiments also provide phenomenological evidence for the importance of constraint stresses to activate more difficult mechanisms such as glide of superdislocations or the formation of the 9R structure. The critical flow stresses of the individual deformation mechanisms are probably closely related to the factors governing the mobility of perfect and twinning dislocations. In this way, the qualitative differences among the results reported in the literature can be explained by differences in composition or impurity contents, which are expected to have significant effects on the dislocation mobilities. Serious implications can particularly arise from high oxygen or nitrogen contents. No systematic data on this problem are available due to the difficulties in controlling these elements. The mechanisms governing the dislocation mobilities in $(\alpha_2 + \gamma)$ titanium aluminides will be investigated in more detail in Section 5.1.

5. Microprocesses of plasticity

Titanium aluminides are relatively brittle materials, exhibiting little plasticity at ambient temperatures. Typical of such deformation behavior is that the gliding dislocations are either too low in density or too immobile to allow the specimen to match the strain rate superimposed by the testing machine. Regarding high temperature applications, strength retention is most important. This, on the other hand, will degrade if the dislocation mobilities and multiplication rates increase. The factors governing these aspects of dislocation dynamics are expected to depend on alloy composition, phase distribution, grain size, and impurity concentration. Understanding of the related micromechanics can contribute to optimize the balance between damage tolerance at ambient temperatures and high temperature strength via modification of the alloy parameters mentioned above. To this end, in this chapter, the glide resistance and multiplication mechanisms of dislocations will be investigated.

5.1. Dislocation mobilities

In technical materials like TiAl, the movement of dislocations can be impeded by different types of glide resistance. Overcoming of glide obstacles with short-range stress fields can be assisted by

thermal activation so that the related (thermal) stress part τ^* is dependent on temperature T and shear strain rate $\dot{\alpha}$. Another type of glide resistance arises from glide obstacles with long-range stress fields, which produces barriers too large for thermal activation to be significant. The related (athermal) stress part τ_μ is almost independent of $\dot{\alpha}$ and T , apart from the small variation of the shear modulus μ with T . In most cases, short-range and long-range obstacles contribute simultaneously to the flow stress τ so that it is often written as

$$\tau = \tau^* + \tau_\mu \quad (5.1)$$

τ describes the total glide resistance to crystallographic shear, which can be converted into a stress σ applied on the polycrystalline material by use of a Taylor factor of $f = 3.06$ as

$$\sigma = f\tau = f(\tau^* + \tau_\mu). \quad (5.2)$$

Similarly, the macroscopic strain rate may be expressed as $\dot{\varepsilon} = \dot{a}/f$.

Interaction mechanisms of dislocations with glide obstacles can be characterized in terms of activation energies and activation volumes. Several approaches have been proposed in the literature to estimate these interaction parameters from deformation tests. The analysis applied here originates from Schöck [161] and starts from the assumption that \dot{a} is controlled by a single thermally activated process with the Gibbs free energy of activation ΔG . In this case, the rate equation for plastic flow may be written as

$$\dot{a} = \dot{a}_0 \exp -\Delta G/kT. \quad (5.3)$$

with

$$\Delta G = \Delta F^* - V\tau^* \quad (5.4)$$

and

$$\tau^* = (1/V) \left(\Delta F^* + kT \ln \frac{\dot{a}}{\dot{a}_0} \right). \quad (5.5)$$

k is the Boltzmann constant. The other parameters involved in Eqs. (5.3)–(5.5) are explained for overcoming localized obstacles by reference to Fig. 23. The dislocation encounters obstacles, separated

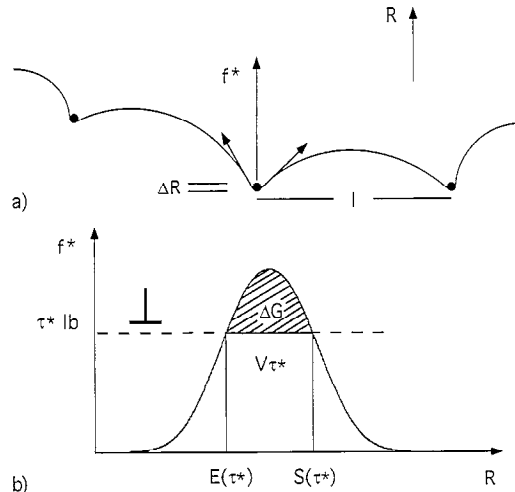


Fig. 23. Thermally assisted overcoming of localized glide obstacles separated by distance l . (a) Interaction force f exerted on the obstacles by the line tension of the dislocation areas being in balance with the applied effective shear stress τ^* . (b) Force/distance potential $f(R)$ showing the energy contributions ΔG and $V\tau^*$ for overcoming the obstacles.

by distance l , each of which provides a resisting force γ balanced in equilibrium by line tension forces (Fig. 23a). To overcome the glide obstacles, the dislocation must move in the direction of R . The associated energy change can be visualized by the force distance potential $f(R)$; (Fig. 23b). ΔG describes the change of the Gibbs free energy between the equilibrium position $R(E)$ and the saddle point position $R(S)$ of the dislocation at the obstacle, respectively, and is supplied by the thermal energy of the crystal. ΔF^* is the free energy of activation and corresponds to the total energy for overcoming the obstacle at given $\dot{\alpha}$ and T . The energy contribution $V\tau^*$ is the work done mechanically during the activation event. $V=lb\Delta R$ is the activation volume which contains the obstacle distance l , the Burgers vector and the activation distance $\Delta R=R(S)-R(E)$. The pre-exponential $\dot{\alpha}_0$ is proportional to the density of mobile dislocations ρ_m , to their vibrational frequency and to their glide distance after a successful activation event. $\dot{\alpha}_0$ is considered to be constant so that the dependence of $\dot{\alpha}$ on τ arises from the stress dependence of ΔG . In this formulation, a thermally activated process is characterized by the parameter ΔG , τ^* , ΔF^* and V .

Under the condition that $\dot{\alpha}_0$ and l are independent of τ and T , the parameters V and ΔG are related to the stress increments $(\Delta\sigma/\Delta T)_\dot{\epsilon}$ and $(\Delta\sigma/\Delta \ln \dot{\epsilon})_T$ which can be determined by temperature or strain rate cycling tests as

$$V=fkT/(\Delta\sigma/\Delta \ln \dot{\epsilon})_T, \quad (5.6)$$

$$\Delta G=\frac{Q_e+V\sigma(T/\mu f)(\partial\mu/\partial T)}{1-(T/\mu)(\partial\mu/\partial T)}, \quad (5.7)$$

$$Q_e\equiv\Delta H=-TV(\Delta\sigma/\Delta T)_\dot{\epsilon}/f. \quad (5.8)$$

Q_e is the experimental activation energy, which for a stress independent obstacle distance is identical to the activation enthalpy ΔH .

On the basis of this analysis, activation volumes and activation energies were determined on different two-phase alloys in a wide temperature range [68,151,152,162–164]. Alloy compositions and microstructures investigated are listed in Table 2. The oxygen and nitrogen contents of the alloys are typically 600 and 100 ppm, respectively. Sample preparation and details of the deformation tests are described elsewhere [162,163]. The results reported here are typical of this class of materials and

Table 2
Alloy compositions and microstructures

Alloy	Composition (at.%)	Processing and microstructure
1a	Ti-47Al-2Cr-0.2Si	two-stage forging at 1500 K: near gamma structure, grain size 11 μm
1b	Ti-47Al-2Cr-0.2Si	two-stage forging at 1500 K followed by annealing at 1650 K, nearly-lamellar structure, colony size 330 μm, lamellar spacings 0.05–1 μm
2	Ti-48Al-2Cr $\phi = 0^\circ, 45^\circ, 90^\circ$	as-cast: nearly-lamellar structure, colony size 1000 μm, lamellar spacings 0.05–1 μm, small volume fraction of lamellar grains
3	Ti-47Al-1Cr with additions of Nb, Mn, Si and B	HIP: nearly-lamellar structure, colony size 200 μm, small amount of gamma grains of about 30 μm
4	Ti-49Al-1V-0.3C	near gamma, grain size 16 μm
5	Ti-45Al	fully-lamellar
6	Ti-45Al-5Nb	fully-lamellar, colony size 138 μm, lamellar spacing 0.1 μm
7	Ti-45Al-10Nb	duplex, colony size 94 μm, interlamellar spacing 0.11 μm, intercolony α_2 and γ of about 8.4 μm grain size
8	Ti-48Al-10Nb	near gamma

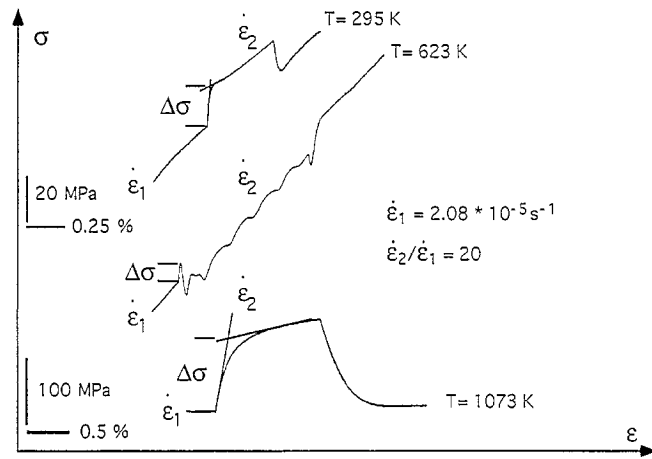


Fig. 24. Stress transients observed in strain rate cycling tests performed at different temperatures, Ti-47Al-2Cr-0.2Si.

were obtained on an alloy with the composition Ti-47Al-2Cr-0.2Si. In order to investigate the influence of structural parameters on thermally activated glide processes, two different microstructures were generated by thermomechanical treatments. Two-stage forging at 1500 K with a height reduction of 70% in each stage resulted in a near gamma structure with an average grain size of about 11 μm . By subsequent annealing at 1650 K for 1 h, a nearly-lamellar structure with a colony size of about 330 μm was generated.

The shape of the stress responses to changes of temperature or strain rate depends on the test temperature, as demonstrated in Fig. 24 for strain rate cycling tests. The stress transients are well expressed between 230 and 400 K, whereas yield drop effects and serrations are superimposed between 400 and 800 K. Above 800 K, smooth stress transients were observed. Yield drop phenomena and smooth stress responses have been commonly associated with changes of the mobile dislocation density. In this case, the pre-exponential in Eq. (5.3) is not any longer constant and the change of $\dot{\varepsilon}$ in a strain rate cycling test, e.g., is partially realized by a change of the mobile dislocation density so that the dislocation velocity does not correspond to the ratio of the strain rates. The implications of these effects were investigated in a separate study of strain rate cycling test in which the strain rate ratio $n = \dot{\varepsilon}_2/\dot{\varepsilon}_1$ was systematically varied and which will be published elsewhere [163]. Accordingly, structural changes occur at test temperatures of 973 K, which significantly reduce the stress response to changes of $\dot{\varepsilon}$. The effects can be minimized if small strain rate ratios are being applied. In the present study for test temperatures higher than 973 K, a strain rate ratio of $n = 3$ was used. For this value, $\Delta\sigma$ could still be determined with ease and accuracy.

The activation parameters were found to depend on temperature, strain rate, and strain. In this section, the processes controlling the dislocation mobility at the critical yield stress will be investigated. Thus, the values estimated at the beginning of deformation will be discussed first. According to Eq. (5.5), τ^* is inversely proportional to the related activation volume. Thus, in Fig. 25, the values of σ and $1/V$ were compared for the temperature range investigated. Reduced values σ/μ are shown in Fig. 25a so that stress changes due to the temperature dependence of the shear modulus could be separated. $\mu(T)$ was calculated from the data measured by Schafrik [165]. σ/μ exhibits qualitatively the same dependence on temperature as σ , which suggests that this variation cannot be explained on the basis of athermal processes only. There is a clear difference in the temperature dependencies of σ/μ and $1/V$, however, which leads to the assumption that the mechanisms controlling the dislocation mobility change strongly over temperature regime studied. Thermally activated processes contribute to the flow stress at temperatures between 230 and 400 K but are almost negligible around 600 K.

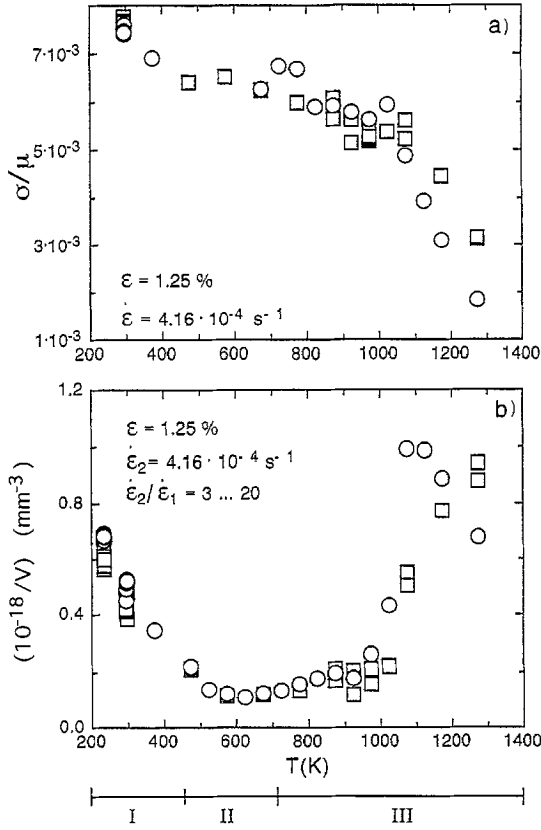


Fig. 25. Flow stresses σ and reciprocal activation volumes $1/V$ measured at the beginning of deformation; dependencies on deformation temperature T . ○ near gamma and □ nearly-lamellar microstructure; (a) flow stress $\sigma_{1.25}$ measured at strain $\varepsilon = 1.25\%$ and reduced by the shear modulus μ ; (b) reciprocal activation volume $1/V$.

$1/V$ increases again above 900 K, where the material becomes ductile and σ starts to decrease. Accordingly, the mechanism determining the deformation behavior in the regimes I, II and III indicated in Fig. 25 will be discussed separately. Activation volumes have also been determined on a Ti–47.5Al–2.5Cr alloy [166], which exhibited an anomalous flow stress peak at 723 K and significant quantitative differences in V with respect to the results presented here.

In all temperature regimes, different mechanisms may provide athermal stress components, which must be separated from the total stress in order to characterize the thermal stress contribution τ^* . To this end, as a first approximation dislocation densities and grain sizes may be considered. A stress part

$$\sigma_{\text{dis}} = f \alpha \mu b \sqrt{\rho_{\text{dis}}} \quad (5.9)$$

certainly arises due to the long-range elastic interactions between the dislocations [167]. ρ_{dis} is the total density of dislocations; $\alpha = 0.5$ was assumed for dislocations gliding on parallel planes. Although the alloys investigated at strain $\varepsilon = 1.25\%$ have a high dislocation density $\rho_{\text{dis}} = 10^8 \text{ cm}^{-2}$, the calculated stress contribution $\sigma_{\text{dis}} = 30 \text{ MPa}$ is relatively small. As will be described in Section 7.1, long-range dislocation interactions with grain boundaries are usually related to stress part $\sigma_{\text{HP}} = k_y d^{-1/2}$ of the Hall–Petch Eq. (3.1). For the alloy with the near gamma microstructure, the stress contribution $\sigma_{\text{HP}} = 400 \text{ MPa}$ was estimated using $k_y = 1.35 \text{ MPa} \sqrt{\text{m}}$ [168] (cf. Section 3.1) and the observed grain size $d = 11 \mu\text{m}$. However, as will be described in Section 6.2, lamellar interfaces provide strong barriers to dislocations and deformation twins, which suggests that overcoming of these barriers results in a significant athermal stress contribution. Since the values of σ and $1/V$ of the two microstructures are

Table 3

Activation parameters of two-phase TiAl alloys, $\varepsilon = 1.25\%$, $\dot{\varepsilon} = 4.16 \cdot 10^{-4} \text{ s}^{-1}$ [68,163,164] (for alloy compositions and microstructures, see)

Alloy	T (K)	σ (MPa)	V/b^3	ΔH (eV)	ΔG (eV)
1a	295	538	91	0.98	0.81
1b	295	517	103	0.96	0.77
2, $\phi=0$	295	404	133	0.84	0.65
3	295	626	93	1.06	0.86
4	295	570	116	1.09	0.86
5	295	890	92		
6	295	803	79		
7	295	953	69		
8	295	676	85		
1a	1100	368	47	3.16	2.40
1b	1100	435	73	3.13	2.25
2, $\phi=0$	1100	360	61	2.04	1.37
3	1100	458	51	2.90	2.35
4	1100	476	70	3.07	2.46
5	1100	634	99	3.71	2.56
6	1100	656	91	4.46	3.15
7	1100	672	53	4.19	3.05
8	1100	459	82	4.04	2.87

almost identical in the temperature interval investigated, the same athermal stress contribution $\sigma_\mu = \sigma_{\text{HP}} + \sigma_{\text{dis}} = 430 \text{ MPa}$ was assumed. Using this value, the activation parameters

$$\tau^* = 30 \text{ MPa}, V = 91b^3, \Delta G = 0.81 \text{ eV}, V\tau^* = 0.5 \text{ eV}, \Delta F^* = 1.3 \text{ eV}$$

were calculated. V was related to the Burgers vector of ordinary dislocations, which seem to contribute significantly to the deformation at room temperature. For comparison, in Table 3 activation parameters determined on two-phase titanium aluminide alloys with different compositions and microstructures were summarized. The small values of V and the relatively high activation energies suggest that the glide resistance in the regime I of the $\sigma(T)$ -curve (Fig. 25a) arises from a high density of relatively strong obstacles. These features of dislocation dynamics become evident in the observed dislocation structures. Fig. 26 shows the typical morphology of dislocations generated by room temperature deformation. In the dislocation structure $1/2\langle 110 \rangle$ screw dislocations are predominant, which suggests that the mobility of ordinary dislocations is anisotropic with the higher glide resistance being present at the screw components. This observation is in accordance with the results of the atomistic simulations of dislocation cores, which have been discussed in Section 4.1. The dislocations are strongly bowed out between closely separated pinning centers indicating their high glide resistance. The alloys investigated had an oxygen content of about 600 wt. ppm, which is well beyond the solubility limit in $\gamma(\text{TiAl})$ [25] (cf. Section 7.3). Thus, it is likely that precipitation of the excess oxygen leads to the formation of discrete glide obstacles. However, a detailed examination of the dislocation morphology revealed that a significant number of the pinning centers were formed at jogs in the screw dislocations. Due to the compact core structure of the ordinary dislocations (cf. Section 4.1), cross slip is probably very easy. The driving forces for cross slip may originate from sources of internal stresses such as dislocation intersections or coherency stresses at lamellar interfaces (cf. Section 6.2). Thus, the high density of the jogs appears to be plausible. The jog dragging certainly provides an additional glide resistance to the screw components of $1/2\langle 110 \rangle$ dislocations. This is seen as another reason for the predominance of this dislocation character in the deformation microstructure.



Fig. 26. Structure of $1/2\langle 110 \rangle$ dislocations generated during room temperature deformation. The screw dislocations are strongly bowed out between localized obstacles and jogs (arrow 1), which indicates that the dislocation motion is impeded by a high glide resistance. Note the dislocation dipoles and debris defects which are trailed and terminated at jogs (arrow 2). Ti-48Al-2Cr alloy. Foil orientation close to $\langle 101 \rangle$.

The distances between the glide obstacles are considerably larger, however, than the values expected from the activation volume. It is therefore speculated that additional glide resistance arises from a lattice friction mechanism. This is also suggested by the observation that the dislocations in the unloaded samples are still bowed out in a smooth arc. It is therefore assumed that high lattice friction forces occur on all dislocation characters. Furthermore, in the observed configuration the dislocations are situated on $\{111\}$ planes which are inclined at large angles to the foil surface. High image forces are therefore expected so that the stressed dislocations should easily escape from the foil, if no friction forces were present.

The glide resistance provided by the two processes seems to disappear at about 600 K as indicated by the small value of $1/V$. Nevertheless, the total flow stress σ is practically unchanged. It is therefore speculated that the dislocation mobility in regime II of the $\sigma(T)$ curve (Fig. 25a) is impeded by another type of dragging mechanism so that the stress level of regime I is maintained. As demonstrated in Fig. 24, negative strain rate sensitivities were observed in this temperature regime ($T=623$ K) when steady state flow stresses before and after the strain rate changes are compared, and serrations in the load-elongation traces occur. Such behavior has been associated with the Portevin-Le Chatelier effect due to the diffusion of solute atoms to the dislocations [169–172]. In order to get further confirmation whether such type of mechanism occurs, static strain ageing experiments were performed

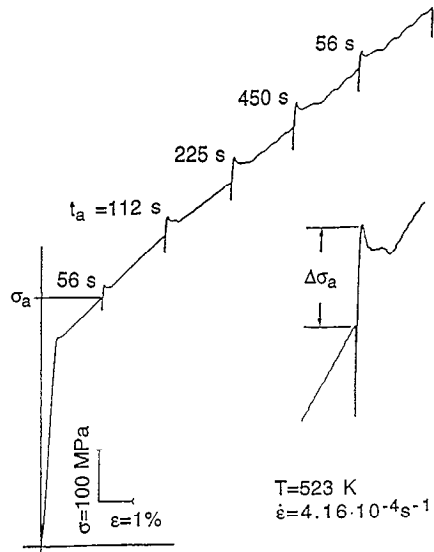


Fig. 27. A force-elongation trace showing the yield point effects on reloading a sample strain-aged for different times. Note the serrated stress strain behavior (Ti–47Al–2Cr–0.2Si).

[31,69,173]. Samples were prestrained and aged at the deformation temperature under a relaxing load for prescribed times. On re-straining the samples with the same strain rate as in prestraining, well expressed yield points were observed, examples of which are shown in Fig. 27. It is commonly accepted that the yield drop effects are related to the locking of dislocations due to atmospheres formed by different kinds of defects during the ageing periods. The experiments were performed in the temperature range of 300 to 623 K on different ternary and quaternary alloys. As an example, Fig. 28 demonstrates the dependence of the stress increments $\Delta\sigma_a$ on the ageing time t_a measured at $T = 523$ and 623 K on a Ti–48.5Al–0.37C alloy. Though quantitative differences exist among the different alloys, the results provide phenomenological evidence that a significant dislocation locking with fast kinetics occurs at relatively low temperatures of 350–623 K. The activation energies determined for strain ageing are in the range

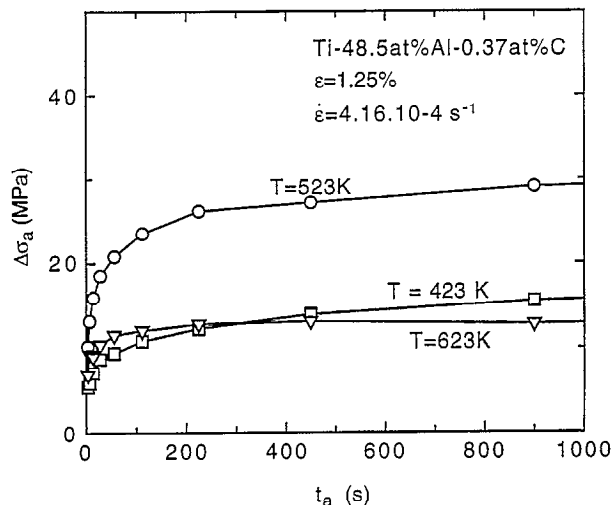


Fig. 28. Dependence of the stress increments $\Delta\sigma_a$ on the ageing time t_a measured on a Ti–48.5Al–0.37C alloy at $T = 523$ and 623 K.

$$Q_a = 0.6 - 0.8 \text{ eV}$$

depending on alloy composition [31]. These energies are significantly smaller than the self diffusion energy for $\gamma(\text{TiAl})$ of $Q_{sd} = 3.01 \text{ eV}$ [174]. Thus, a classical vacancy diffusion mechanism can clearly be ruled out. Unfortunately, little information can be deduced for dislocation pinning by the segregation of impurity atoms at the dislocation cores due to the lack of diffusion data for impurity atoms. However, it can be speculated that the ageing phenomena arise from fast diffusing impurity elements. This being the case, iron or boron atoms should be considered as recent studies have revealed that these elements have high mobilities in $\alpha_2(\text{Ti}_3\text{Al})$ [Herzig, unpublished results]. In this respect, particular interactions between the diffusing impurity elements and the jogs in screw dislocations may occur. Another possible mechanism specific for $\gamma(\text{TiAl})$ and other ordered alloys is a pinning process related to antisite defects. Clearly, the problem needs further investigation.

In regime III of the $\sigma(T)$ curve, the flow stress strongly decreases with increasing temperature and the material becomes ductile. The yield drop effects and the serrated yielding, characteristic of regime II, disappear and instead, the strain rate cycling tests exhibit smooth stress transients which cover strain intervals of 0.5 to 0.8% (Fig. 24). Typical of the alloys investigated is that $1/V$ increases in regime III with temperature, which suggests that a new thermally activated process becomes operative. Deformation at the transition from brittle to ductile material behaviour is again characterized by a relatively small activation volume, and when compared with room temperature deformation, by a high activation enthalpy. The values measured at 1100 K on alloy 1a (Table 3) are [151,163]

$$V = 47b^3 \text{ and } \Delta H = 3.16 \text{ eV.}$$

Since ΔH is close to the self diffusion energy of $\gamma(\text{TiAl})$ [174], it is concluded that a diffusion controlled mechanism contributes to deformation under these conditions. This view is supported by in situ heating studies, in which thin foils of predeformed samples were annealed at 900 K inside the TEM. Fig. 29 shows that the morphology of ordinary dislocations generated a 300 K changes into helical configurations, which are characteristic of dislocation climb. It is therefore assumed that this non-conservative dislocation mechanism initiates the transition from brittle to ductile material behavior. As has been discussed in Section 4.2, the contribution of dislocation climb to elevated temperature deformation of single-phase [157] and two-phase alloys [75] has also been confirmed by conventional TEM studies.

5.2. Dislocation multiplication

It is commonly accepted that dislocation multiplication in pure metals and disordered alloys mainly takes place through the operation of dislocation sources incorporating stress driven cross slip or climb. Multiplication of superdislocations in ordered materials by this type of sources is considered to be difficult due to the geometrical constrictions between the leading and trailing superpartials at each revolution, when large differences in the mobility of the superpartials exist [175]. According to the authors' knowledge, little information is available on the multiplication of superdislocations in TiAl. The present investigation will therefore be restricted to the generation mechanisms of ordinary dislocations, which on the other hand, have been found to determine the deformation behavior of two-phase alloys in a wide temperature range (Section 4.2).

The type of dislocation sources being preferentially activated seems to be determined by the test temperature. Multiplication at room temperature was found to be closely related to jogs in screw dislocations formed by cross slip. As has been discussed in Section 4.1, ordinary dislocations have compact cores so that cross slip is expected to be relatively easy. Thus, as has been confirmed in Fig. 26, screw dislocations contain a high density of jogs. Since the jogs are immobile in the direction of

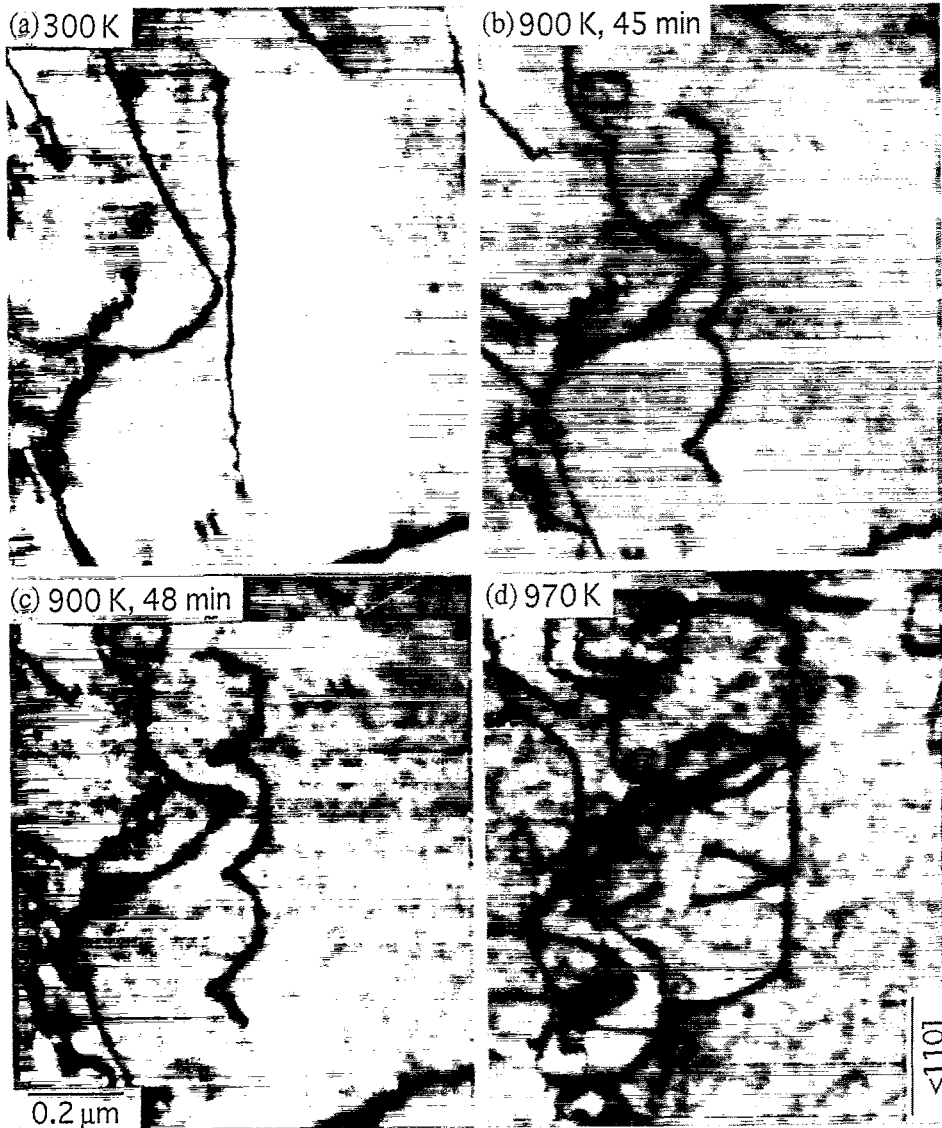


Fig. 29. Dislocation climb processes in a deformed sample observed during in situ heating inside the TEM. Ti–48Al–2Cr, predeformation at 300 K to strain $\varepsilon = 3\%$, acceleration voltage 120 kV.

the motion of the screw dislocations, dislocation dipoles are trailed at the jogs. Possible subsequent processes are illustrated in Fig. 30 and depend on the height h of the jogs [176], which determines the distance between the slip planes of the trailed edge dislocations. The dipole arms can overcome their elastic interaction and pass each other (Fig. 30c), if the applied shear stress is larger than [169]

$$\tau_d = \frac{\mu b}{8\pi(1-\nu)h}. \quad (5.10)$$

If the bowing process continues, the dipole arms can effectively behave independently of each other and act as single ended dislocation sources [176]. Fig. 31 shows a dislocation dipole trailed at a high jog, which is probably in the initial stage of this multiplication mechanism. Since the anchorings of the segments are formed by cross glide, the dislocations may expand and multiply in such a way that slip spreads from one slip plane to the next, thus, producing wide slip bands. Due to the high flow

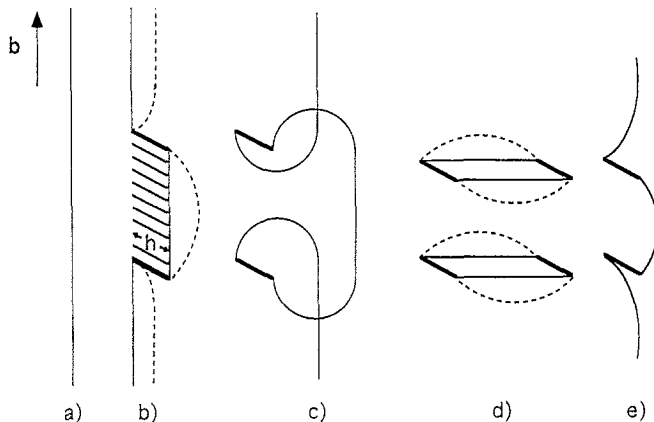


Fig. 30. Behavior of a jogged screw dislocation according to Gilman and Johnston [176]; (a and b) anchoring of the dislocation at jogs of height h ; (c) operation of dipole arms as single ended dislocation sources in case of large jogs; (d and e) trailing and termination of dipoles at small jogs. At higher stresses, the dipole arms may overcome their elastic interaction and operate as double ended dislocation sources (dashed lines).



Fig. 31. Initial stage of multiplication of an $1/2<(110>$ dislocation by cross glide. The dipole arms trailed at a high jog (arrow 1) in the screw dislocation are widely separated so that they could pass each other and may act as single ended dislocation sources. Note the emission of the dislocation loops from the interfaces (arrow 2). Ti-48Al-2Cr, compression at $T=300\text{ K}$ to strain $\varepsilon=3\%$.

stresses of the titanium aluminides relatively narrow dipoles can act as dislocation sources [152]. If an effective stress of $\tau^*=30\text{ MPa}$, as has been discussed in Section 5.1, is taken as a lower limit for τ_d , a minimum dipole height for multiplication of only $d=130b$ is calculated from Eq. (5.9). The mechanisms were also observed in front of crack tips [92], where high stress concentrations occur so that this type of sources can effectively operate (cf. Section 9).

Dipoles of smaller height, which cannot multiply at given stress, will be pinched off from the dislocation due to a second cross slip event, as illustrated in Fig. 30d and e. The process can be supported by glide of the jog along the dislocation due to unbalanced sideways components of line tension. Terminated dipoles are demonstrated in Figs. 26 and 32, respectively, and have been found to be a characteristic feature of the defect structure of both, deformed and undeformed two-phase

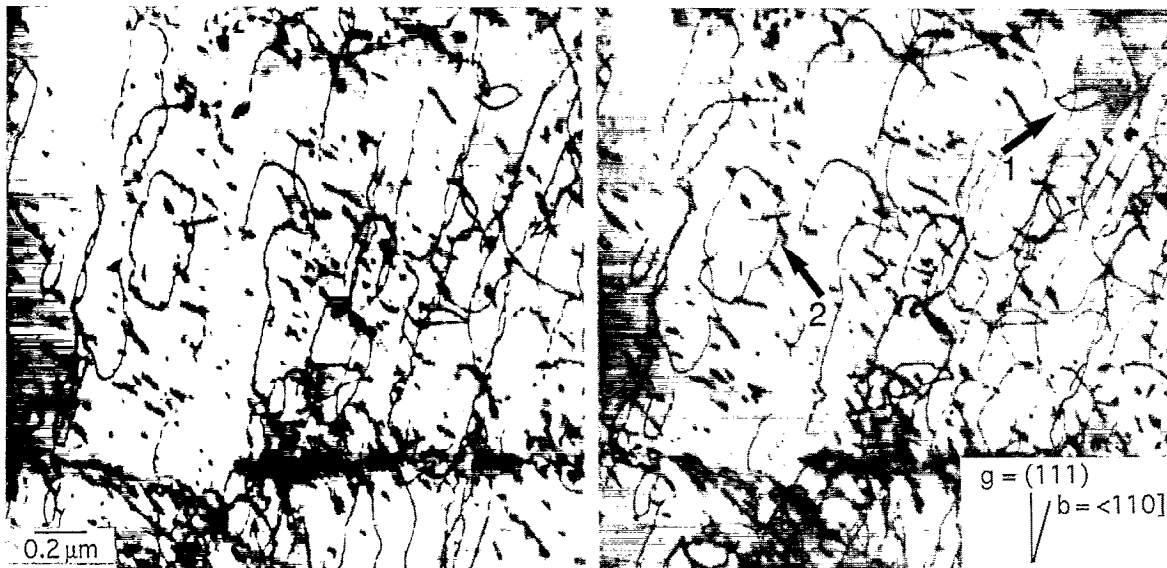


Fig. 32. Stereo pair of micrographs showing dislocation multiplication starting from pinched off dipoles. Details: (1) earlier stage of the mechanism; (2) final stage of the mechanism, two screw dislocations trailed by the dipole arms. Ti–48Al–2Cr, compression at $T = 300$ K to strain $\varepsilon = 3\%$.

alloys [68]. These defects can also operate as dislocation sources when in later stages of deformation the flow stress increases. Then the dipole arms can pass each other and operate as double ended dislocation source. Experimental evidence of this mechanism is suggested in Fig. 32, which shows pinched off dipoles being in different stages of this re-activation process. As can be confirmed by the stereo pair, dislocations of mainly screw character are trailed by the dipole arms with edge character (detail 2) suggesting that the edge components have a significantly higher mobility. The multiplication mechanisms observed at room temperature are closely related to cross slip and confirm the earlier models proposed by Gilman and Johnston [176]. Considering the easiness of cross slip in γ (TiAl) at room temperature, there is probably a sufficient number of sources available under these deformation conditions.

As has been discussed in Section 5.1, deformation at elevated temperatures involves extensive climb resulting in complex dislocation configurations. Therefore, the multiplication mechanisms can hardly be deduced from postmortem TEM observations. In the present study, direct information were obtained from in situ heating experiments performed inside the TEM. The samples used were predeformed at 300 K to strain $\varepsilon = 3\%$ which introduced sufficient dislocations for observation and certainly a small supersaturation of intrinsic point defects due to the non-conservative glide processes discussed in Section 5.1. Apart from qualitative differences, the defect structure is similar to that of undeformed material, since processing routes of two-phase alloys often involve thermomechanical treatments and rapid quenches. During the in situ heating experiments, the dislocations moved under the combined action of thermomechanical stresses and osmotic climb forces so that information on potential multiplication mechanisms at elevated temperatures could be obtained. The experiments were performed between 800 and 930 K, which corresponds to the transition between brittle and ductile behavior and to the intended service temperature of the material. Low acceleration voltages of 120 and 200 kV were, respectively, used in order to avoid radiation damage.

Multiplication at elevated temperatures was found to start from different defects incorporating climb suggesting that different variants of the classical Bardeen and Herring dislocation climb source [177] were operative. Fig. 33 demonstrates the growth of climb sources during a long period of about

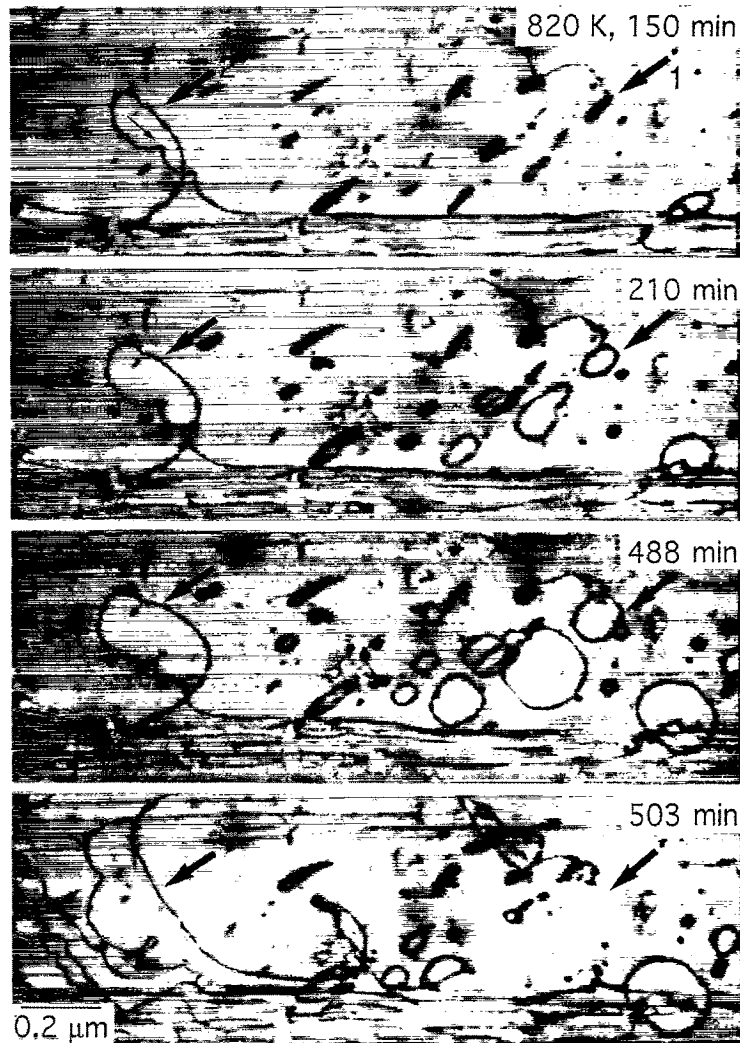


Fig. 33. Operation of Bardeen and Herring dislocation climb sources during an in situ heating experiment inside the TEM at 820 K. Details: (1) nucleation and growth of prismatic dislocation loops, (2) expansion of a dislocation loop containing two jogs (small arrow). After one cycle of the source, a new dipole is generated so that the mechanism is regenerative. Ti-48Al-2Cr, pre-deformation at 300 K to strain $\varepsilon = 3\%$.

350 min by a sequence of micrographs of an in situ study performed at 820 K. Accordingly, dislocations were generated by the nucleation and growth of prismatic loops (arrow 1). Since the expansion of each loop is realized by the removal of an atomic plane, the mechanism seems to be exhausted after only one cycle of the source. The expanding loop designated with arrow 2 contains a jog so that climb on different atomic planes occurs. After one cycle of the source, a new dipole is generated so that the mechanism is regenerative. The climb processes often lead to the formation of spiral sources, which generate complex configurations of interconnected multiple loops, as has already been demonstrated in Fig. 29.

The character of the point defects involved in the formation of the climb sources was not identified in the present study. The point to note is, however, that the critical vacancy concentration c/c_0 required to operate a Bardeen and Herring source is relatively low. For a loop expanding from a source of length L , the critical value is [178]

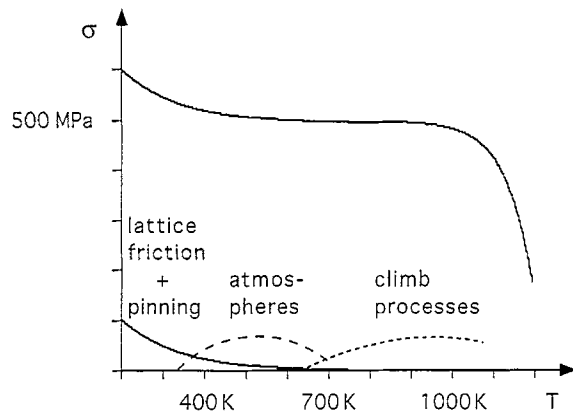


Fig. 34. Proposed mechanisms contributing to the glide resistance of ordinary dislocations in two-phase titanium aluminides.

$$\ln \frac{c}{c_0} \geq \frac{\mu b \Omega}{L 2\pi(1-\nu) kT} \ln (L\alpha/1.8b), \quad (5.11)$$

where Ω is the atomic volume and $\alpha=4$. For the present experimental conditions $T=820$ K and $L=150-350b$, the values $c/c_0=3-1.7$ are obtained. These supersaturations are small in comparison to those produced initially after rapid cooling, which is often involved in the processing route of two-phase titanium aluminides. Thus, Bardeen and Herring sources can probably operate throughout the entire period of annealing out of excess vacancies and are seen to influence the initial stages of creep (cf. Section 8). In addition to the mechanisms discussed here, dislocations can also be generated at lamellar interfaces, which will be described in Section 6.

In summary of the present section, it may be concluded that the motion of ordinary dislocations in two-phase titanium aluminides over a wide range of temperature is impeded by a high glide resistance. Such dislocations mainly facilitate the deformation process. The mechanisms which are believed to cause the glide resistance are schematically illustrated in Fig. 34 for the temperature range investigated. At room temperature, the dislocation velocity is controlled by a combined operation of localized pinning and lattice friction, while locking of the dislocations due to the formation of atmospheres of yet unknown defects occurs in the temperature range of 400–750 K. Starting from the transition from brittle to ductile material behavior, the dislocation velocity seems to be determined by dislocation climb. The mechanisms relieve one another so that the total flow stress remains constant over a wide temperature range as indicated in Fig. 34.

The activation parameters associated with these mechanisms are determined by the bonding strength, the impurity content and the diffusion properties of the material. Among different two-phase alloys activation volumes and activation energies can therefore change with composition and microstructure as these inherent material properties do. In particular, it now becomes plausible that the activation parameters are less dependent on microstructure. Two-phase TiAl alloys of technical significance have typically a total content of interstitial impurities of 700 to 1000 ppm, which certainly contributes significantly to the high glide resistance in addition to the lattice friction of the material due to its covalent bonding. According to the present study, additional glide obstacles are formed at jogs in screw dislocations. These jogs can give rise to various interactions with dislocations, which will be investigated in Section 7.4. It is interesting to note that several features of the glide resistance reported here for two-phase alloys have been also observed in single phase alloys [179,180]. There is much evidence that the multiplication of ordinary dislocations is relatively easy. Due to their compact core structure these dislocations can easily cross glide so that various types of single and double ended

Frank–Read sources can operate. At elevated temperatures, climb-assisted multiplication occurs due to various modifications of Bardeen and Herring sources. However, little information is available on the multiplication of superdislocations, a field which requires further investigation.

6. Interface related deformation phenomena

The assessment of the strength properties (Section 3) has revealed that nearly all mechanical properties of two-phase titanium aluminides are improved when the alloys have a fully-lamellar microstructure provided the colony size was suitably controlled [54]. Much research interest has therefore been focused on elucidating structural details of the lamellar morphology and the related microprocesses of plasticity. Investigation of these problems is the subject of this section.

6.1. Structural details of lamellar interfaces

The lamellar structure is the result of phase transformations and ordering reactions occurring during solidification, which depend on composition and cooling rate [15,20,181,182] as has been discussed in Section 2. When alloys with nearly equiatomic compositions are prepared by usual ingot metallurgy, the γ phase is formed by the nucleation and growth of γ platelets with the $L1_0$ structure at the expense of the α phase with the disordered hcp structure (Fig. 35) [88]. At lower temperatures, the α phase undergoes an ordering reaction to the α_2 phase with the DO_{19} structure. As shown in Section 2.1, the two phases constituting the lamellar structure have the epitaxial relationships (2.1). In the $L1_0$ structure, the $[1\bar{1}0]$ direction differs from the two $\langle 01\bar{1} \rangle$ directions on the (111) plane while the three $\langle 11\bar{2}0 \rangle$ directions on the basal plane of the DO_{19} structure are all equivalent. Since there are six possible orientations of $[110]_\gamma$ with respect to $\langle 1120 \rangle_{\alpha_2}$, the γ phase has a domain structure composed of six differently oriented variants (Fig. 35). Thus, in the lamellar structure, three distinct γ/γ interfaces occur, which can formally be described in terms of rotations of one lamella relative to its neighbour by multiples of 60° about $(111)_\gamma$, so that the close packed directions nearly align. The adjacent lamellae match exactly and have a $(111) [11\bar{2}]$ true twin orientation when the rotation is 180° . In the case of 60° rotations, the matching is only approximate and the neighbouring lamellae form a pseudo-twin. Rotations of 120° result in an order-fault boundary and the adjacent

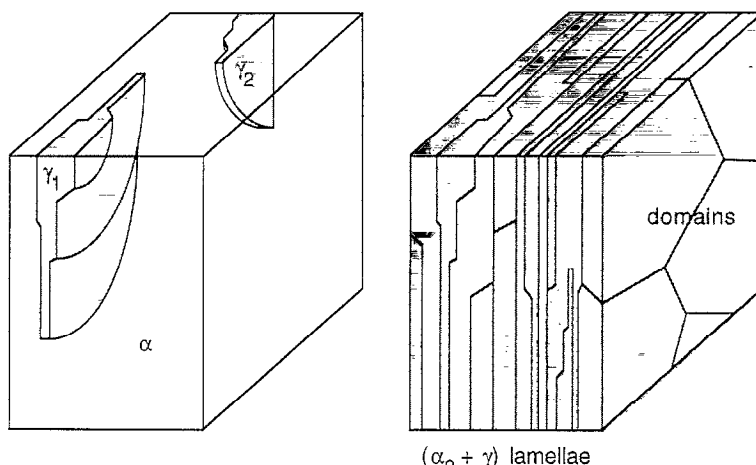


Fig. 35. Formation of the lamellar microstructure by the nucleation and growth of γ platelets from the α phase. The orientation of the γ variants in the individual domains can be described by multiples of 60° about $(111)_\gamma$. After [88], changed.

lamellae are in matrix/matrix relation if the tetragonality of the γ phase and the different atomic species are ignored. The misorientations across domain boundaries are the same as those of lamellar interfaces, but the habit plane is usually not of type {111}.

Interfaces in lamellar microstructures have been studied since 1970 by both conventional and high resolution electron microscopy [51,68,141,183–190]. While some differences exist in the details, the observations essentially confirm the general predictions of Frank and van der Merwe [191] that the structure of the interfaces is mainly determined by the mismatch occurring between adjacent lamellae. In case of α_2/γ interfaces, a significant mismatch occurs due to the differences in crystal structure and lattice parameters. Similarly, misfit strains are present across the 60° and 120° interfaces of γ variants due to their tetragonality. For the unrelaxed state of these interfaces, misfit strains of about 1% are expected, which cannot be accommodated elastically. The interfaces therefore contain arrays of misfit dislocations, which reduce the misfit strain energy and improve the interfacial coherency by producing local relaxations. As an example, Fig. 36 demonstrates the mismatch structure of a 120° γ/γ interface in a PST crystal. The observed cross-grid of screw dislocations can be attributed to the accommodation of the pure shear misfit occurring in this case [188].

The processing routes of polycrystalline materials often involve rapid quenchings or significant hot working resulting in changes of the microstructure and apparently more complex interfaces. TEM studies performed on a lamellar Ti–44Al alloy [185] have revealed $1/2\langle 110 \rangle$ and $1/6\langle \bar{1}\bar{1}\bar{2} \rangle$ interfacial dislocations, which can be associated with the rotational misfit. In addition, dislocations with the Burgers vector $b = 1/2\langle \bar{1}12 \rangle$ and $b = \langle 101 \rangle$ were identified, which undergo various dissociations and are not correlated with the interfacial misfit. Fig. 37 demonstrates the typical features of the lamellar microstructure of a polycrystalline Ti–48Al–2Cr alloy. Hot isostatic pressing of the material was performed at 1473 K and 1.7 bar for 4 h followed by relatively slow cooling to room temperature at a rate of 10 K/min. The thickness of the lamellae ranges from about 10 nm to 1 μm and the fraction of α_2 lamellae is 5–10%. Most of the interfaces join therefore differently oriented γ lamellae. Fig. 37a shows the atomic structure of an α_2/γ interface of the same alloy. These interfaces are mostly composed of coherent terraces parallel to $(111)_\gamma$ and arrays of regularly spaced ledges about 20 nm apart (arrowed in Fig. 38a). Thus, the overall habit plane of the α_2/γ interface often deviates from the ideal orientation relationship (Section 2.1). The ledges have been associated with Shockley partial dislocations, an observation which suggests that the growth and dissolution of α_2 platelets in the lamellar microstructure is accomplished by the passage of these dislocations on alternate $(111)_\gamma$ planes [189]. Fig. 37b and c demonstrate the interfaces between 120° and 180° – γ variants, respectively, which represents strain accommodation due to misfit dislocations and perfect matching of adjacent γ lamellae.

One particular feature of the lamellar structure in polycrystalline technical alloys is that the interfaces often contain tilt misfit. As demonstrated in Fig. 37b, this tilt component is realized by interfacial dislocations with an additional $(111)_\gamma$ plane parallel to the interface γ_1/γ_2 so that they may be associated with $b = 1/3[111]$. These dislocations are less efficient in accommodating the rotational misfit between γ variants and may lead to high interfacial energies. The origin of these extraneous interfacial dislocations is not clear. It is speculated that they are formed as a result of phase transformations and migration of the lamellar boundaries, which occur after solidification leading to a change of the misfit character of the interfaces. Another possible process is the trapping of matrix dislocations at the interfaces and their reaction with pre-existing misfit dislocations. This process is seen to be supported by thermally induced stresses upon cooling. It should be mentioned, however, that in other cases tilt misfit out of the {111} interfacial plane has rarely been observed, though particular attention had been given [192]. For these reasons, the structure of the interfaces is expected to be strongly dependent on the processing route and thermal history of the material. This view is supported by TEM observations on hot-rolled sheet material of an alloy Ti–47Al–1Cr with additions of Nb, Mn, Si and

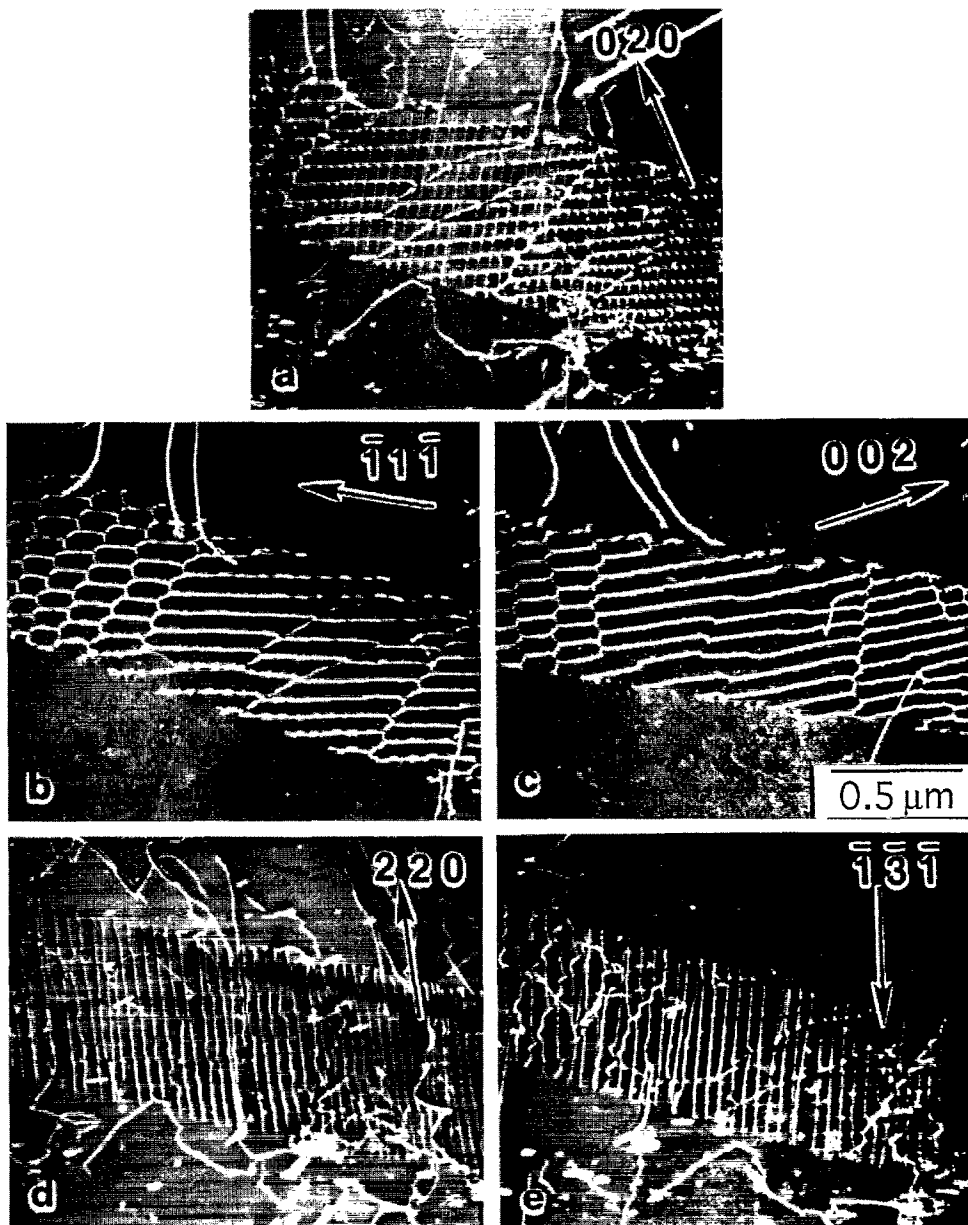


Fig. 36. Weak-beam micrographs of misfit dislocations in a lamellar interface between 120° rotational γ variants. The cross-grid of screw dislocations appears to be adequate for accommodating the total shear occurring at this type of interfaces. The arrows are parallel to g : (a) $g = 020$, (b) $g = \bar{1}\bar{1}\bar{1}$, (c) $g = 002$, (d) $g = 220$; (e) $g = \bar{1}\bar{3}\bar{1}$. The horizontal dislocations have the Burgers vector $b = 1/2[\bar{1}\bar{1}2]$ and the vertical dislocations have $b = 1/2[110]$. On the left-hand side of the boundary, the reaction of the dislocations forms a hexagonal network with segments containing $b = [011]$. Ti-50Al PST crystal. (Micrographs: Kad and Hazzledine [188]).

B. As demonstrated in Fig. 38 for an α_2/γ interface, the lamellar boundaries in these sheets exhibit a significant tilt component. This is accommodated by a high density of interfacial dislocations with a Burgers vector out of the interfacial plane. This interfacial structure probably reflects the extensive structural changes of the lamellar morphology during hot rolling of the material.

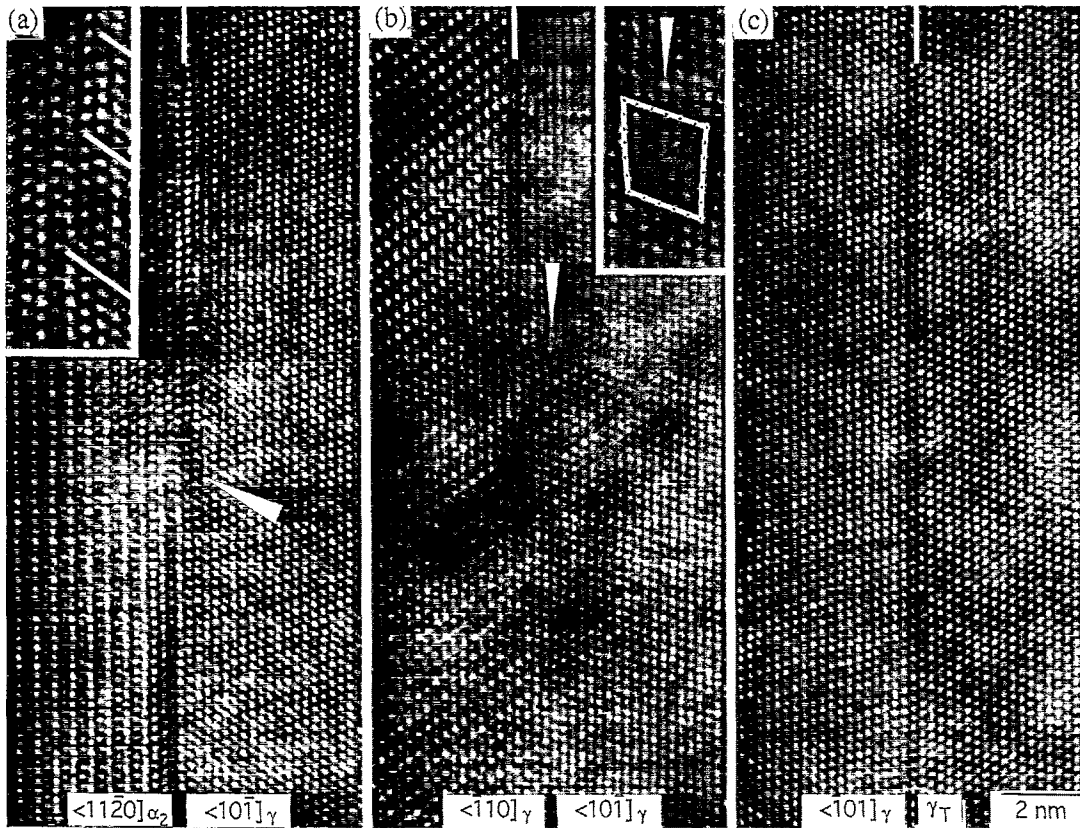


Fig. 37. Structural features of a lamellar Ti-48Al-2Cr alloy; (a) high resolution image of an α_2/γ interface; (b) semicoheres interface between 120° rotational variants γ_1/γ_2 with matrix/matrix relation. Note the arrowed misfit dislocation; (c) coherent interface between 180° rotational variants γ/γ_T with true twin orientation.

6.2. Coherency stresses of lamellar interfaces and dislocation generation

In spite of the strain accommodation by the interfacial dislocations, a significant misfit seems to remain at the interfaces resulting in high coherency stresses [150,155]. This is indicated by characteristic structures of dislocation loops adjacent to the interfaces (Fig. 39). The Burgers vector of the loops was identified as $b = 1/2<110>$, which in most cases was not contained in the interfacial plane. The loops were probably formed by reactions of interfacial dislocations. A possible mechanism may involve the misfit dislocations with the Burgers vectors $b = 1/3[111]$ and $b = 1/6[11\bar{2}]$ according to

$$1/3[111] + 1/6[11\bar{2}] \rightarrow 1/2[110]. \quad (6.1)$$

The reactant $1/2[110]$ dislocations were probably emitted from the interfaces due to the residual coherency stresses. The process could be confirmed by in situ heating experiments, in which the temperature was repeatedly varied between 300 and 973 K. Fig. 40 demonstrates the observed change of the mismatch structures adjacent to an α_2/γ interface. The loops were emitted at elevated temperatures around 970 K, where the friction forces impeding dislocation glide were probably reduced due to thermal activation.

The magnitude of the coherency stresses has been estimated by analyzing the curvature of the dislocation loops [150,155]. The insert of Fig. 39 demonstrates line tension configurations of $1/2<110>$ dislocations which were calculated with the help of the model of DeWitt and Koehler [193].

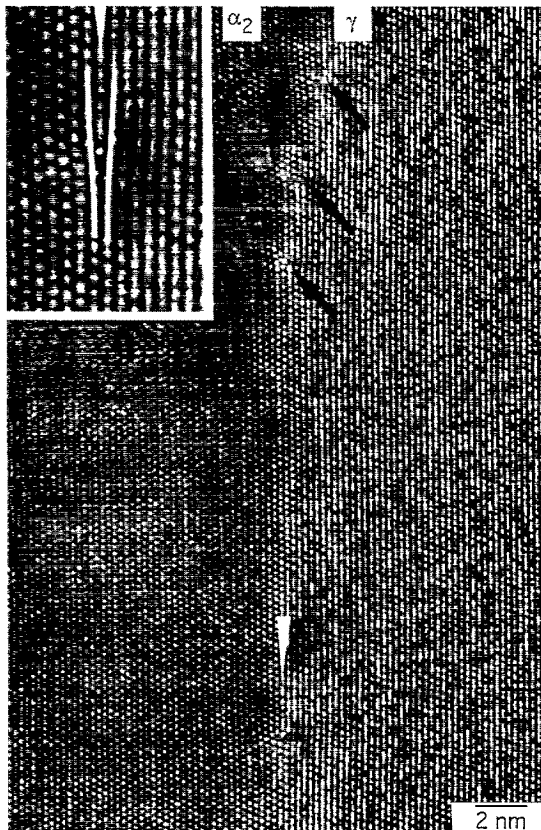


Fig. 38. High resolution image of an α_2/γ interface in sheet material of an alloy Ti-47Al-1Cr with additions of Nb, Mn, Si, and B. Note the significant tilt misfit and the high density of interfacial dislocations (arrowed) with a Burgers vector out of the interfacial plane.

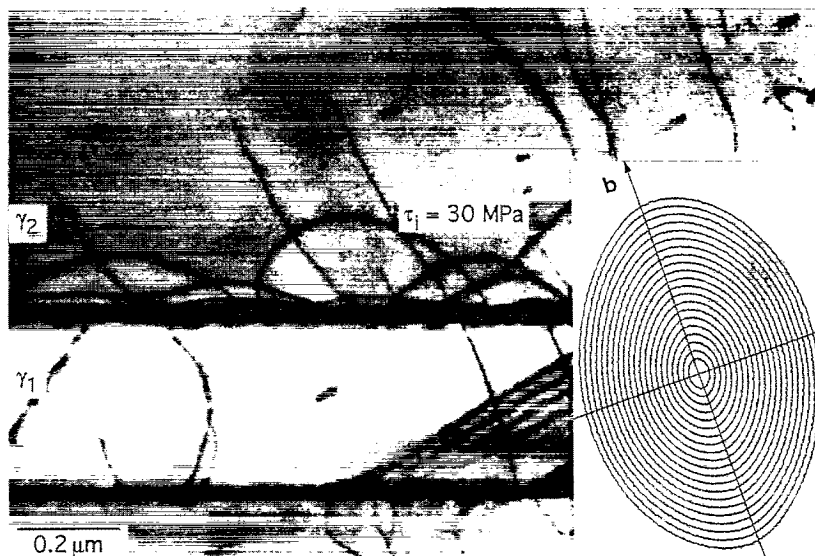


Fig. 39. Dislocation loops with Burgers vector $b = 1/2\langle 110 \rangle$ emitted from a semicoherent interface γ_1/γ_2 under the action of coherency stresses. The insert shows line tension configurations calculated for different shear stresses and projected into the $\langle 101 \rangle$ foil plane. By comparison to the segment indicated a shear stress $\tau_i = 30 \text{ MPa}$ was attributed. (Ti-48Al-2Cr).

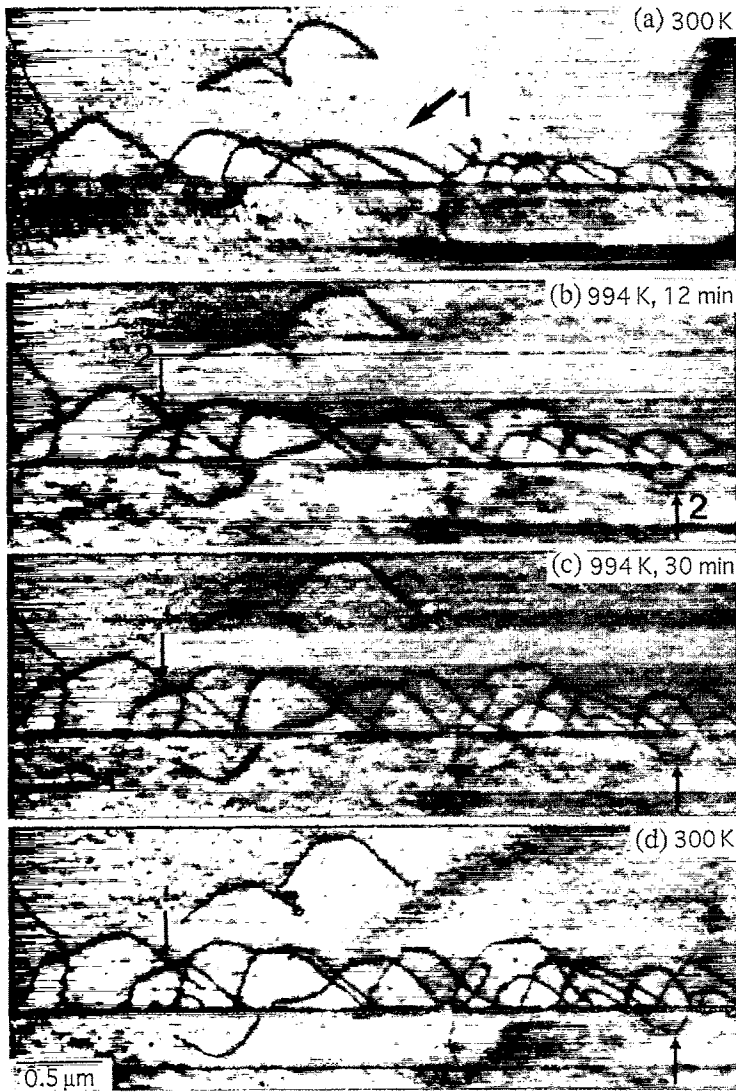


Fig. 40. Generation of dislocation loops at a semicoherent α_2/γ interface during in situ heating inside the electron microscope. The loops indicated by arrow (1) were probably generated in a first run of the experiment in which the foil was heated up to 994 K for 30 min and afterwards cooled down to 300 K. Fig. 2b demonstrates the formation of new loops (arrow 2) in the second run of the experiment in which the sample was again heated up to 994 K for 60 min. Foil orientation close to $\langle 11\bar{2} \rangle$. Ti-48Al-2Cr. Acceleration voltage 200 kV.

The line tension loops were calculated for different shear stresses and projected into the foil plane of the imaged dislocations. Thus, from comparing the calculated loops with the imaged ones, the coherency stresses could be determined. The results obtained are summarized in Fig. 41 as a frequency distribution, which leads to an average coherency stress $\tau_i = 130$ MPa. Similar values of coherency stresses have also been determined by convergent beam electron diffraction [194]. The room temperature flow stress of the material investigated here is $\sigma_a = 430$ MPa, from which a shear stress $\sigma_a/f = 140$ MPa can be deduced. Thus, the coherency stresses are of the same order of magnitude as the shear stresses applied during deformation. Due to the broad variation of τ_i (Fig. 41), a long-range internal stress field is probably generated, which changes in amplitude and direction. The combined action of these fluctuating stresses and the high density of misfit dislocations can have various implications on the strength properties and the structural stability of the material. One particular consequence

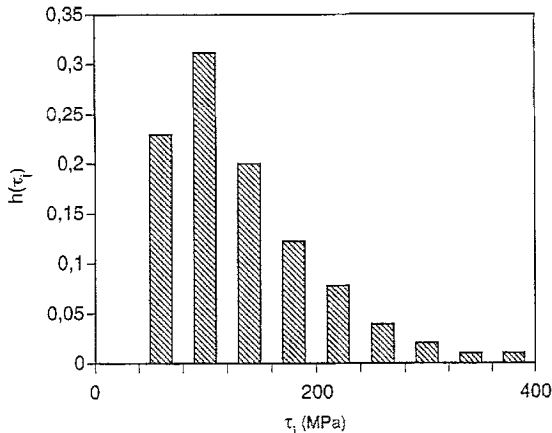


Fig. 41. Distribution $h(\tau_i) = \Delta N/N_0$ of the coherency stresses acting on dislocation loops emitted from semicoherent interfacial boundaries of a polycrystalline Ti-48Al-2Cr alloy. ΔN is the number of segments found in the stress intervals and $N_0 = 190$ is the total number of analyzed loops.

is the initiation of glide processes at the lamellar interfaces. The dislocation loops described above are situated on {111} planes obliquely oriented to the interfaces and have a Burgers vector $1/2\langle 110 \rangle$ out of the interfacial plane. Since the loops are strongly bowed out by the coherency stresses they can easily be detached from the interfaces and serve as glide dislocations for the translation of the shear deformation across the lamellae. Extended glide processes of $1/2\langle 110 \rangle$ dislocations starting from lamellar interfaces were found to be a significant feature of the defect structure of samples deformed under various conditions. As an example, Fig. 42 demonstrates the dislocation structure adjacent to a semicoherent γ/γ interface in a Ti-48 Al-2Cr alloy deformed at 300 K.

The interface related generation of glissile dislocations has different implications on the strength properties depending on test temperature. The mechanism certainly supports deformation processes at ambient temperatures where the dislocation mobility is low. Furthermore, as will be shown in Sections

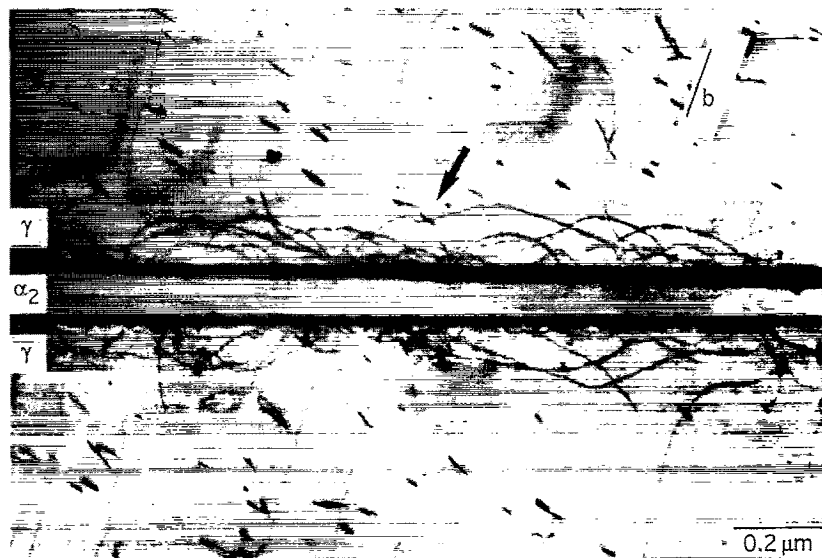


Fig. 42. Structure of ordinary dislocations with Burgers vectors $b = 1/2\langle 110 \rangle$ observed after room temperature compression to strain $\varepsilon = 3\%$. Glide processes were initiated at dislocation loops pre-existing at α_2/γ semicoherent interfaces γ_1/γ_2 (arrowed). Ti-48Al-2Cr, foil orientation close to $\langle 101 \rangle$.

7.1 and 9, the emission of the dislocation loops from the interfaces can relieve stress concentrations in front of deformation twins and crack tips [92]. In this respect, the mechanism is certainly beneficial for the ductility and damage tolerance of the material at ambient temperatures. On the other hand, the changes of the mismatch structures observed at elevated temperatures (Fig. 40) probably contribute to the degradation of the strength properties occurring under these conditions. In particular, the dislocation emission from the interfaces is expected to contribute to the high primary creep rate of the material (cf. Section 8). Another interface related deformation mechanism occurring at elevated temperatures consists probably in the formation of the 9R structure, as described in Sections 4.2 and 8.

6.3. Twin nucleation and growth

As has been described in Section 4.2, the importance of twinning has long been recognized as deformation mechanism of γ (TiAl). However, many aspects of the mechanism have been elucidated only in recent years when a number of detailed TEM observations became available. This concerns in particular the generation of twins. Since the spontaneous formation of a large twin is difficult to envisage, separate consideration is usually given to the formation of a small twin region (embryonic twin) and to its subsequent growth into a large twin [149]. For twin nucleation, basically two approaches have been adopted. Accordingly, twins can nucleate homogeneously in a defect free region of the crystal when the interfacial energy is low and very high stresses are present. Alternatively, twin nucleation may occur at lattice defects with a favorable atomic configuration which can be rearranged into an embryonic twin.

For γ (TiAl) several heterogeneous nucleation mechanisms have been proposed [94,119,195], which basically are related to the dissociation of superdislocations. Accordingly, the expansion of stacking fault loops resulting from the dissociation can lead to twin nucleation. The nucleation of microtwins due to the superposition of extended SESF on alternate {111} planes has been proposed by Singh and Howe [196]. The mechanisms have been discussed in a recent review [149]. A pole mechanism, based on the dissociation of jogged $1/2\langle 110 \rangle$ dislocations and the climb expansion of a Frank partial dislocation has recently been proposed by Yoo and Fu [197]. In lamellar two-phase titanium aluminides deformation twins mostly originate from the interfacial boundaries (Figs. 20 and 21), which also suggests a heterogeneous nucleation. Direct confirmation could be obtained by high resolution TEM studies of deformed materials, examples of which are shown in Fig. 43. Accordingly, the twins are preferentially formed at the misfit dislocations of the interfaces having a Burgers vector component out of the interfacial plane [141,150]. Fig. 43a shows the formation of a stacking fault at a misfit dislocation of an α_2/γ interface, which may be considered as the initial stage of twin nucleation. Fig. 43b demonstrates twin generation at a γ/γ interface. The two γ lamellae have a true twin orientation but exhibit locally a significant tilt misfit. The micrographs reveal that this misfit is accommodated by an array of interfacial dislocations. Two narrow twins (1) and (2) six and nine {111} planes thick, respectively, are generated at the misfit dislocations. The defect configuration designated with (3) apparently shows the initial stage of twin nucleation. Since the misfit dislocations have a Burgers vector component parallel to the twinning shear direction $\eta_1 = [\bar{1}\bar{1}\bar{2}]$, they can give rise to the formation of the related twinning partials. The process is certainly supported by the high residual stresses present at the interfaces as discussed in Section 6.2. Likewise, coherency stresses and mismatch structures may support twin nucleation at grain boundaries of equiaxed materials as exemplified in Fig. 43c.

The structure of the K_1 twinning plane (111) apparently depends on the deformation temperature. High resolution studies of twins propagated at room temperature revealed the fully coherent and highly perfect nature of the shear planes [141,145,150]. However, as demonstrated in Fig. 44a, there are one

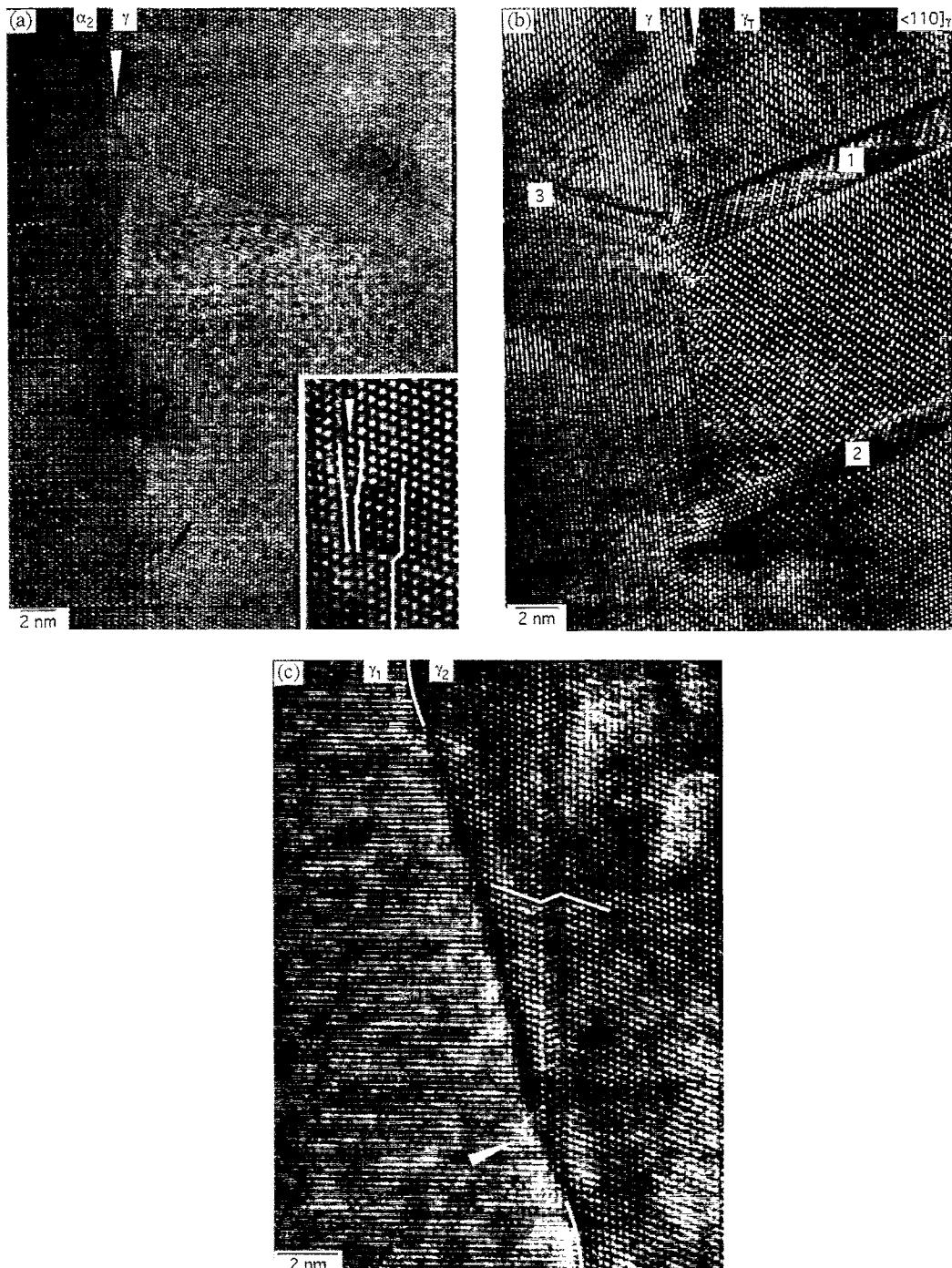


Fig. 43. Heterogeneous nucleation of deformation twins in different two-phase titanium aluminide alloys. (a) Formation of a stacking fault at a misfit dislocation of an α_2/γ interface. Sheet material of an alloy Ti-47Al-1Cr, with additions of Nb, Mn, Si, and B. Tensile deformation at 300 K to failure at $\varepsilon_t = 2.8\%$. (b) Generation of deformation twins at an interface γ/γ_T between γ variants with true twin orientation. The interface exhibits a significant tilt component, which is accommodated by an array of misfit dislocations (arrowed). The narrow twins (1) and (2) are nucleated from the misfit dislocations. The defect configuration designated with (3) probably represents an embryonic twin. Ti-48Al-0.37C, compression at 300 K to strain $\varepsilon = 3\%$. (c) Generation of a deformation twin at a small angle grain boundary, alloy and deformation conditions as in (a).

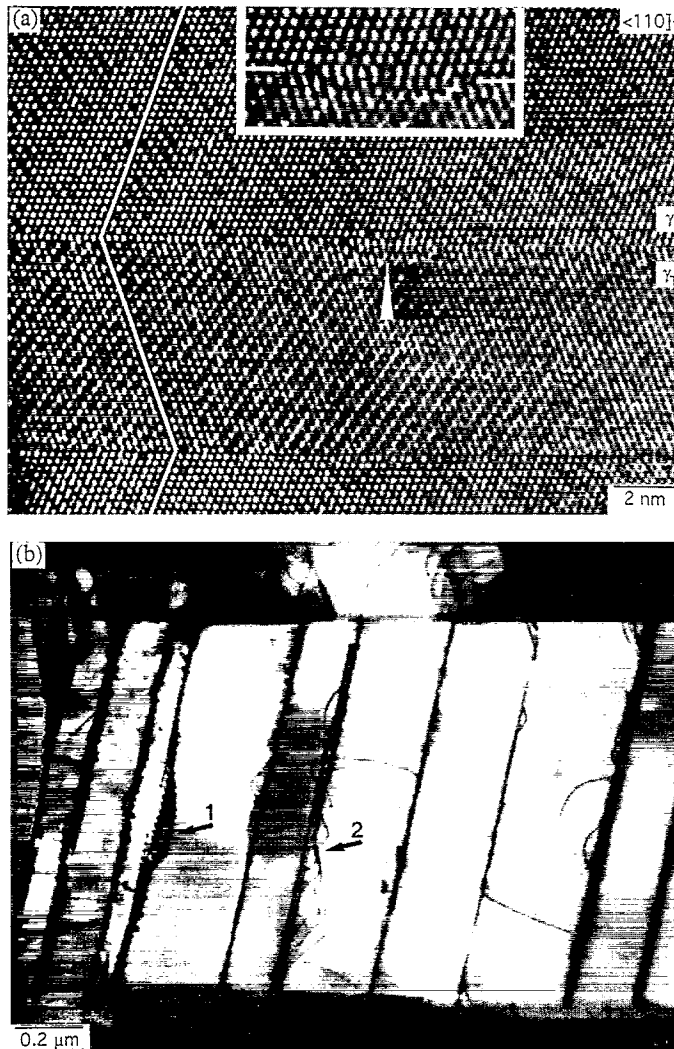


Fig. 44. Structure of deformation twins in a Ti-48Al-2Cr alloy. (a) Atomic structure of the K_1 -shear plane of a twin propagated at $T = 300$ K. Note the one-plane ledges (arrowed) in one of the twin matrix/interfaces. (b) Twin propagation at elevated temperatures. Note the formation of complex dislocation networks (arrow 1) at the twin/matrix interfaces and the emission of dislocation loops (arrow 2). Tensile deformation at $T = 1073$ K to failure at $\varepsilon_f = 10.2\%$.

plane ledges (arrows) in these interfaces. These suggest the twins to grow through the propagation of Shockley partials [94]. Twins generated at elevated temperatures are often fragmented and exhibit rough interfaces (Fig. 44b). It is speculated that these structural features arise from complex reactions between the Shockley partial dislocations and matrix dislocations which have been incorporated into the twin/matrix interface. In this way, the Shockley partial dislocations can be converted to perfect dislocations. Climb of these dislocations probably give rise to the observed complex interfacial dislocation networks (arrowed in Fig. 44b). Electron microscope *in situ* deformation studies have been used for dynamic observations of twin propagation and growth. A polar source of a partial dislocation bounded by a perfect dislocation has been observed in a single phase Ti-54Al alloy [198]. Jin and Bieler [199] initiated twin propagation in a Ti-47.4-1.9Nb-2.2Cr alloy by an ‘electron beam illumination method’. The twins appeared to grow by successive formation and bowing out of twinning dislocations from grain boundaries on adjacent {111} planes. The mechanism was suggested to be

supported by local stress concentrations. While the proposed pole mechanisms certainly help to explain the slow twin growth, the question arises as to whether they can account for the rapid formation of a twin of finite thickness. This problem has been recognized in the literature for many years but nevertheless remains unsolved.

As a summary of the present section, the following conclusions can be made. In lamellar titanium aluminides, various types of coherent and semicoherent interfaces occur. The structure of the interfaces depends on the processing route and thermal history of the material, respectively, and is often more complex than expected from the rotational misfit and differences in lattice constants. Semicoherent interfaces are characterized by dense mismatch structures and high coherency stresses. These structural features support the generation of perfect and twinning partial dislocations. Misfit dislocations with a favorable core configuration can be rearranged into twin embryos. Several aspects of the growth process of twins by polar sources are not yet solved and need further investigation. This concerns in particular the factors limiting the lateral growth of the twins and the dependence of these processes on temperature. One feature in common to both interface related twin nucleation and generation of perfect dislocations (described in Section 6.2) is certainly their beneficial effect on the material ductility. Due to the high density of misfit dislocations, a fine dispersion of deformation twins can be generated at the interfaces, which certainly helps to compensate for the limited number of operative slip systems. The glide resistance provided by the lamellar interfaces will be discussed in Section 7.1.

7. Strengthening mechanisms

In the previous sections, it was shown that many factors contribute to the mechanical behavior of the titanium aluminides. As a high strength is required for many technical applications, several metallurgical techniques have been applied to strengthen the material. These involve grain refinement, solid solution and precipitation hardening, and work hardening. In this section, the micromechanisms being relevant for the strengthening will be examined and assessed with respect to their potential for the further alloy design.

7.1. Grain refinement

In most technical applications, titanium aluminides will most likely be used in polycrystalline form. Much attention has therefore been focused on the effect of grain size on the material strength. As with all metals yield and fracture stresses increase as the grain size decreases. Thus, the strength properties are often described in terms of Hall–Petch relations (Eq. (3.1)). One rationalization of this model is that a dislocation pile up at a grain boundary in one grain can generate sufficiently large stresses to initiate glide in an adjacent grain. In most analyses of the experimental data, the microstructure has been characterized by a single length parameter, as grain size, lamellae colony size or lamellar spacing. On the basis of this approximation, Hall–Petch relations have been revealed for several classes of γ -based alloys (cf. Section 3.1). Examples of this analysis are given in Fig. 9. However, the evaluation is not always straight forward, since the microstructures are mostly quite complex and rich in detail encompassing different length parameters being relevant for the dislocation mean free path. Concerning the approximations made, the situation seems to be relatively clear for equiaxed near gamma microstructures. For these materials, the Hall–Petch constant is typically in the range $k_y = 0.9\text{--}1.3 \text{ MPa } \sqrt{\text{m}}$, which explains about 70% of the yield stress of fine grained material [18,19,61]. Particular problems seem to arise for the analysis of duplex materials, where the grain sizes of the $(\alpha_2 + \gamma)$ colonies and equiaxed γ grains are often quite different and, furthermore, the

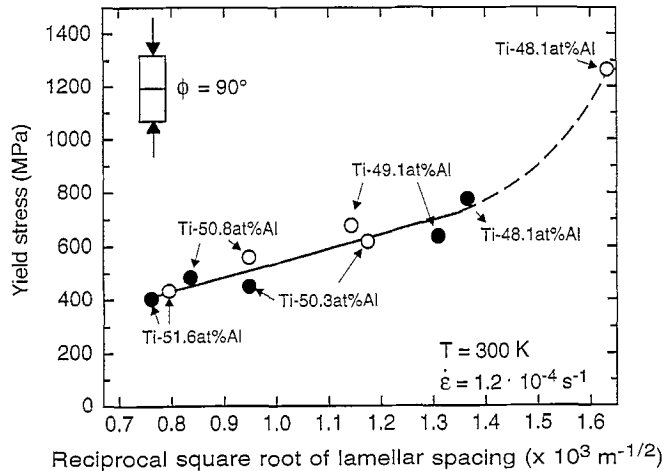


Fig. 45. Yield stress of PST crystals as a function of the reciprocal square root of the average lamellar spacing, for lamellae orientations perpendicular to the loading axis, $\phi = 90^\circ$. Open and closed circles show crystals grown at 2.5 mm/h and 5 mm/h, respectively. The sharp increase of the yield stress of Ti-48Al grown at 2.5 mm/h is due to the high volume fraction of α_2 plates. (Courtesy: Umakoshi et al. [56]).

relative contributions of the two constituents to the total deformation of the polycrystal are unknown. Similar uncertainties exist for lamellar microstructures as flow stresses might be associated with colony sizes, domain sizes, lamellar spacings, and the separation distance of α_2 lamellae. However, there is significant supporting evidence that the lamellar boundaries are very effective barriers for glide processes. This has been first recognized in PST crystals by the strong yield stress anisotropy (Fig. 8) [56–58]. The effect has also been observed on polycrystalline materials with a preferred orientation of the lamellae [162,200]. As the anisotropy of the deformation behavior was to a much lesser extent reflected in the activation volume, it was suspected that the lamellar barriers provide athermal glide obstacles [162]. The flow stress anisotropy of PST crystals has been analyzed by Umakoshi et al. [56] by considering different structural parameters of the lamellar morphology. Fig. 9 shows the variation of the flow stress with the domain size and the lamellar spacing, respectively, which was determined for shear deformation parallel and across the lamellae [57]. The evaluation revealed that the α_2/γ interfaces provide the highest barrier strength when compared with γ/γ interfaces or domain boundaries. The barrier strength of the α_2 lamellae apparently depends on their orientation with respect to the deformation axis. This has been referred to the glide anisotropy of the α_2 phase by considering the Schmid factors for prismatic slip. As for lamellae orientations of $\phi = 90^\circ$, no prismatic slip occurs and as pyramidal slip requires very high shear stresses [201–204], the α_2 lamellae provide the highest glide resistance in this orientation. This view is supported by the experimental finding that the yield stress for lamellae orientations of $\phi = 90^\circ$ strongly increases with the volume fraction of α_2 lamellae (Fig. 45) [56].

Direct structural evidence of the operation of the Hall–Petch mechanism in equiaxed materials is relatively rare as dislocation pile ups are barely observed. This may in part be due to the fact that most TEM observations were performed with conventional instruments operated at low acceleration voltages so that the electron transparent foils were relatively thin and significant rearrangements of the pile ups are likely to occur. The efficiency of lamellar interfaces as glide obstacles has been recognized by TEM observations [141,150,152]. Fig. 46 demonstrates interaction processes of dislocations and deformation twins with lamellar interfaces. The loading geometry in the related deformation test was chosen such that shear processes through the lamellar boundaries were initiated. The translation mechanism for shear deformation through the lamellae was found to depend on their interfacial



Fig. 46. Slip/twin interactions at lamellar interfaces. Deformation at 300 K, loading axis parallel to the interfaces ($\phi = 0^\circ$), acceleration voltage 300 kV. (a) $1/2\langle 110 \rangle$ dislocations and $1/6\langle 112 \rangle$ twinning partial dislocations piled up at a semicoherent lamellar interface, foil orientation close to $\langle 101 \rangle$. (b) Translation of twinning deformation across an interfacial boundary γ/γ_T between lamellae with true twin orientation. Foil orientation $\langle 101 \rangle$. (c) Translation of shear deformation across a semicoherent interface γ_1/γ_2 . Foil orientation close to $\langle 101 \rangle$.

structure [141,150,152]. Fig. 46a shows ordinary $1/2\langle 110 \rangle$ dislocations and $1/6\langle 11\bar{2} \rangle$ twinning partial dislocations piled up against a semicoherent interface and indicating their high obstacle strength. Fig. 46b demonstrates the propagation of a deformation twin through an interface between γ lamellae with true twin orientation. By this process, considerable lattice incompatibilities are expected, which surprisingly are confined to a rather narrow region at the interface. At these regions, recrystallization can be initiated at elevated temperatures (cf. Fig. 20a). The mechanism seems to provide some resistance for twin propagation as the twinning partial dislocations were often found to be immobilized at the interface and as dislocations were often generated close to the intersection region. In contrast to the coherent lamellar boundaries, the overcoming of semicoherent interfaces between 60° and 120° rotational variants of γ lamellae involves the generation of perfect and twinning partial dislocations by the mechanisms described in Section 5.2. Fig. 46c demonstrates the transmission of twinning shear deformation through such a semicoherent interface. The twins were mostly immobilized and extended glide processes were initiated in the adjacent lamellae. The glide processes start at the dislocation half-loops present at the semicoherent interfaces (Fig. 21, Figs. 39 and 40). In this way, the high stress concentration in front of the twins was effectively shielded. The dislocation pile ups demonstrated in Fig. 46a give supporting evidence for a hardening mechanism according to the classical Hall–Petch mechanism. However, the accommodation mechanism shown in Fig. 46b and c supports another view of yielding in polycrystalline material, which has been proposed by Li and Chou [205] as an extension of the classical Hall–Petch mechanism. In this model, the internal boundary may act as dislocation source and the efficiency to emit dislocations may primarily depend on the character of the boundary and to a lesser extent on the grain size. In this respect, the complexity of slip geometry and the restrictions on the multiplication of superdislocations, as has been discussed in Section 5.2, are particularly important and may explain why the Hall–Petch constants k_y for lamellar microstructures are relatively high, when compared with conventional alloys. Thus, the physical significance of the parameter k_y is still open to discussion. Recent computer modelling of dislocation pile ups in multilayers [206], which simulate fully-lamellar microstructures, have revealed that the yield stress is most sensitive to the lamellar spacings. The yield behaviour of polycrystalline lamellar TiAl has also been examined by finite element procedures [207]. The study revealed that the constraints exerted by neighbouring crystals are the dominant factor controlling the yield stress. As these constraints can relax when only a small number of grains is sampled in the specimen volume, a serious underestimation of the flow stress may occur.

7.2. Solid solution strengthening

As has been described in Section 2.1, most empirical variations of alloy chemistry have been conducted to improve the ductility of γ alloys. In this section, emphasis will be placed on assessing the potential of solid solution strengthening for increasing the yield stress. In two-phase titanium aluminides, the position of the boundary between the $(\alpha_2 + \gamma)$ and γ phase field depends on the addition of ternary elements (cf. Section 2.1). Thus, small variations of the composition are often associated with significant changes of the microstructure. This may easily mask strength variations caused by solid solution or precipitation hardening. In this respect, the most reliable information on solute effects may be extracted from investigations on PST crystals as these materials always have a fully-lamellar microstructure. Furthermore, shear deformation parallel to the interfaces ($\phi = 45^\circ$) can be achieved without being interfered by the lamellar boundaries. Solid solution hardening due to V, Cr, Mn, Mo, Ta, Nb and Zr has clearly been recognized when adding 0.6–1% of these elements to binary PST crystals [13] (Fig. 8). Among these elements, Zr, Mo, Ta and Nb seem to be most effective for strengthening γ alloys.

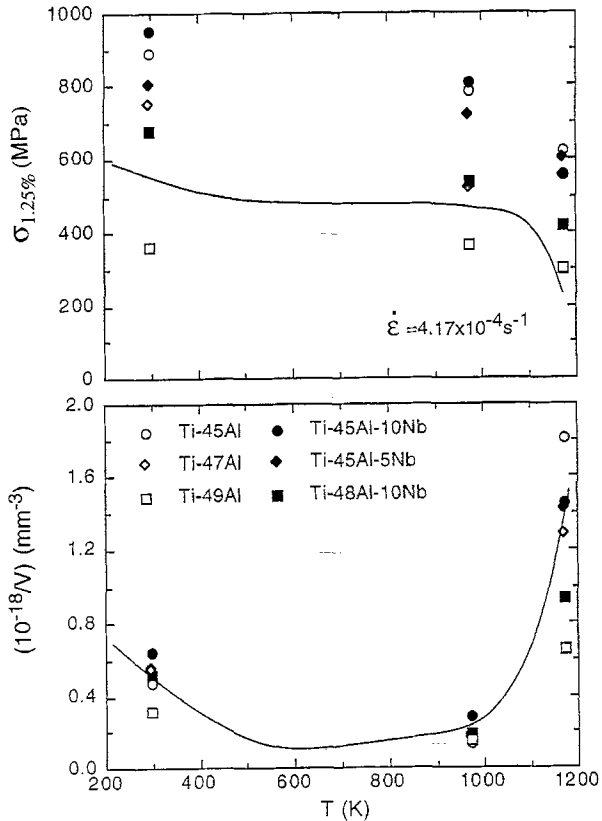


Fig. 47. Dependence of the flow stress σ and of the reciprocal activation volume $1/V$ on the deformation temperature. The data of different binary and ternary alloys containing Nb-additions are shown. For comparison, the data of a Ti-47Al-2Cr-0.2Si alloy (material 1a in Table 2) are indicated by the drawn lines.

Several groups have studied the effects of ternary additions on the yield strength of polycrystalline materials [24,27,208–212]. In a two-phase alloy of the base line composition Ti-48Al, Cr was found to be an effective solute strengthener while Mn was not [28,208–210]. A significant strengthening effect has also been reported for Nb when added with an amount of 10 at.% to two-phase alloys [24,211,212]. The origin of this hardening mechanism has been studied by a systematic variation of the Al and Nb contents and an assessment of the strength properties in terms of activation parameters [164]. Fig. 47 shows the flow stresses and reciprocal activation volumes measured on different ternary alloys containing Nb and the values of binary alloys with the equivalent Al content. For comparison, the data of the Ti-47Al-2Cr-0.2Si alloy (material 1a in Table 2) are given. Accordingly, there is a significant strengthening effect for the binary and ternary alloys containing 45% Al, when compared with the conventional material. The strengthening effect is almost independent of the Nb content. Furthermore, no strengthening is noticeable for Ti-48Al-10Nb. It was therefore concluded that the effect of Nb on the strength properties is much less than the effect of the Al content. This view is supported by the experimental finding that all alloys exhibited almost the same activation volume. The strengthening effect is therefore athermal in nature and probably related to the structural changes associated with the low Al content. This conclusion appears also plausible in the light of ALCHEMI examinations (atom location by channelling enhanced microanalysis of site occupation), which have revealed that Nb favors the Ti sublattice [213,214].

7.3. Precipitation hardening

Recent studies [25,215] have revealed that the solubility of interstitial elements such as oxygen and nitrogen in γ (TiAl) is significantly lower than the impurity contents of most technical materials. Precipitation may therefore easily occur and contribute to the material strength. For example, the maximum solubility of oxygen in the γ matrix of ternary alloys is about 250 at. ppm, whereas the total oxygen content of technical materials often exceeds 1500 at. ppm. It is therefore expected that the oxygen excess leads to the precipitation of oxides, which impede the dislocation motion. A significant increase of the yield stress due to oxygen additions of about 0.1 at.% has been recognized by Kawabata et al. [216] on different binary alloys. Precipitation of fine-scale oxide particles on $1/2\langle 110 \rangle$ dislocations has been reported in Ref. [217].

The strengthening effects of carbide and nitride precipitates have been systematically studied by Tian and Nemoto [29] and Christoph et al. [31]. The precipitates can be formed by solution annealing and subsequent quenching, followed by annealing. TEM examination and diffraction analysis revealed needle-shaped Ti_3AlC and Ti_3AlN precipitates of perovskite type with their long axis parallel to the [001] direction of the matrix [30,218]. For precipitate strengthening to become effective, a fine dispersion of precipitates is required. This can be achieved by suitable ageing conditions [29]. The interaction mechanisms of the dislocations with the precipitates have been studied by mechanical testing and TEM observations [31]. For an assessment of the relative contributions of thermal and athermal mechanisms, the yield stress was described in terms of Eqs. (5.5) and (5.8) and analyzed in terms of activation parameters (cf. Section 5.1).

Fig. 48 shows the dependencies of σ and $1/V$ on the carbon concentration for homogenized and quenched materials where the carbon atoms are thought to be in solid solution or in form of tiny agglomerates. The data were compared with those of homogenized and aged materials which contain

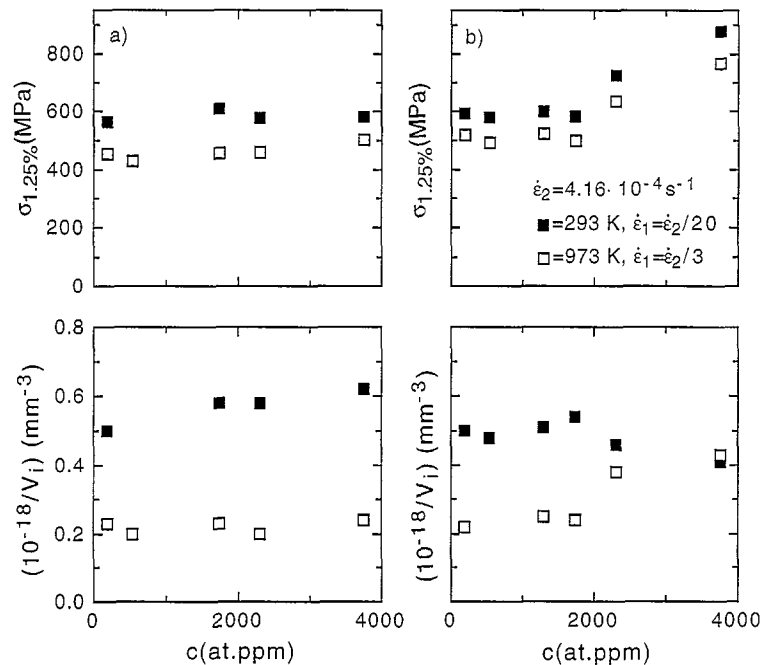


Fig. 48. Dependence of the flow stress σ and the reciprocal activation volume $1/V$ on the carbon concentration. (a) Homogenized and quenched materials with carbon atoms in solid solution or in form of tiny agglomerates. (b) Homogenized and aged materials which contain a fine dispersion of Ti_3AlC perovskite type precipitates.

a fine dispersion of Ti_3AlC perovskite precipitates. For the quenched material, the flow stresses are nearly independent of carbon concentration. In contrast, the flow stress of the carbide containing alloys increases with c . The different deformation behavior is also manifested in the activation volume. Homogenized materials exhibit at room temperature relatively large values of $1/V$, which slightly increase with c . It is therefore concluded that the carbon atoms in solid solution act as weak glide obstacles, which apparently can easily be overcome with the aid of thermal activation. These impurity related defects are therefore manifested in the activation volume but are rather ineffective for hardening the material. In contrast, the reciprocal activation volume of the aged material slightly decreased with c indicating that the density of thermal obstacles decreases with c . It is therefore concluded that the flow stress increase as observed in aged material is mainly athermal in nature, i.e., the related glide obstacles cannot be overcome with the aid of thermal activation. This is supported by the fact that the high flow stresses of the strongly doped materials were maintained up to 973 K.

The high glide resistance of the perovskite precipitates become also evident in TEM observations. The deformation structure observed after 3% compression at room temperature consisted mainly of $1/2\langle 110 \rangle$ ordinary dislocations, $\langle 011 \rangle$ superdislocations and $1/6\langle 11\bar{2} \rangle$ order twins. As demonstrated in Fig. 49a and b, perfect and twinning partial dislocations were pinned by the perovskite precipitates. The obstacle spacing along the dislocations was typically $l_c = 50–100$ nm. The high glide resistance provided by the precipitates is manifested by the strong bowing-out of the dislocation segments. The bowing process is particularly pronounced at the twinning partial dislocations because of their low line tension. The effective shear stresses τ_c acting on the pinned dislocation segments were estimated

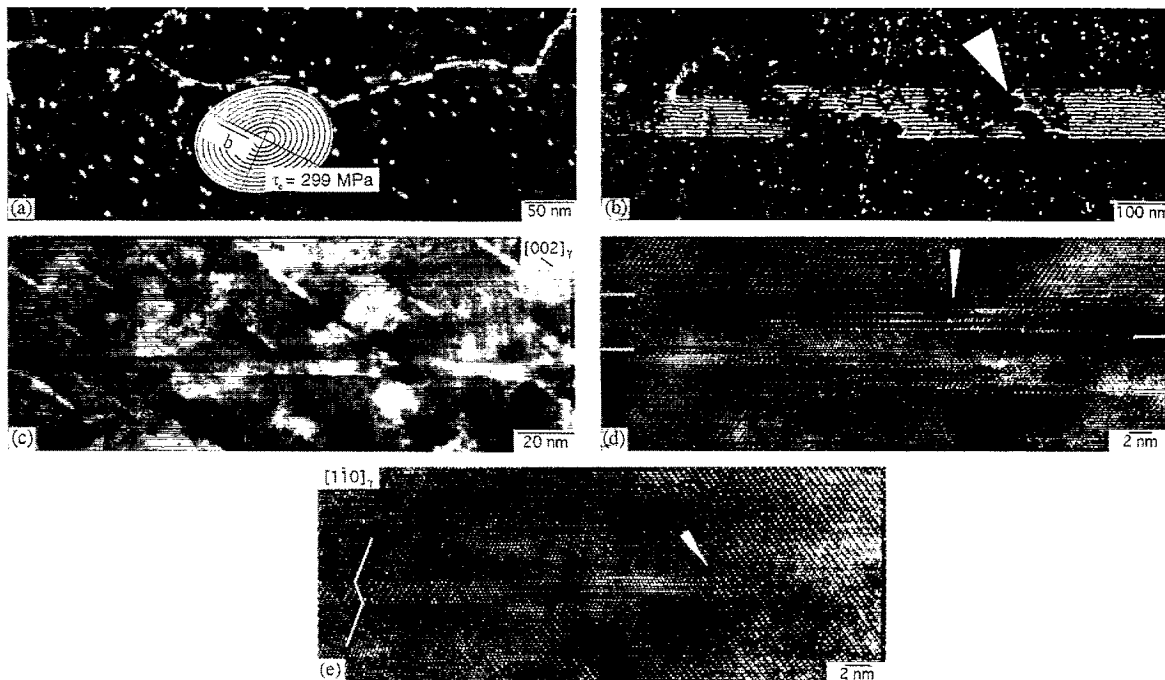


Fig. 49. Deformation structure of an aged Ti–48.5Al–0.37C alloy generated during room temperature compression to strain $\varepsilon = 3\%$. Pseudo-weak beam images recorded using $g = (002)_{TiAl}$ reflection from near the $[020]$ pole in the $g/3.1\text{ g}$ condition, and high resolution images in $\langle 110 \rangle_\gamma$ projection. Note the high density of Ti_3Al -precipitates. (a) Pinning of $\langle 011 \rangle$ superdislocations by the precipitates. The insert shows line tension configurations calculated for different stresses and projected into the image plane. To the segment analyzed, the length $l_c = 110$ nm, the half axis $q = 80$ nm and the effective shear stress $\tau_c = 299$ MPa have been attributed. (b) Pinning of twinning partial dislocations (arrowed) by the precipitates. (c) Low magnification high resolution image showing a deformation twin and perovskite precipitates. (d) Deflection of a deformation twin due to interactions with perovskite precipitates. (e) Immobilization of a deformation twin (arrowed).

by analyzing their curvature. Line tension configurations were calculated for different stresses according to the DeWitt and Koehler model [193], which considers the dependence of the line energy of a dislocation on its orientation. Elastic isotropy was assumed for the sake of simplicity. Within the framework of this model, the loops are apparently elliptical with the major semi-axis q (in μm) parallel to the Burgers vector. Loops of this configuration are related to the shear stress τ_c by

$$\tau_c (\text{MPa}) = \frac{\mu b}{4\pi(1-\nu)} \cdot \frac{1}{q} \ln \left(1.6l_c/b \right). \quad (7.1)$$

Line tension loops were calculated for different stresses and projected into the foil plane (Fig. 49a). By comparison with the observed loop shapes, effective shear stresses $\tau_c = 300 \text{ MPa}$ were obtained. This value can be related to a normal stress $\sigma_c = f\tau_c = 900 \text{ MPa}$, which is consistent with the flow stress $\sigma = 1000 \text{ MPa}$ at strain $\varepsilon = 3\%$. This, together with the high density of pinning centers, leads to the conclusion that a significant portion of the total flow stress in the aged materials arises from the interactions of perfect and twinning partial dislocations with the precipitates. Due to the relatively large size of the precipitates, it is speculated that their overcoming by the dislocations is essentially an athermal process as has been suggested by the concentration dependence of the activation volume (Fig. 48). This view is supported by the frequent observation of sessile dislocation configurations in the form of bundles or multiples. The athermal nature of the glide processes is also manifested in the observed structure of deformation twins. Due to their strong interactions with the precipitates, the twinning partials are frequently immobilized. This often leads to a deflection (Fig. 49c and d) or complete immobilization of the twins (Fig. 49e). As overcoming of the precipitates cannot be supported by thermal activation, the resulting glide resistance will be maintained under low creep rates. The high glide resistance of the perovskite precipitates at elevated temperature deformation is demonstrated in Fig. 50 by the strong bowing of the dislocations between the particles [29]. Hardening of two-phase titanium aluminides by fine dispersions of Ti_3AlC precipitates seems therefore to be a suitable metallurgical technique for improving the high temperature strength and creep resistance of the material. The high efficiency of carbon additions for improving the creep resistance has been

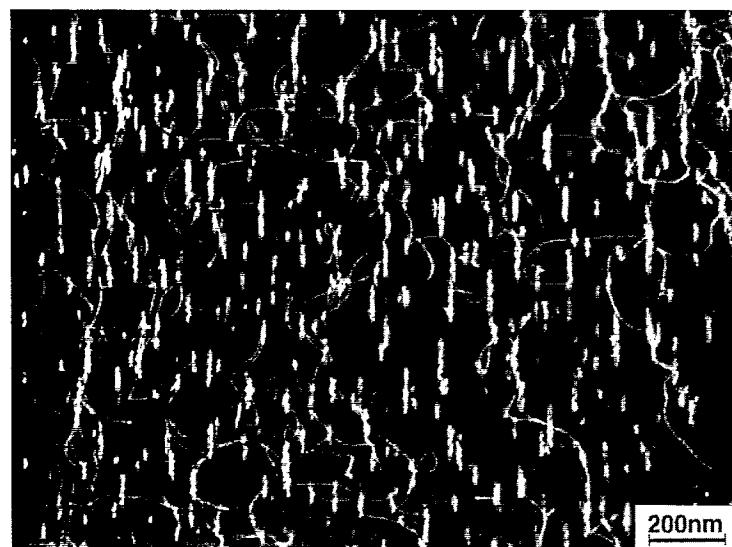


Fig. 50. Dark field electron micrograph showing dislocation interactions with needle-shaped precipitates. $\text{Ti}-51\text{Al}-0.5\text{C}$, annealed at 1523 K for 170 h, followed by quenching and ageing at 1073 K for 100 h. Compression at 873 K to strain $\varepsilon = 3\%$. Note the strong bowing of the dislocations between the precipitates. (Micrograph: Tian and Nemoto [29].

demonstrated on a Ti–48Al–1V alloy containing 0.3 at.% C [219]. However, in contrast to the analyses presented above, the enhanced glide resistance was attributed to a solute atmosphere drag mechanism.

In two-phase alloys, boron additions are often used for refining and stabilizing the grain size in castings [220,221]. Most structural investigations revealed long ribbon-like precipitates with a thickness down to a few nanometers for all levels of boron addition [222–224]. Frequently, the related changes of the mechanical properties have been attributed to the grain refinement achieved. However, as revealed by TEM observations and thermal activation analysis [Müllauer et al., unpublished work] in addition to the coarse precipitates also a fine dispersion of boride particles can be formed which may serve as glide obstacles. The implications of this type of glide obstacles on the work hardening behavior will be addressed in Section 7.4.

Precipitation strengthening due to fine Ti_5Si_3 particles less than 200 nm in size has been reported for a Ti–48Al–1.5Cr alloy containing 0.26–0.65 at.% Si. The hardening mechanism was proofed effectively to enhance the creep resistance [225,226].

7.4. Work hardening

Compared with the large amount of mechanical data, little information on work hardening of $\gamma(TiAl)$ is available. Essentially, this reflects the limited tensile ductility of the material. However, in compression, it is possible to produce work hardening over large plastic strains. For example, at room temperature values of $\sigma/\mu \geq 3 \times 10^{-2}$ can be achieved which apparently presents a significant potential to strengthen the material. Analysis of work hardening in terms of dislocation mechanisms is hindered by the large number of phenomena which might be involved. This includes the classical strain hardening mechanisms which have been considered for conventional alloys as well as processes being related to the particular dislocation core structure and glide geometry of $\gamma(TiAl)$. Rather than attempting a general discussion, we present a few examples which typify the processes and give some insight into the material behavior at high strains. Emphasis will be placed on the effects of temperature, strain rate and precipitation hardening. For an assessment of the relative contribution of thermal and athermal work hardening mechanisms, the flow stress will be described analogous to Eq. (5.8) (cf. Section 5.1) as

$$\sigma(\varepsilon) = \sigma_o + \sigma_\mu(\varepsilon) + \sigma^*(\varepsilon) = \sigma_o + \sigma_\mu(\varepsilon) + 1/V_d(\varepsilon) (\Delta F_d^* + kT \ln \dot{\varepsilon}/\dot{\varepsilon}_o). \quad (7.2)$$

σ_o represents the stress contribution from thermal and athermal mechanisms which are operating at the onset of yielding (cf. Section 5.1). Thus, σ_o is considered to be independent of strain. $V_d(\varepsilon)$ and ΔF_d^* are the activation volume and the free energy of activation, respectively, of deformation induced short-range obstacles. Thus, the variation of the reciprocal activation volume with ε will serve as a measure for the contribution of thermal glide obstacles to work hardening [68,152].

Polycrystalline $\gamma(TiAl)$ alloys often exhibit a parabolic relation between σ and ε , although in some materials extended yield drop phenomena have been observed (cf. Fig. 7). The work hardening coefficients $\vartheta = d\sigma/d\varepsilon$ determined in compression are nearly independent of temperature. At strain $\varepsilon = 6\%$ and $\dot{\varepsilon} = 10^{-4} s^{-1}$, the values are typically $\vartheta/\mu = 0.07$ [68,69,152]. Athermal contributions to work hardening in terms of the stress part $\sigma_\mu(\varepsilon)$ of Eq. (7.2) certainly arise due to elastic interactions of dislocations on parallel slip systems. This becomes evident by multiple structures, which have frequently been observed after room temperature deformation (Fig. 51). The dislocations are probably trapped because of their elastic interaction and local recombination by cross glide. It may therefore be expected that the multiples are relatively strong glide obstacles, which in a wide temperature range contribute to work hardening.

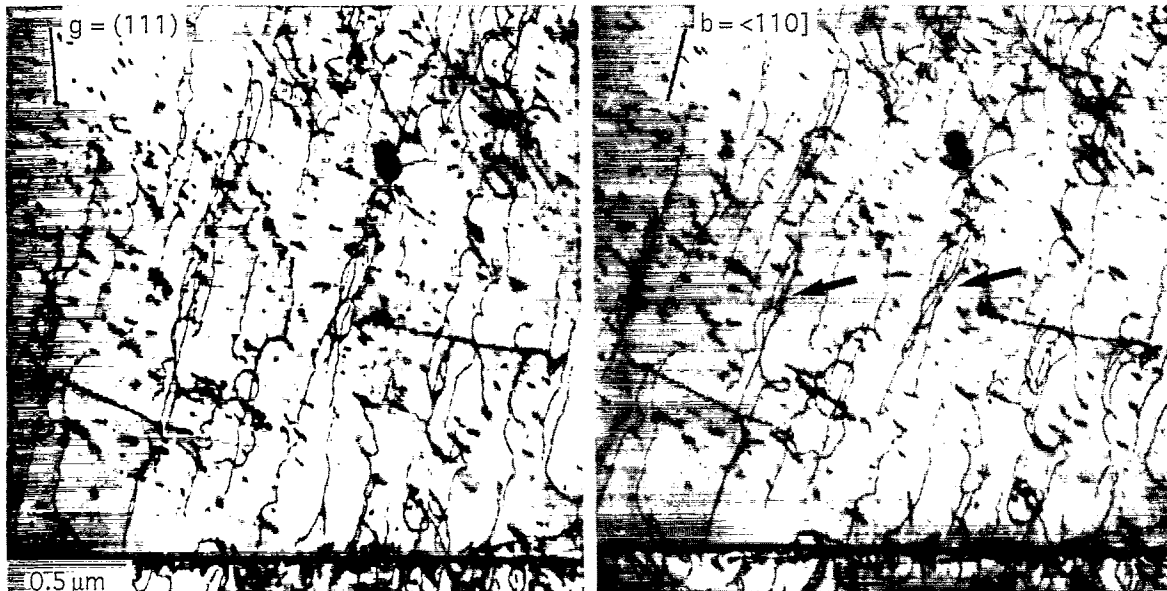


Fig. 51. Stereo pair of micrographs showing multipoles (arrowed) of $1/2\langle 1\bar{1}0 \rangle$ screw dislocations situated on $\{1\bar{1}1\}$. High order bright field images using $g = (111)$, reflection from near the $[011]$ pole. Ti–48Al–2Cr, compression at $T = 300$ K to strain $\varepsilon = 3\%$.

Due to the complex glide geometry of the $L1_0$ structure in most cases several glide systems are subjected to similar stresses. It is therefore expected that multiple slip occurs and obliquely oriented slip systems interpenetrate. Dislocations intersecting on oblique glide systems are impeded by strong elastic interactions and jog formation. Although the details of these mechanisms depend on the mutual orientation and the type of the dislocations involved [178,227,228], a significant contribution to the work hardening is expected as the frequency of the intersections certainly increases with strain [178]. Fig. 52 demonstrates the intersection of two sets of $1/2\langle 110 \rangle$ screw dislocations situated on different $\{111\}$ planes. In the region of intersection numerous dislocation dipoles and debris defects are present. This indicates that jogs are formed by the intersection processes. The generation of dipole defects at jogs in screw dislocations has been described in Section 5.1.

In $\gamma(\text{TiAl})$, Kear–Wilsdorf type locks can be formed by decomposition and dissociation of dislocations (Section 4). Different configurations have been discussed by Greenberg [229], Greenberg and Gornostirev [230], and Greenberg et al. [231]. The locked dislocations are considered to be very effective glide obstacles probably resulting in athermal stress parts; experimental evidence is rare, however.

The processes discussed above provide mainly athermal contributions to the flow stress, thus, their contributions to work hardening are almost independent on temperature and strain rate. However, there is clear evidence that short-range defects may also contribute to work hardening. Deformation at RT is always accompanied by an increase of the reciprocal activation volume [68,152], Fig. 53a. As $1/V$ is related to the obstacle density, it can be inferred from Fig. 53a that new short-range glide obstacles were generated by the straining. It is speculated that the dislocation dipoles and debris defects may act as deformation induced glide obstacles. The generation mechanisms of the dipoles have been discussed in Sections 5.1 and 5.2 and together with Fig. 52. Fig. 54 demonstrates the interaction of a dislocation with a small debris defect [68]. The dislocation is strongly bowed-out at the defect, which indicates its high obstacle strength. There are certainly complex interactions between gliding dislocations and debris defects, which can initiate cross slip. Thus, the strong bowing of the dislocation at

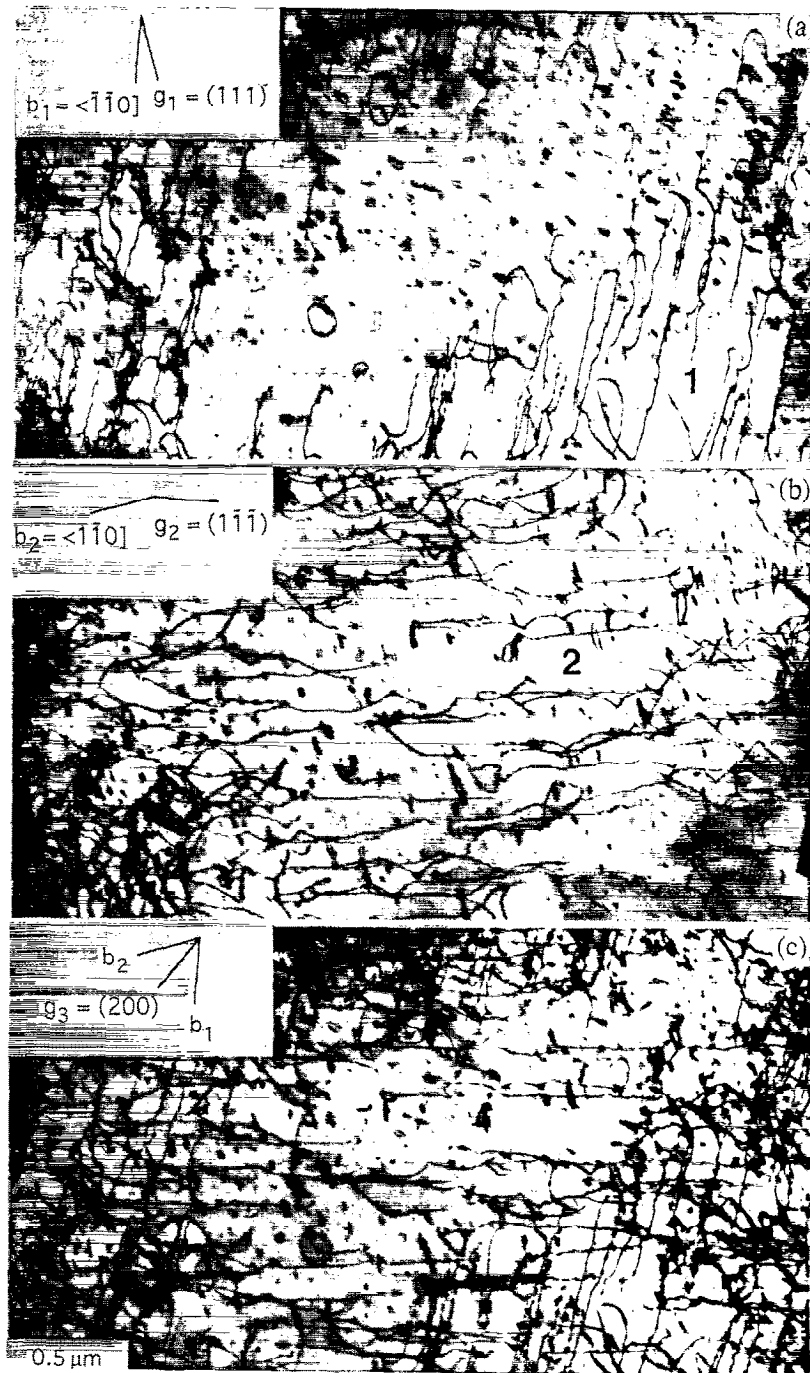


Fig. 52. Intersections of two sets of $1/2\langle 110 \rangle$ dislocations propagating on different $\{111\}$ planes. Ti-48Al-2Cr, compression at $T = 300$ K to strain $\varepsilon = 3\%$. High order bright field images from near the $[0\bar{1}\bar{1}]$ pole using the reflections g_i , indicated. (a) set (1): screw dislocations with Burgers vector $b_1 = 1/2\langle 110 \rangle$ situated on $(\bar{1}\bar{1}\bar{1})$, $g_1 = (111)_\gamma$, (b) set (2): screw dislocations with Burgers vector $b_2 = 1/2\langle \bar{1}\bar{1}0 \rangle$ situated on (111) , $g_2 = (111)$, (c) sets (1) and (2) of screw dislocations are simultaneously imaged using $g_3 = (200)_\gamma$.

the defect may be attributed to the presence of a jog. However, this seems not to be the case as the rounded configuration of the dislocation close to the defect is characteristically different from the jogged configurations shown in Fig. 26. There is certainly a broad distribution of defect sizes. Small

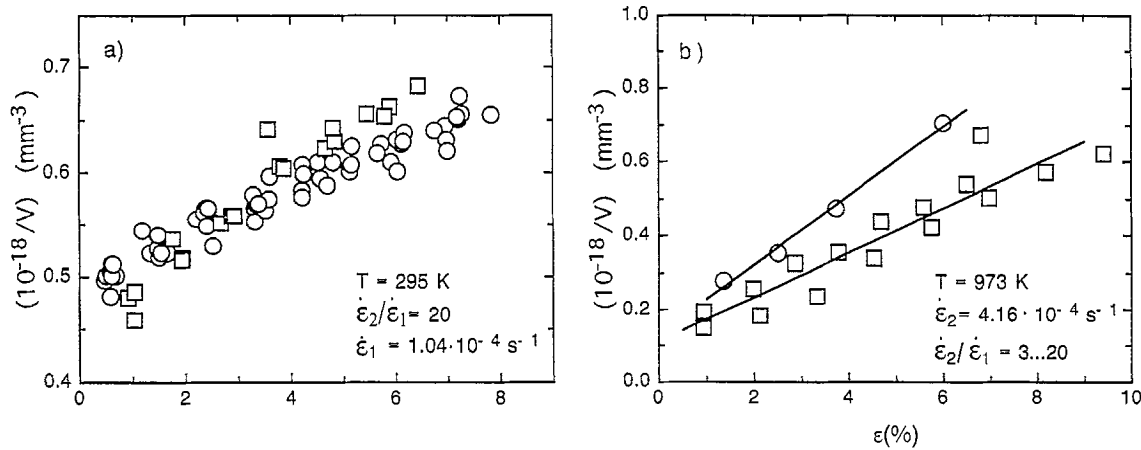


Fig. 53. Dependence of the reciprocal activation volume $1/V$ on strain ε . Ti-47Al-2Cr-0.2Si. ○ near gamma and □ nearly lamellar microstructure; compression at (a) $T=300 \text{ K}$, (b) $T=973 \text{ K}$.



Fig. 54. Interaction of a $1/2\langle 110 \rangle$ screw dislocation with a debris defect (arrowed). Ti-48Al-2Cr, compression at $T=300 \text{ K}$ to strain $\varepsilon=3\%$.

dipole defects are expected to have short-range stress fields [232] so that they probably can be overcome with the aid of thermal activation. Thus, these defects should be manifested in the activation volume. Since the density of the dipole defects increases with strain, the overcoming of small debris defects exhibits the characteristic features of a strain dependent thermally activated deformation mechanism. Thus, work hardening must be accompanied by an increase of $1/V$ with ε as shown in Fig. 53a.

At elevated temperatures, the increase of $1/V$ with ε is much more pronounced (Fig. 53b). Straining to $\varepsilon=8\%$ typically leads to the activation volume $V=60b^3$, when referred to the Burgers vector of ordinary dislocations [68,163]. This is about 30% of the value determined at the beginning of deformation and is close to the theoretical predictions for dislocation climb of $V=1-10b^3$ [233]. It is therefore concluded that the contribution of climb processes strongly increases during high temperature straining and determines work hardening. This view is supported by the strong dependence

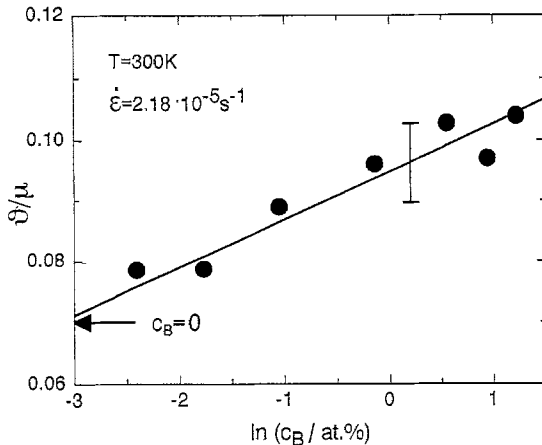


Fig. 55. Dependence of the work hardening coefficient $\vartheta/\mu = (1/\mu)d\sigma/d\varepsilon$ on the boron concentration. Ti-48Al-2Cr+B, compression at $T = 300$ K.

of the work hardening rate on $\dot{\varepsilon}$ [68,152,157] and the high activation energy (Section 5.1, Table 3) observed at elevated temperatures.

Another important aspect of work hardening is related to the effects of dispersed particles. On Ti-50Al and Ti-56Al alloys, a significant increase of the work hardening rate with increasing oxygen concentration has been observed [234]. Although no direct evidence was given, the strengthening effect, in part, was attributed to dislocation interactions with $\alpha\text{-Al}_2\text{O}_3$ particles. This type of work hardening phenomena has also been recognized in boron-doped Ti-48Al-2Cr alloys as shown in Fig. 55. The strengthening effect probably arises from fine boride particles which are impenetrable for the dislocations as shown in Fig. 56. Overcoming may occur via the classical Orowan mechanism [235], which then leaves a dislocation loop around the particle [236]. The loops accumulated at the particles give rise to a back stress which, in turn, leads to an increment of strain hardening [237,238].

From the foregoing discussion of strengthening mechanisms, the following conclusion may be drawn. Like many other engineering materials, titanium aluminides derive their strength from various mechanisms. Grain refinement represents a very effective and economical method of improving the strength. Further investigations are needed to link dislocation based models of microplasticity with continuum mechanical modelling. Another important way to strengthen the material is precipitation hardening. Most important are alloying additions for which optimized dispersions of particles can be formed by a solution annealing followed by ageing. The precipitate microstructure, however, must be stable with respect to coarsening in order to avoid strength degradation under service conditions. For nitrides and carbides, this has yet to be proved. It is interesting to note that work hardening, apart from long-range mechanisms, is also derived from non-conservative dislocation processes, such as jog dragging, debris hardening and dislocation climb. The relative contributions of these mechanisms depend on temperature. At elevated temperatures, dislocation climb is predominant. Thus, work hardening becomes strongly rate dependent under these conditions and is ineffective at low strain rates. Concerning the intended service temperatures of about 700°C, the most effective strengthening of titanium aluminides apparently arises from fine, uniformly distributed particles. From the engineering view-point, the challenge is to establish this mechanism without compromising other desirable properties.

8. Creep properties

While satisfactory room temperature tensile properties of $\gamma\text{(TiAl)}$ alloys can be achieved via alloy optimization and microstructure control, their limited creep strength is still of major concern.



Fig. 56. Dislocation loops left around boride particles due to dislocation interactions according to the Orowan mechanism. Ti-48Al-2Cr-0.87B, compression at $T=300$ K to strain $\varepsilon=10\%$.

For instance, a γ (TiAl) blade being envisaged for usage in the last stage of an industrial gas turbine, typically will be exposed to a stress of ~ 150 MPa at 700°C . Under these conditions, the creep strain must not exceed 1% after service for $\sim 10^4$ h. This demands a strain rate $\dot{\varepsilon}$ as small as 10^{-10} s^{-1} which is hardly met by any of the current alloys regardless of their microstructure. For most creep experiments conducted hitherto, the temperature and stresses were chosen such that $\dot{\varepsilon}$ exceeded 10^{-10} s^{-1} by several orders of magnitude. Thus, the results obtained from such studies must not necessarily be relevant for envisaged engineering applications.

8.1. Phenomenological observations of creep curves

Phenomenologically, like for conventional materials, the creep curves $\varepsilon(t)$ of γ (TiAl) display several distinct creep regimes (Fig. 57). The onset and extension of each regime depends on temperature and stress as well as on the microstructure (Section 8.2). Primary (or transient) creep occurs upon initial loading and is characterized by a period of decreasing creep rate. As exemplified in Fig. 57a, even for lower stresses, the transient creep strain can be rather high and, thus, may approach the design limit for the tolerable maximum creep strain of a component. Thus, minimization of the primary creep strain is an important requirement for engineering applications. During secondary creep, $\dot{\varepsilon}$ attains a steady state value or, as frequently observed in two-phase alloys, reaches a minimum value ($\dot{\varepsilon}_{\min}$) before it increases again slowly with strain (Fig. 58).

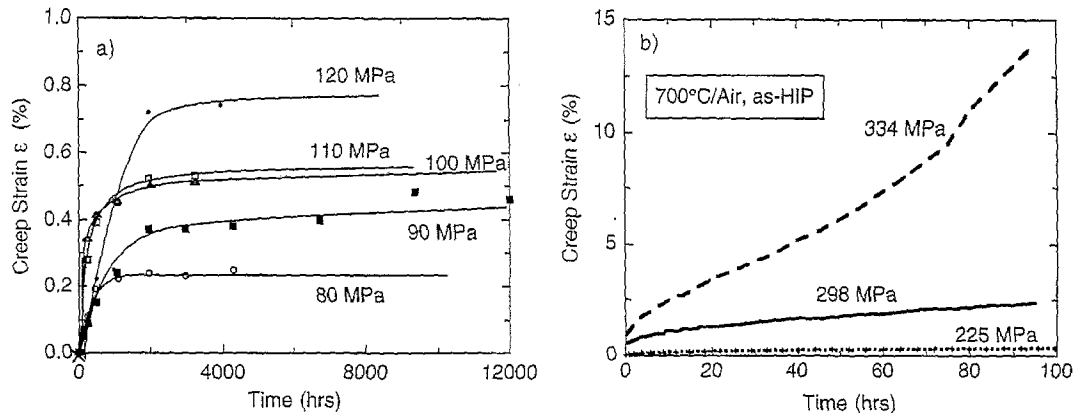


Fig. 57. Creep curves measured at 700°C in air under (a) low and medium, and (b) high tensile stresses. Ti–48Al–2Cr in the as-HIP condition with ~80 vol % lamellar colonies and ~20 vol % γ grains [14].

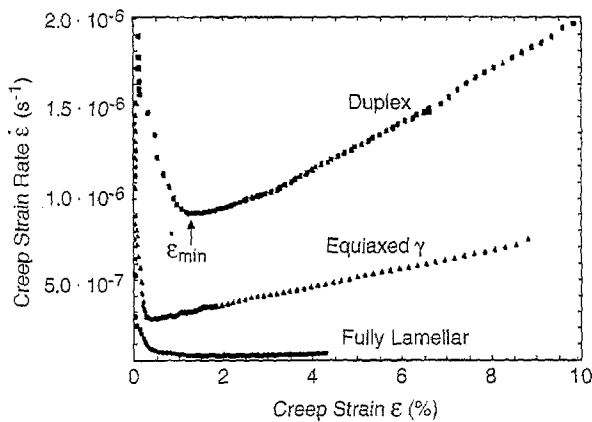


Fig. 58. Creep strain rate as a function of strain for different microstructures. Tested in air at 815°C with $\sigma = 150$ MPa. Data from Ref. [239].

For a quantitative analysis of the creep curves in terms of a power law behavior $\dot{\varepsilon} \sim \sigma^n$ (cf. Section 8.4), usually $\dot{\varepsilon}_{min}$ has been used. At high stresses (Fig. 57b), secondary creep is followed by the onset of tertiary creep. To the authors' knowledge, little is known about the influence of test environment on the creep behaviour, in particular, during long term creep at small rates.

8.2. Effect of microstructure on creep

Despite the large body of papers dealing with creep properties [85,239–248], a detailed understanding of the influence of various microstructural parameters such as grain or colony size, volume fraction and morphology of the γ and α_2 —and sometimes β phase on the creep strength is still lacking [12].

Creep testing at 700°C revealed a pronounced influence of the microstructure on creep strength (Fig. 59) as has also been reported from previous studies for temperatures up to 870°C [85,219,239–248]. Consistently, the creep strength of the fully-lamellar microstructure has been found to be superior when compared with equiaxed and duplex ones. Furthermore, for identical conditions, the secondary creep regime is more extended for fully-lamellar than for equiaxed γ or duplex microstructures (Fig. 58).

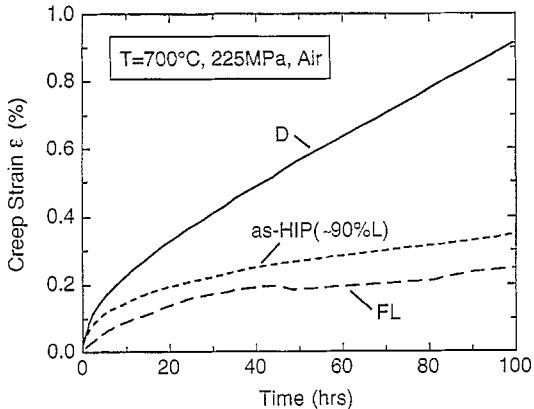


Fig. 59. Influence of microstructure on creep curves of Ti-48Al-2Cr.

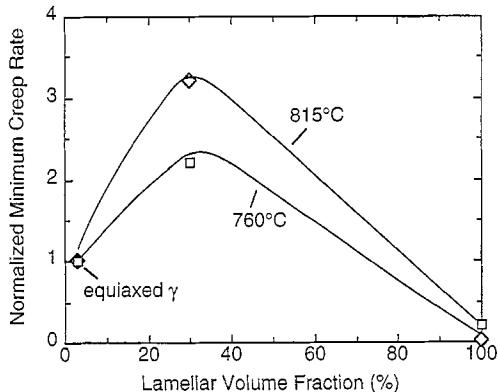


Fig. 60. Influence of the lamellar volume fraction on minimum strain rate of Ti-49Al-1V. Testing at 760 and 815°C in air at $\sigma = 100$ MPa. The creep rates were normalized with respect to those of the equiaxed microstructure at either temperature. Data from Ref. [239].

A systematic study of the influence of the lamellar volume fraction on creep properties revealed that $\dot{\epsilon}_{\min}$ does not monotonically decrease with the volume fraction of lamellar grains but rather displays a maximum at about ~30 vol % of the lamellar constituent [241,245] in a duplex microstructure (Fig. 60). Thus, the rule-of-mixture [249,250] which has frequently been used for analyzing the influence of the volume fraction of a second phase on creep resistance does not apply to γ (TiAl) alloys with duplex microstructures. A microscopic explanation for this experimental finding, however, is still lacking. Similarly, the puzzling fact that the creep resistance of equiaxed γ microstructures is superior to that of the duplex ones (cf. Fig. 58) is far from being understood on a microscopic level, in particular, as the deformation structures in the lamellar colonies of duplex microstructures have been found to be essentially identical to those in fully-lamellar materials [219,242,243]. This suggests the creep behaviour of the γ grains to be rather different depending on whether they are constituent of the equiaxed or the duplex microstructure. It may be speculated that the dislocation mobility is significantly reduced in the γ grains of the equiaxed γ microstructure due to the higher friction forces resulting from the presence of interstitial impurities. In contrast, as outlined in Section 3.1, the level of interstitial impurities dissolved in γ grains of the duplex microstructure is much smaller because of the considerably higher volume fraction of the α_2 phase (cf. Section 7.3). This is further corroborated by the observation that a rather high density of precipitates was formed in duplex Ti-48Al-2Cr (Fig. 61) which had been creep deformed at 700°C for 6000 h at a moderate stress (140 MPa) into the



Fig. 61. Dislocation interactions with precipitates after long-term creep (700°C , 140 MPa, 6000 h, $\dot{\varepsilon} = 0.69\%$, inert gas). (a) Pinning of dislocation segments at the departure side of precipitates. High order bright field image using a systematic row of $g = \{111\}_{\gamma}$ reflections. (b) Interaction of a gliding dislocation with an immobilized ordinary dislocation decorated by precipitates. Note the dislocation reaction indicated by the arrow. Pseudo-weak beam image recorded using $g = \{111\}_{\gamma}$ reflections from near the $\langle 10\bar{1} \rangle$ pole in the $g/3.1\ g$ condition. (c) Decoration of a subgrain boundary and of isolated dislocations by precipitates [251].

transition regime from secondary to tertiary creep. Concomitantly with the long-term creep deformation, the α_2 laths were found to dissolve. This mechanism which has been reported to occur also during creep at 800°C [242] or upon long-term ageing of RFL material at 800°C [252] is suggested to lead to a growing supersaturation of interstitial impurities with increasing creep strain. As evidenced by the decoration of creep induced subgrain boundaries and isolated dislocations, the nucleation of the precipitates is heterogeneous in nature. It is certainly supported by the low dislocation velocity under the creep conditions applied ($\dot{\varepsilon} \sim 3 \cdot 10^{-10} \text{ s}^{-1}$). Even though the nature of the precipitates could not yet be identified they are speculated to contain oxygen or nitrogen. Gliding dislocations show a strong interaction with the creep induced precipitates (Fig. 61a). The decorated and immobilized dislocations may also act as strong obstacles for subsequent gliding dislocations. Local reactions among these lead to the formation of stable configurations (Fig. 61b).

8.3. Microscopic creep mechanisms

From a microscopic point of view, there is still much uncertainty on whether creep at small rates which are typical for engineering applications ($\dot{\varepsilon} \sim 10^{-10} \text{ s}^{-1}$), is a glide or a climb controlled process. At high stresses, the creep rates are rather high and close to strain rates typically used in dynamic tensile experiments ($\dot{\varepsilon} \sim 10^{-5} \text{ s}^{-1}$). Consequently, the deformation microstructure is expected to be similar to that found in material tested under constant strain rate conditions, with glide and twinning being the dominant mechanisms. This, in fact, has been confirmed for crept duplex material where mechanical $1/6\langle 11\bar{2}\rangle \{111\}$ twinning and glide of ordinary $1/2\langle 110\rangle$ dislocations are the most important deformation mechanisms [242,253]. However, unlike in dynamic tensile testing, in crept fully-lamellar microstructures dislocation glide and climb prevails, and deformation twinning is rarely to be observed [240,243]. This difference in microstructural evolution at similar deformation rates requires further elucidation.

After long-term tension creep at moderate stresses and small rates ($\dot{\varepsilon} \sim 10^{-9} \text{ s}^{-1}$), lamellar colonies contain essentially ordinary dislocations, some superdislocations and dislocation networks (Fig. 62). Again deformation twins have rarely been observed. Under the given creep conditions, dislocation loops which at room temperature were anchored at the lamellar boundaries (cf. Section 6.2) can detach and thus contribute to creep deformation (Fig. 62a). This happens at relatively low stresses ($\sigma \ll \sigma_y$) indicating the dislocation friction forces to be strongly reduced due to stress assisted thermal activation. This mechanism has been evidenced by the multiple generation of dislocation loops from lamellar interfaces (Fig. 62b, Fig. 63). The interface-related deformation mechanism explains the high primary creep rate (Figs. 58 and 59) of lamellar materials when compared with coarse grained single phase alloys [254]. However, as the misfit character of the interfaces is changed by dislocation emission, the mechanism becomes exhausted after some straining and thus will be effective only in the primary creep regime.

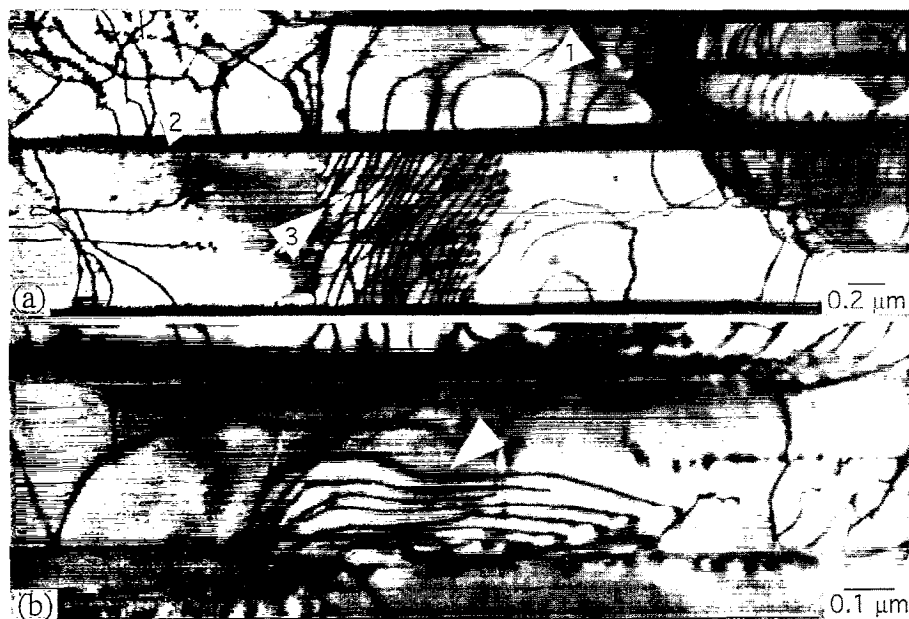


Fig. 62. Dislocation structure after long-term creep $\sigma = 140 \text{ MPa}$, 700°C , $t = 6000 \text{ h}$, $\varepsilon = 0.69\%$. (a) Note the emission of interface dislocation loops (1), decorated dislocations (2), and dislocation networks (3). (b) Multiple generation of $1/2\langle 110\rangle$ dislocations [251].

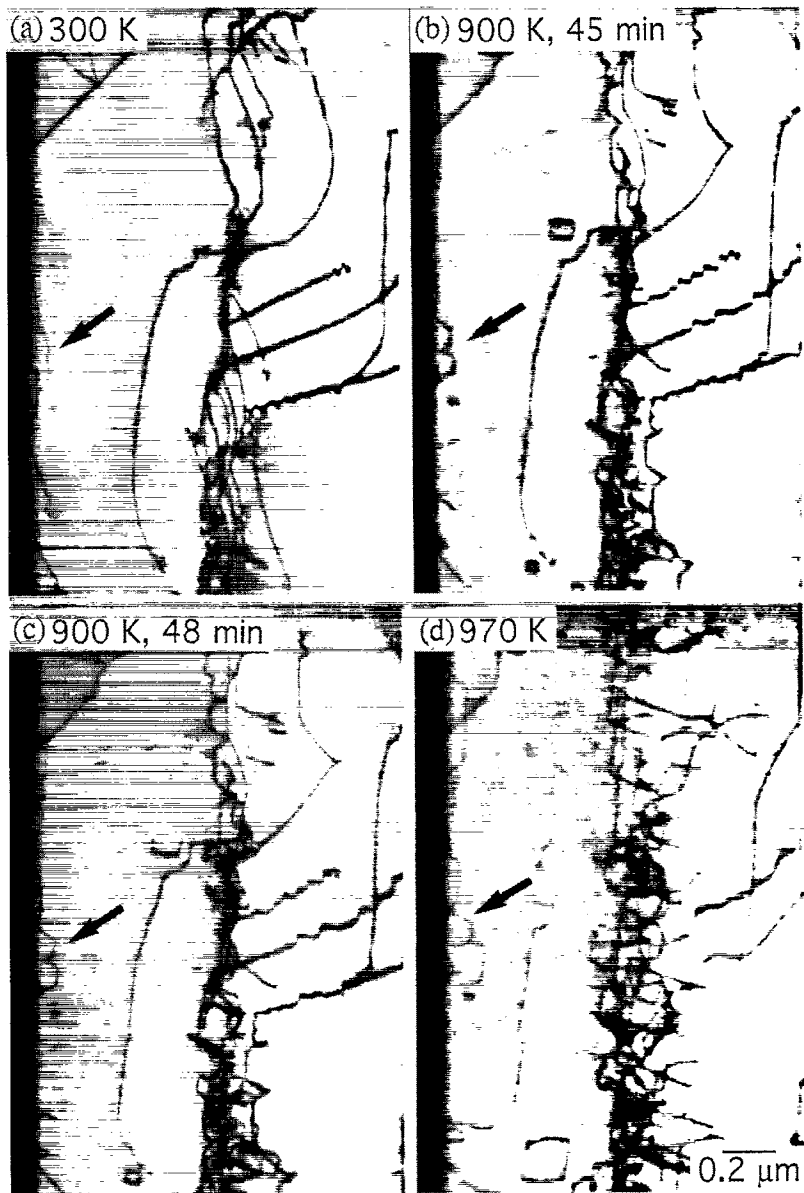


Fig. 63. Climb of interfacial dislocations during in situ heating inside the TEM. Note the emission of dislocations from the lamellar interfaces (arrowed). The formation of helical configurations of the dislocations may operate as Bardeen and Herring dislocation climb sources. Nearly-lamellar Ti–48Al–2Cr; colony size $\sim 1000 \mu\text{m}$; lamellar spacing ranging from 0.05 to $1 \mu\text{m}$ [163].

The propagation of dislocations occurs under diffusional control as indicated by their climb configurations (Fig. 62a). This is further corroborated by in situ heating to 630 and 700°C in the TEM. Fig. 63a–d demonstrate the change of the mismatch structures under the given conditions. The misfit dislocations assume helical configurations, which are characteristic of climb. These processes lead to interconnected loop structures, which may act as Frank–Read glide sources or Bardeen and Herring climb sources (cf. Section 5.2, Fig. 29). The efficiency and relative contribution of the two multiplication mechanisms to creep deformation certainly depends on the particular creep conditions.

The thermal activation analyses described in Section 5.1 have revealed that in the temperature regime III (Fig. 25) which is relevant for creep deformation, the activation enthalpy is close to the

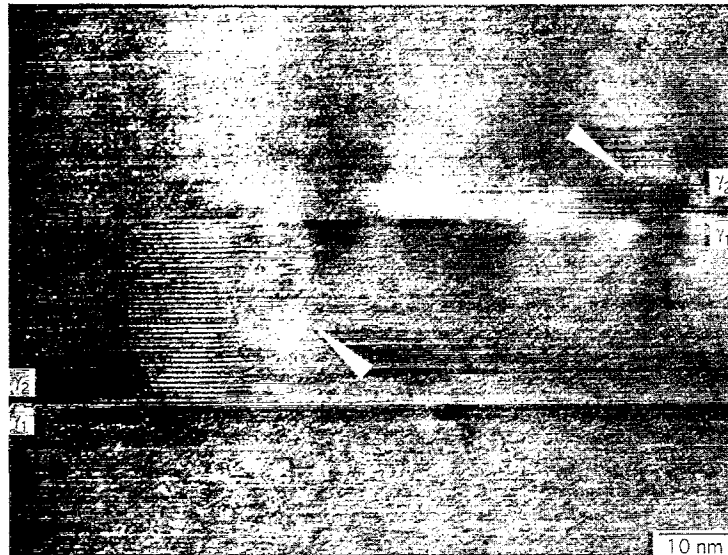


Fig. 64. Formation of two ledges at a lamellar twin boundary upon long-term creep of Ti-48Al-2Cr ($\sigma = 140 \text{ MPa}$; $T = 700^\circ\text{C}$; $t = 6000 \text{ h}$; $\varepsilon = 0.69\%$). At the ledges, slabs of the 9R structure are imaged.

self-diffusion enthalpy ($Q_{sd} = 3.01 \text{ eV}$ [174]) of $\gamma(\text{TiAl})$. This points towards lattice diffusion to control deformation. The activation volume, however, is considerably larger ($V = 47b^3$) than just $1-10 \cdot b^3$ as expected for climb controlled deformation [233,255]. On grounds of TEM studies, Kad and Frazer [157] have assumed that dislocation motion occurs via climb as well as glide depending on stress. Appel et al. [163] took a different view, corroborated by TEM studies (Fig. 29). They concluded that some dislocation segments are dissociated on intersecting $\{111\}$ planes with resulting non-planar core configurations. This leads to a locking of the dislocation segment involved. Its average climb velocity thus may critically depend on the particular segment length which, in turn, is associated with a considerably larger activation volume.

In addition to the above mentioned dislocation mechanisms, migration of the lamellar interfaces also contributes to creep. As exemplified in Fig. 64, two ledges of different height were formed in an originally flat twin boundary (cf. Section 6.1) upon long-term creep. Through formation and growth of such ledges, the interface can migrate, thus, shearing the material by twinning. Ledges with heights up to 200 nm were frequently observed in the lamellar colonies. At all ledges, slabs of the 9R structure become discernible (Fig. 64). The 9R structure has also been observed in a two-phase alloy heavily deformed at room temperature [158] and after high-temperature deformation [141]. This structure forms from the L1_0 structure by twinning operations on two adjacent $\{111\}$ planes and an anti-twinning operation on every third $\{111\}$ plane [158]. It is speculated that the ledges arise from Shockley partial dislocations which moved along the interfaces and were piled up at misfit dislocations [256]. This is supported by the observation that in all cases misfit dislocations occur at the ledges. Once a sharp pile up has been formed the configuration may rearrange under diffusional control into a tilt configuration with long-range elastic stress fields. This would cause further Shockley partials to be incorporated into the ledge.

8.4. Power law behaviour and microstructural stability of creep

The occurrence of a steady-state creep rate ($\dot{\varepsilon}_{ss}$) is considered to result from a balance between the rates of work hardening and recovery [257]. If such balance is established, the dependence of $\dot{\varepsilon}_{ss}$

on stress (σ) and temperature (T) is usually expressed in terms of the general constitutive power law [258,259].

$$\dot{\varepsilon}_{ss} = A_o \cdot \sigma^n \cdot e^{-Q/kT}. \quad (8.1)$$

The dislocation configuration and density which are assumed to be constant are included in the pre-exponential factor A_o , together with other structural parameters such as stacking fault energy, dispersion of second phases, grain size, etc. all supposed to be constant. Regardless of the particular microstructure, a steady state creep rate has barely become discernible when $\dot{\varepsilon}$ versus ε had been plotted. Thus, in general, instead of $\dot{\varepsilon}_{ss}$, the minimum creep rate $\dot{\varepsilon}_{min}$ has been used for a determination of the stress exponent n and the activation energy Q of creep by means of Eq. (8.1).

Compilations of n and Q values [12,242,244] which have been derived in numerous creep studies on the basis of Eq. (8.1), revealed large discrepancies in such data. The n values range from $n \approx 2$ to $n \approx 8$ without any noticeable correlation with microstructure though with some reported tendency for n to increase with increasing stress [260,261]. Whether this is indicative for a transition from diffusional creep ($n \approx 1$) to dislocation climb controlled creep ($n = 4.5$) at higher stresses as discussed in Refs. [242,244,262], or rather a breakdown of power law behavior due to the prevalence of dislocation glide controlled creep at high σ [260], is still subject to controversy.

Activation energies for creep of two-phase alloys have been reported to range from 230 to 430 kJ/mol with the upper bound showing some tendency of being associated with the higher stress exponents [12,242]. These data must be compared with the activation energy $Q_{sd} = 290$ kJ/mol for self-diffusion of Ti in single-phase γ (TiAl) [174]. Thus, at medium stresses where n and Q are in the range of ~ 4 and ~ 300 kJ/mol, respectively, dislocation climb may be assumed as the creep controlling mechanism.

However, for several reasons, the significance of the n and Q data and the related interpretation of the creep controlling mechanisms will remain questionable as long as the applicability of Eq. (8.1) is not justified by complementary analyses of the evolution of the substructure with creep strain: (i) The restrictive condition of the constancy of A_o is rarely satisfied as severe microstructural changes such as precipitation of interstitial impurities and changes of the interfacial boundary structure during creep at small rates were observed (cf. Section 8.3). Furthermore, both dynamic recrystallization of equiaxed γ grains which originally surrounded lamellar colonies, and the spheroidization of the α_2 -laths cause microstructural instabilities in crept duplex material [242,251]. The γ lamellae adjacent to the dynamically recrystallized γ grains show some buckling and experience also dynamic recrystallization at larger creep strains. In these regions, the lamellar structure is no longer preserved [242]. Similar microstructural instabilities have been reported for Ti–47Al with a nearly-lamellar microstructure upon ageing without applied load for 168 h at 800°C. γ grains along lamellar colony boundaries were found to grow whereas some lamellae within the colonies dissolved [252]. (ii) For single-phase γ (TiAl) a back stress reducing the applied stress was concluded to exist [263]. Dislocation pile ups such as observed at the lamellar boundaries (e.g., Fig. 46) are likely to build up a back stress in the lamellar constituent of two-phase γ (TiAl) the neglection of which may lead to an apparent stress exponent which is considerably higher [244]. (iii) Most creep tests were conducted under constant tensile load without accounting for the increase in stress as creep strain increases.

In essence, analyses of creep data in terms of power law creep did not provide conclusive information on the creep controlling mechanisms. More detailed analyses of the microstructural stability and the evolution of substructure with creep strain, are needed in order to elucidate the effect of stress and temperature on the creep behavior. The experiments should be conducted under conditions which are relevant for the envisaged engineering applications.

9. Crack tip plasticity

The experimental findings on tensile ductilities and fracture toughness described in Section 3.3 have demonstrated that the microstructure of two-phase titanium aluminides significantly affects the fracture mechanisms. Thus, the observed variation of fracture toughness has often been attributed to mechanisms which are closely related to the lamellar morphology. This involves shear ligament bridging, crack deflection and microcrack shielding [54,76,77,80,86]. These analyses are based upon continuum fracture mechanics where the effects of local crystallography and anisotropy of crack tip plasticity are not taken into account. However, there is supporting evidence that crack tip plasticity can also lead to an appreciable enhancement in fracture resistance of two-phase materials [83,92,250]. As these aspects of crack propagation are closely related to the mechanisms of dislocation dynamics addressed in Sections 5.1 and 5.2, we shall concentrate on TEM observations of crack tip plasticity. The cracks investigated in those studies [92] propagated accidentally in thin wedge-shaped foils so that the sample geometry and the loading conditions were unknown. Nevertheless, the method gives direct information on the defect structure ahead of crack tips which cannot be obtained by other techniques. Thus, the results may contribute to achieve a microscopic understanding of crack processes in TiAl.

The effects of the microstructure on the crack propagation became also evident in the TEM observations. The characteristic differences become obvious when studying crack processes in duplex microstructures where both microstructural constituents, i.e., γ grains and lamellar ($\alpha_2 + \gamma$) grains, are present. The typical features are shown in Fig. 65. In the γ grains, cleavage-like fracture on $\{111\}$ planes down to the atomic level occurs indicating their relatively low cohesive strength, which has been predicted by Yoo and Fu [264] on ground of their first principles total energy calculations. The cracks are frequently arrested at the boundary of adjacent lamellar colonies. In front of the crack tip, a plastic zone was formed. It is extended over several lamellae and consists mainly of $1/6\langle 11\bar{2} \rangle \{111\}$ deformation twins and ordinary $1/2\langle 110 \rangle$ dislocations. Thus, the shape of the plastic zone is strongly determined by the crystallography of these slip elements. For comparison, in Fig. 65, the shape of the plastic zone is drawn, which is expected at a mode-I crack tip in an elastically isotropic solid under plane stress conditions [83,92,265]. The comparison may demonstrate the high strain localization in the experimentally observed zone as a result of the particular crystallography of the shear processes initiated by the crack.

Within the lamellar morphology, crack propagation across the lamellae is characterized by various interactions of the crack tip with the lamellar interfaces (Fig. 66). Within the individual lamellae, the crack follows $\{111\}_\gamma$ planes again indicating cleavage-like fracture. At the lamellar interfaces, crack deflection occurs according to the change of the orientation of the $\{111\}_\gamma$ cleavage planes of the adjacent lamellae with a common $\langle 110 \rangle$ direction. Thus, a more tortuous zigzag-shaped crack path is formed. Finally, the crack was arrested at a semicoherent interface γ_1/γ_2 between γ variants with a matrix/matrix relationship (detail 1).

In addition to these microstructural aspects, fracture resistance seems also to be derived from crack tip plasticity. The observed processes are closely related to the factors governing the dislocation mobility and multiplication which have been discussed in Sections 5.1 and 5.2. Structural details of the crack tip plasticity are shown in Fig. 67, which represents enlarged details of the framed region (3) in Fig. 66. Ahead of the crack tip, two deformation twins (arrow 2 in Fig. 66) were generated and immobilized at the next semicoherent interface γ_1/γ_2 of γ variants with a pseudo-twin relationship. The stress concentration in front of the twins is relaxed by the formation of dislocations with the Burgers vector $b = 1/2\langle 110 \rangle$, (Fig. 67a). These dislocations were probably emitted from the interfacial dislocation network by the stress field ahead of the immobilized twins as described in Sections 4.3 and



Fig. 65. A crack in a Ti-48Al-2Cr alloy with a duplex microstructure. The imaged region shows a γ grain containing a few coarse annealing twins adjacent to a colony of fine ($\alpha_2 + \gamma$) lamellae. GB indicates the grain boundary. The crack propagated in the γ grain on a {111} plane and is arrested at the interface γ/γ_T formed by one of the annealing twin lamellae. Ahead of the crack tip, a plastic zone is formed consisting mainly of deformation twins (T), which propagate across the annealing twins. The main twin T_1 is finally immobilized in the lamellar colony (arrow). For comparison, the shape of the plastic zone expected from the elastic stress field at a mode-I crack tip is drawn. Foil orientation close to $\langle 011 \rangle_\gamma$.

6.2. As in bulk material, within the plastic zone the dislocation mobility seems to be determined by localized pinning and jogs. The dislocations are strongly bowed out between the pinning centers indicating their high obstacle strength. As estimated from the dislocation curvature shear stresses of about 250 MPa act in front of the crack tip. Thus, according to Eq. (5.10), very narrow dislocation dipoles of height $h > 15b$ may operate as dislocation sources (Section 5.2). A few of the dipoles indicated by arrows in Fig. 67b are probably in the initial state of multiplication, which is indicated by the fact that the edge arms have already by-passed. Thus, considering the observed high density of jogs in screw dislocations, there is probably a sufficient number of sources available for the multiplication of ordinary dislocations.

As has been discussed in Section 4.3, in principle, a sufficient number of independent slip systems is available in $\gamma(\text{TiAl})$. However, the van Mises criterion is not the only necessary condition for an arbitrary shape change of a polycrystalline material. Not only must the five systems be operative at comparable stresses, but they should also be homogeneously activated throughout each grain. Having recognized the importance of crack tip plasticity in $\gamma(\text{TiAl})$, several aspects of the dislocation kinematics and dynamics can be important in this respect. Dislocation generation and glide band broadening seem to be relatively easy as has been discussed in Section 5. However, dislocations and deformation twins propagating on different slip systems must intersect, a mechanism which seems to be difficult

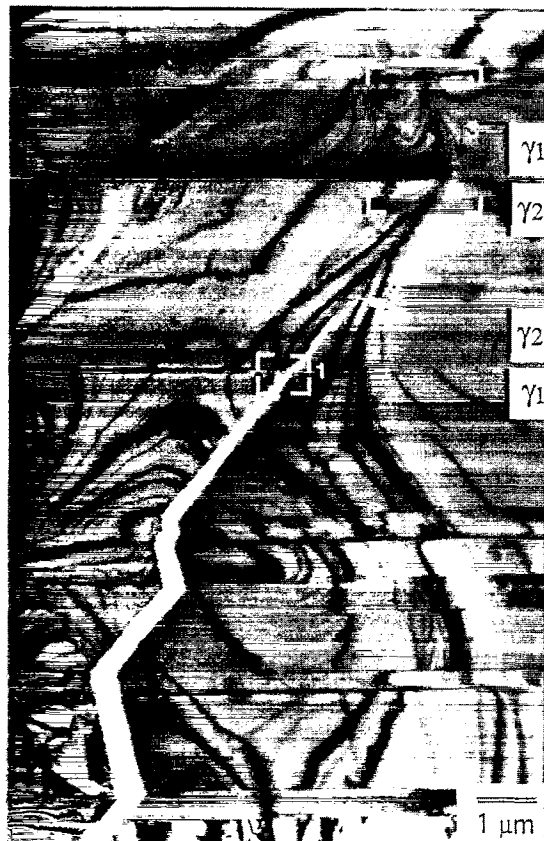


Fig. 66. Crack propagation across lamellar interfaces in a Ti-48Al-2Cr alloy. The crack is arrested at interface γ_1/γ_2 (frame 1). Ahead of the crack tip, two twins are generated, which are immobilized at interface γ_2/γ_1 (arrow 2). The stress concentration in front of the twins is shielded by glide processes of dislocation loops in lamella γ_1 (frame 3). Foil orientation close to $\langle 101 \rangle$.

in $\gamma(\text{TiAl})$ and probably contributes to the high work hardening rate of the material (Section 7.4). Another problem may arise from the anisotropy of the dislocation mobility concerning screw and edge characters, resulting in a predominance of screw dislocations. Debate remains as to whether these particular features are detrimental to the ductility of γ -titanium aluminides.

In summary of this section, the following conclusions can be drawn. On a microscopic scale crack propagation in two-phase titanium aluminides is strongly determined by their susceptibility for cleavage fracture on $\{111\}_\gamma$ planes and the crystallography of glide processes in the $L1_0$ structure. Concerning these aspects, resistance against unstable crack propagation may be derived from crack deflection and dislocation glide processes ahead of the crack tip. This suggestion is supported by the high density of dislocation sources observed in front of crack tips, due to multiple cross glide and dislocation emission from interfaces. It is speculated that crack tip plasticity is particularly important for crack propagation in equiaxed γ materials, where the toughening mechanism operative in the lamellar constituents are almost absent. This speculation is supported by different temperature dependence of the fracture toughness observed for equiaxed gamma and nearly-lamellar materials (Fig. 15).

10. Open problems

The intention of the present paper was to describe the mechanical behavior of γ -based two-phase titanium aluminides in terms of micromechanisms of deformation and to investigate how these proc-

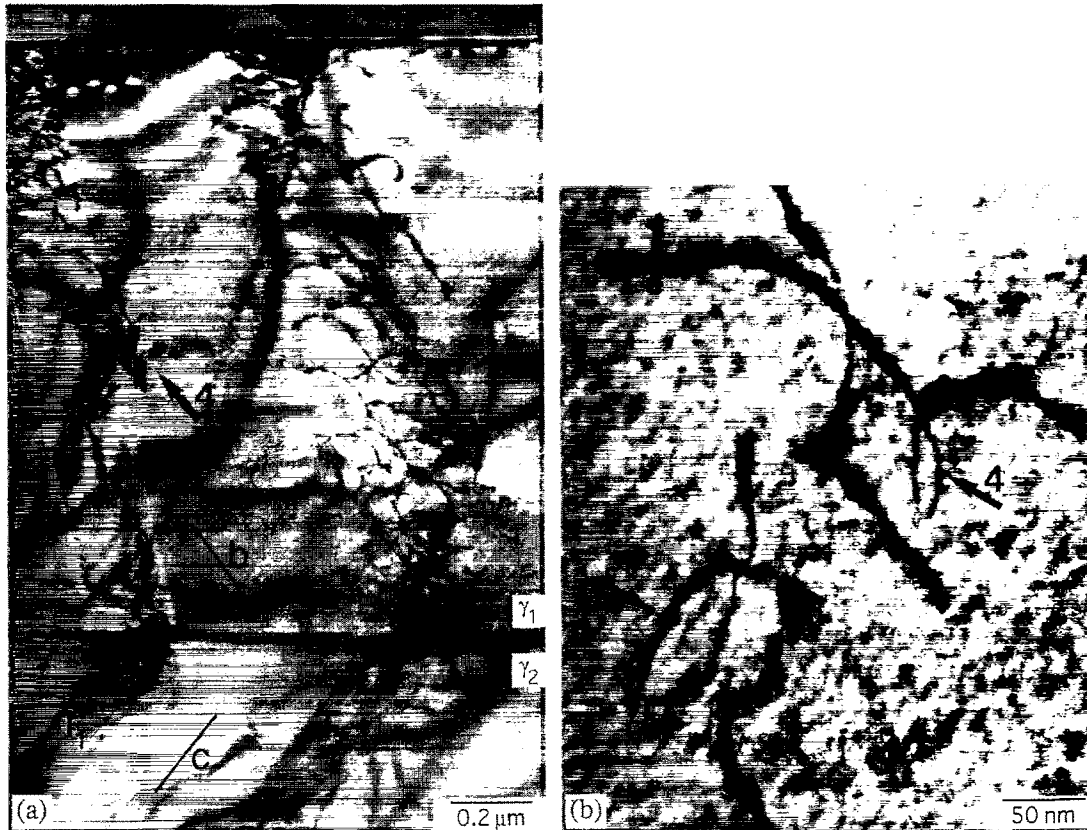


Fig. 67. Crack tip plasticity in front of the arrested crack shown in Fig. 66; enlargements of details. (a) Frame (3): Groups of ordinary dislocations with Burgers vector $b = 1/2\langle 110 \rangle$ ahead of the two deformation twins T_1 and T_2 immobilized at the interface γ_1/γ_2 . The line indicated by C is parallel to the direction of the crack. (b) Higher magnification of detail (4) in Fig. 66: Initial state of dislocation multiplication via cross glide.

esses may be related to appropriate engineering design parameters. As this analysis bases on highly idealized models of dislocation dynamics, it has its own limitations and drawbacks. Furthermore, deformation of complex materials such as titanium aluminides involve many phenomena which impede a rigorous analysis. Thus, several open problems remain which will be addressed in this section.

There are various uncertainties regarding the slip geometry in $\gamma(\text{TiAl})$. This concerns the relative contributions of slip and twinning and their change with deformation temperature. Very limited quantitative information is available on the critical shear stresses needed to activate the different types of perfect and twinning partial dislocations. Thus, in terms of the van Mises criterion, debate remains, whether a sufficient number of independent slip systems can operate at comparable stresses.

The observation that the Hall-Petch equations obeyed for a wide range of polycrystalline material gives strong experimental evidence that grain boundaries and lamellar interfaces impede the propagation of slip. However, the problem of linking flow stresses with structural parameters in different microstructures is still under discussion.

Strain accommodation is certainly an important issue of deformation and fracture of polycrystalline TiAl. Several mechanisms have been reported including slip/twin interactions and various interface related processes. Nevertheless, more work including TEM-observations is required.

The collected data support the view that the dislocation velocity is controlled by various processes involving lattice friction, impurity interactions, jog dragging, and climb. Attempts to assess quantitatively the relative contributions are frustrated for several reasons. There is rather limited information

on the temperature dependence of the individual mechanisms and the rules of their superposition. Unfortunately, in most cases, the particular parameters which can be controlled in a certain experiment, represent only a fraction of those influencing the flow stress. Thus, it is difficult to design experiments which separate the contributions of the individual micromechanisms.

Little information is available on the effects of ternary elements like Cr and Mn on the lattice parameters and dislocation mobilities, although these elements are known to enhance the material ductility. No systematic studies have been performed on the influence of oxygen and nitrogen, which in technical alloys are unavoidable impurities.

While the multiplication of ordinary dislocations and the nucleation of twins is well documented, little information is available on the generation of superdislocations being a characteristic feature of the slip geometry of the $L1_0$ structure.

Rather less is available which deals with the work hardening behaviour of the material. This concerns the evolution of the defect structure during straining and the origin of the unusually high work hardening rate when compared with conventional materials.

Although there are many investigations on the creep properties, their assessment in terms of dislocation dynamics and the evolution of the substructure is still unsatisfactory. In particular, this holds true for long-term creep under relatively low stresses, even though such conditions are relevant for the intended engineering applications.

Precipitation hardening has been found to be very effective for strengthening the material. Quantitative assessments and direct observations of the hardening mechanism are rare, however. This is due to the fact that the analysis requires a careful determination of particle sizes and separation distances, which is difficult to realize by conventional TEM diffraction contrast imaging. Furthermore, additions of doping elements often lead to changes of the microstructure which additionally may affect the flow stress. For optimized strength properties, it is necessary to specify both, the obstacle strength and the dispersion of the particles. Thus, precipitation hardening is likely to play an important role for both, fundamental research and as the basis for developing more creep resistant γ alloys.

Some relevant topics of current interest have had to be excluded. They involve textures, recovery, recrystallization, and fatigue.

11. Outlook

Alloy chemistry and processing technologies of two-phase γ alloys have been developed to such an extent that semifinished products and structural parts can be fabricated with a promising balance of engineering properties. Testing some of these parts under service conditions has rendered γ (TiAl) as a weight-saving structural material for replacing Ni based superalloys. At the present state of the art, its maximum operational temperature capability must be seen at about 700°C.

When comparing γ (TiAl) with competing high-temperature structural materials, major R&D efforts must be directed towards improving its strength level while maintaining sufficient ductility, toughness and damage tolerance. At the same time, the creep resistance and rupture strength, which are closely related to structural stability must be improved for long-term service, e.g., in industrial gas turbine applications. Promising approaches in achieving these objectives may be seen in (i) alloying additions which lead to further microstructural refinement with an associated Hall-Petch type strengthening, (ii) a reduction in the Al content with a related increase of the α_2 phase, and (iii) via precipitation strengthening.

The rather poor impact toughness and insufficient fatigue crack growth resistance of present generation γ (TiAl) alloys is related to the low dislocation mobility. As this appears to be an inherent

feature of γ alloys, it can neither be improved via alloy chemistry nor via microstructural control but rather has to be considered in the design of the specific structural part.

Acknowledgements

We gratefully acknowledge many stimulating discussions with our colleagues U. Lorenz, U. Sparka, Drs. U. Christoph, B. Dogan, J. Müllauer, M. Oehring, and J. Paul, and their numerous contributions of experimental data. Mrs. E. Schröder and Mrs. E. Tretau have been very patient with us when preparing and typing the manuscript. We also would like to thank the Deutsche Forschungsgemeinschaft for the given financial support (Ap 49/1-5) and (Ap 49/3-1) within the frame of the DFG-Schwerpunktprogramm ‘Deformation and Fracture of Ordered Materials’.

References

- [1] M.V. Nathal, S.R. Levine, in: S.D. Antolovich, R.W. Stusrud, R.A. MacKay, D.L. Anton, T. Khan, R.D. Kissinger, D.L. Klarstrom (Eds.), *Superalloys 1992*, TMS, Warrendale, PA, 1992, p. 329.
- [2] W. Smarsly, L. Singheiser, in: D. Contouradis, et al. (Eds.), *Materials for Advanced Power Engineering*, Part II, Kluwer Acad. Publish., Dordrecht, 1994, p. 1731.
- [3] D.M. Dimiduk, D.B. Miracle, Y.-W. Kim, M.G. Mendiratta, *ISIJ Int.* 31 (1991) 1223.
- [4] T. Khan, S. Naka, P. Veyssiére, P. Costa, in: E. Bachelet, R. Brunetand, et al. (Eds.), *High-Temperature Materials for Power Engineering*, Kluwer Acad. Publ., Dordrecht, 1990, p. 1533.
- [5] D.M. Dimiduk, in: Y.-W. Kim, R. Wagner, M. Yamaguchi (Eds.), *Gamma Titanium Aluminides*, TMS, Warrendale, PA, 1995, p. 3.
- [6] J.C. Chesnutt, in: S.D. Antolovich, R.W. Stusrud, R.A. MacKay, D.L. Anton, T. Khan, R.D. Kissinger, D.L. Klarstrom (Eds.), *Superalloys 1992*, TMS, Warrendale, PA, 1992, p. 381.
- [7] W. Smarsly, in: Proc. 1993 European Propulsion Forum, Royal Aeronautical Soc., Bath UK, 1993, p. 22.1.
- [8] J.C. Chesnutt, J.C. Williams, *Metals and Materials*, 1990, 509.
- [9] M. Atsuo, *ISIJ Int.* 31 (1991) 1212.
- [10] Y.-W. Kim, *JOM* 41 (1989) 24.
- [11] Y.-W. Kim, D.M. Dimiduk, *JOM* 43 (1991) 40.
- [12] Y.-W. Kim, *JOM* 46 (1994) 30.
- [13] M. Yamaguchi, H. Inui, in: R. Darolia, J.J. Lewandowski, C.T. Liu, P.L. Martin, D.B. Miracle, M.V. Nathal (Eds.), *Structural Intermetallics*, TMS, Warrendale, PA, 1993, p. 127.
- [14] R. Wagner, F. Appel, B. Dogan, P.J. Ennis, U. Lorenz, J. Müllauer, H.P. Nicolai, W. Quadakkers, L. Singheiser, W. Smarsly, W. Vaidya, K. Wurzwallner, in: Y.-W. Kim, R. Wagner, M. Yamaguchi (Eds.), *Gamma Titanium Aluminides*, TMS, Warrendale PA, 1995, p. 387.
- [15] C. McCullough, J.J. Valencia, C.G. Levi, R. Mehrabian, *Acta Metall.* 37 (1989) 1321.
- [16] H.A. Lipsitt, D. Shechtman, R. Schafrik, *Metall. Trans. A* 6A (1975) 1991.
- [17] M.J. Blackburn, M.P. Smith, U.S. patent 4294615, 1981.
- [18] C. Koeppe, A. Bartels, J. Seeger, H. Mecking, *Metall. Trans. 24A* (1993) 1795.
- [19] S.-C. Huang, D.S. Shih, in: Y.-W. Kim, R.R. Boyer (Eds.), *Titanium Aluminides and Alloys*, TMS, Warrendale, PA, 1990, p. 105.
- [20] M. Yamaguchi, Y. Umakoshi, *Prog. Mater. Sci.* 34 (1990) 1.
- [21] C.M. Austin, T.J. Kelly, in: R. Darolia, J.J. Lewandowski, C.T. Liu, P.L. Martin, D.B. Miracle, M.V. Nathal (Eds.), *Structural Intermetallics*, TMS, Warrendale, PA, 1993, p. 143.
- [22] T. Tsujimoto, K. Hashimoto, in: C.T. Liu, A.I. Taub, N.S. Stoloff, C.C. Koch (Eds.), *High-Temperature Ordered Intermetallic Alloys III*, Mat. Res. Soc. Symp. Proc. Vol. 33, Pittsburgh, PA, 1989, p. 391.
- [23] Y.-W. Kim, *Acta Metall. Mater.* 40 (1992) 1121.
- [24] S.-C. Huang, in: R. Darolia, J.J. Lewandowski, C.T. Liu, P.L. Martin, D.B. Miracle, M.V. Nathal (Eds.), *Structural Intermetallics*, TMS, Warrendale, PA, 1993, p. 299.
- [25] A. Menand, A. Huguet, A. Nérac-Partaix, *Acta Mater.* 44 (1996) 4729.
- [26] S.C. Huang, E.L. Hall, *Metall. Trans. A* 22A (1991) 2619.
- [27] S.C. Huang, E.L. Hall, *Acta Metall. Mater.* 6 (1991) 1053.
- [28] T. Kawabata, T. Tamura, O. Izumi, *Metall. Trans. A* 24A (1993) 141.

- [29] W.H. Tian, M. Nemoto, in: Y.-W. Kim, R. Wagner, M. Yamaguchi (Eds.), Gamma Titanium Aluminides, TMS, Warrendale, PA, 1995, p. 689.
- [30] S. Chen, P.A. Beaven, R. Wagner, *Scripta Metall. Mater.* 26 (1992) 1205.
- [31] U. Christoph, F. Appel, R. Wagner, in: C.C. Koch, N.S. Stoloff, C.T. Liu, A. Wanner (Eds.), High-Temperature Ordered Intermetallic Alloys VII, Mat. Res. Soc. Symp. Proc., Vol. 460, Pittsburgh, PA, 1997, p. 207.
- [32] P.A. Beaven, Th. Pfullmann, J. Rogalla, R. Wagner, in: L.A. Johnson, D.P. Pope, J.O. Stiegler (Eds.), High-Temperature Ordered Intermetallic Alloys IV, Mat. Res. Soc. Symp. Proc., Vol. 213, Pittsburgh, PA, 1991, p. 151.
- [33] S.L. Semiatin, N. Frey, C.R. Thompson, J.D. Bryant, *Scripta Mater.* 24 (1990) 1403.
- [34] K. Wurzwallner, H. Clemens, P. Schretter, A. Bartels, C. Koeppe, in: I. Baker, R. Darolia, J.D. Whittenberger, M.H. Yoo (Eds.), High-Temperature Ordered Intermetallic Alloys V, Mat. Res. Soc. Symp. Proc., Vol. 288, Pittsburgh, PA, 1993, p. 867.
- [35] H. Clemens, P. Schretter, K. Wurzwallner, A. Bartels, C. Koeppe, in: R. Darolia, J.J. Lewandowski, C.T. Liu, P.L. Martin, D.B. Miracle, M.V. Nathal (Eds.), Structural Intermetallics, TMS, Warrendale, PA, 1993, p. 205.
- [36] P.E. Jones, W.J. Porter, M.M. Keller, D. Eylon, in: F.H. Froes, W. Wallace, et al. (Eds.), Advances in Synthesis and Processes, Proc. 3rd Intl. SAMPE Metals and Metals Processing Conf., Covina, CA, 1991, M146.
- [37] D. Larsen, C. Govern, in: Y.-W. Kim, R. Wagner, M. Yamaguchi (Eds.), Gamma Titanium Aluminides, TMS, Warrendale, PA, 1995, p. 405.
- [38] S.L. Kampe, J.D. Bryant, L. Christodoulou, *Metall. Trans. A* 22 (1991) 2009.
- [39] J.D. Bryant, S.L. Kampe, P. Sadler, L. Christodoulou, *Metall. Trans. A* 22 (1991) 447.
- [40] G.E. Fuchs, in: I. Baker, R. Darolia, J.D. Whittenberger, M.H. Yoo (Eds.), High-Temperature Ordered Intermetallic Alloys V, Mat. Res. Soc. Symp. Proc., Vol. 288, Pittsburgh, PA, 1993, p. 847.
- [41] R. Wagner, F. Appel, R. Börmann, R. Gerling, in: M. Yamaguchi, H. Fukutomi (Eds.), Proc. 3rd Intl. SAMPE Symp., Chiba, 1993, p. 1548.
- [42] B. London, D.E. Larsen, D.A. Wheeler, P.R. Aimone, in: R. Darolia, J.J. Lewandowski, C.T. Liu, P.L. Martin, D.B. Miracle, M.V. Nathal, Structural Intermetallics, TMS, Warrendale, PA, 1993, p. 151.
- [43] H. Fukutomi, Chr. Hartig, H. Mecking, *Z. Metallkd.* 81 (1990) 272.
- [44] Y.-W. Kim, *Mat. Sci. Eng.* A192/193 (1995) 519.
- [45] K. Müller, X. Neubert, P.A. Beaven, M. Rommerskirchen, in: M. Yamaguchi, H. Fukutomi (Eds.), Proc. 3rd Intl. SAMPE, Chiba, 1993, p. 1564.
- [46] Chr. Hartig, X.F. Fang, H. Mecking, M. Dahms, *Acta Metall. Mater.* 40 (1992) 1883.
- [47] L.A. Willey, H. Margolin, *Metals Handbook*, Am. Soc. Metals, Metal Park, OH, 8th edn., Vol. 8, 1973, p. 264.
- [48] Y.-W. Kim, in: Y.-W. Kim, R.R. Boyer (Eds.), Microstructure/Property Relationships in Titanium Aluminides and Alloys, TMS, Warrendale, PA, 1991, p. 91.
- [49] P.A. Beaven, F. Appel, B. Dogan, R. Wagner, in: C.T. Liu, R.W. Cahn, G. Sauthoff (Eds.), Ordered Intermetallics—Physical Metallurgy and Mechanical Behavior, Kluwer Academic Publishers, Dordrecht, 1992, p. 413.
- [50] S.L.M. Sastry, H.A. Lipsitt, *Metall. Trans. A* 8A (1977) 299.
- [51] H. Inui, M.H. Oh, A. Nakamura, M. Yamaguchi, *Phil. Mag. A* 66 (1992) 539.
- [52] C.R. Feng, D.J. Michel, C.R. Crowe, *Scripta Metall.* 22 (1988) 1481.
- [53] C.R. Feng, D.J. Michel, C.R. Crowe, *Scripta Metall.* 23 (1989) 1135.
- [54] Y.-W. Kim, in: Y.-W. Kim, R. Wagner, M. Yamaguchi (Eds.), Gamma Titanium Aluminides, TMS, Warrendale, PA, 1995, p. 637.
- [55] C.T. Liu, P.J. Maziasz, D.R. Clemens, J.H. Schneibel, V.K. Sikka, T.G. Nieh, J. Wright, L.R. Walker, in: Y.-W. Kim, R. Wagner, M. Yamaguchi (Eds.), Gamma Titanium Aluminides, TMS, Warrendale, PA, 1995, p. 679.
- [56] Y. Umakoshi, T. Nakano, T. Yamane, *Mater. Sci. Eng.* A152 (1992) 81.
- [57] Y. Umakoshi, T. Nakano, *Acta Metall. Mater.* 41 (1993) 1155.
- [58] T. Fujiwara, A. Nakamura, M. Hosomi, S.R. Nishitani, Y. Shirai, M. Yamaguchi, *Phil. Mag. A* 61 (1990) 591.
- [59] H. Inui, A. Nakamura, M.H. Oh, M. Yamaguchi, *Phil. Mag. A* 66 (1992) 557.
- [60] H. Inui, M.H. Oh, A. Nakamura, M. Yamaguchi, *Acta Metall. Mater.* 40 (1992) 3095.
- [61] V.K. Vasudevan, S.A. Court, P. Kurath, H.L. Fraser, *Scripta Metall.* 23 (1989) 467.
- [62] Y.-W. Kim, in: M. Yamaguchi, H. Fukutomi (Eds.), Proc. 3rd Intl. SAMPE Symp., Chiba, 1993, p. 1310.
- [63] Y.-W. Kim, D.M. Dimiduk, to appear in Proc. 2nd Intl. Symp. Structural Intermetallics, Seven Springs, TMS, 1997.
- [64] M. Yamaguchi, H. Inui, K. Kishida, M. Matsumuro, Y. Shirai, in: J. Horton, I. Baker, S. Hanada, R.D. Noebe, D.S. Schwartz (Eds.), High-Temperature Ordered Intermetallic Alloys VI, Mat. Res. Soc. Symp. Proc., Pittsburgh, PA, Vol. 364, 1995, p. 3.
- [65] R. Uemori, T. Hanamura, H. Morikawa, *Scripta Metall. Mater.* 26 (1992) 969.
- [66] J. Kumpfert, Y.-W. Kim, D.M. Dimiduk, *Mater. Sci. Eng.* A192/193 (1995) 465.
- [67] H. Clemens, W. Glatz, F. Appel, *Scripta Mater.* 35 (1996) 429.
- [68] F. Appel, U. Sparka, R. Wagner, in: J. Horton, I. Baker, S. Hanada, R.D. Noebe, D.S. Schwartz (Eds.), High-Temperature Ordered Intermetallic Alloys VI, Mat. Res. Soc. Symp. Proc., Pittsburgh, PA, Vol. 364, 1995, p. 623.
- [69] A. Bartels, C. Koeppe, T. Zhang, H. Mecking, in: Y.-W. Kim, R. Wagner, M. Yamaguchi (Eds.), Gamma Titanium Aluminides, TMS, Warrendale, PA, 1995, p. 655.

- [70] F. Appel, H. Clemens, R. Wagner, in: W.O. Soboyejo, T.S. Srivatsan, H.L. Fraser (Eds.), Deformation and Fracture of Ordered Intermetallic Materials III, TMS, Warrendale, PA, 1996, p. 123.
- [71] B. Viguier, M. Cieslar, J. Bonneville, K.J. Hemker, J.L. Martin, in: Y.-W. Kim, R. Wagner, M. Yamaguchi (Eds.), Gamma Titanium Aluminides, TMS, Warrendale, PA, 1995, p. 275.
- [72] S.H. Wang, Z.M. Wang, Z.X. Li, in: Y.-W. Kim, R. Wagner, M. Yamaguchi (Eds.), Gamma Titanium Aluminides, TMS, Warrendale, PA, 1995, p. 245.
- [73] G. Sauthoff, *Intermetallics*, VCH Publishers, Weinheim, 1995.
- [74] J.H. Westbrook, in: J.H. Westbrook, R.L. Fleischer (Eds.), *Intermetallic Compounds—Principles and Practice*, Vol. 1, Wiley, West Sussex, UK, 1994, p. 3.
- [75] M.A. Morris, *Phil. Mag. A* 69 (1994) 129.
- [76] K.S. Chan, Y.-W. Kim, *Met. Trans. A* 23A (1992) 1663.
- [77] K.S. Chan, Y.-W. Kim, *Met. Trans. A* 24A (1993) 113.
- [78] B. Dogan, D. Schöneich, K.-H. Schwalbe, R. Wagner, *Intermetallics* 4 (1996) 61.
- [79] K.S. Chan, D.L. Davidson, in: R. Darolia, J.J. Lewandowski, C.T. Liu, P.L. Martin, D.B. Miracle, M.V. Nathal (Eds.), *Structural Intermetallics*, TMS, Warrendale, PA, 1993, p. 223.
- [80] K.S. Chan, in: Y.-W. Kim, R. Wagner, M. Yamaguchi (Eds.), *Gamma Titanium Aluminides*, TMS, Warrendale, PA, 1995, p. 835.
- [81] Z.J. Pu, K.H. Wu, J. Shi, D. Zou, *Mat. Sci. Eng. A* 192/193 (1995) 347.
- [82] N.J. Rogers, P. Bowen, in: R. Darolia, J.J. Lewandowski, C.T. Liu, P.L. Martin, D.B. Miracle, M.V. Nathal (Eds.), *Structural Intermetallics*, TMS, Warrendale, PA, 1993, p. 231.
- [83] F. Appel, U. Lorenz, T. Zhang, R. Wagner, in: J. Horton, I. Baker, S. Hanada, R.D. Noebe, D.S. Schwartz (Eds.), *High-Temperature Ordered Intermetallic Alloys VI*, Mat. Res. Soc. Symp. Proc., Vol. 364, Pittsburgh, PA, 1995, p. 493.
- [84] Y.-W. Kim, D.M. Dimiduk, Proc. JIMIS-7 on High-Temperature Deformation and Fracture, Japan Institute for Metals, Sendai, 1993, p. 373.
- [85] D.S. Shih, S.-C. Huang, G.K. Scarr, H. Jang, J.C. Chestnutt, in: Y.-W. Kim, R.R. Boyer (Eds.), *Titanium Aluminides and Alloys*, TMS, Warrendale, PA, 1991, p. 135.
- [86] P. Bowen, N.J. Rogers, A.W. James, in: Y.-W. Kim, R. Wagner, M. Yamaguchi (Eds.), *Gamma Titanium Aluminides*, TMS, Warrendale, PA, 1995, p. 849.
- [87] U. Lorenz, F. Appel, R. Wagner, Proc. Intl. Conf. Strength of Metals and Alloys, ICSMA 11, *Mat. Sci. Eng. A*, 1997, in press.
- [88] P.M. Hazzledine, B.K. Kad, *Mat. Sci. Eng. A* 192/193 (1995) 340.
- [89] S. Yokoshima, M. Yamaguchi, in: M. Yamaguchi, H. Fukutomi (Eds.), Proc. 3rd Intl. SAMPE Symp., Chiba, 1993, p. 1346.
- [90] T. Nakano, T. Kawanaka, H.Y. Yasuda, Y. Umakoshi, in: M. Yamaguchi, H. Fukutomi (Eds.), Proc. 3rd Intl. SAMPE Symp., Chiba, 1993, p. 1334.
- [91] S. Mitao, S. Tsuyama, K. Minakawa, *Mat. Sci. Eng. A* 148 (1991) 51.
- [92] F. Appel, U. Christoph, R. Wagner, *Phil. Mag. A* 72 (1995) 341.
- [93] M.J. Blackburn, in: R. Jaffee, N. Promisel (Eds.), *The Science, Technology and Application of Titanium*, Pergamon, 1970.
- [94] D. Schechtman, M.J. Blackburn, H.A. Lipsitt, *Metall. Trans. 5* (1974) 1373.
- [95] T. Kawabata, T. Kanai, O. Izumi, *Acta Metall.* 33 (1985) 1355.
- [96] S.C. Huang, E. Hall, in: C.T. Liu, A.I. Taub, N.S. Stoloff, C.C. Koch, *High-Temperature Ordered Intermetallic Alloys III*, Mat. Res. Soc. Symp. Proc., Vol. 133, Pittsburgh, PA, 1989, p. 133.
- [97] V. Vitek, *Prog. Mat. Sci.* 36 (1992) 1.
- [98] V. Paidar, *Mat. Sci. Eng. A* 192 (1995) 142.
- [99] G. Hug, A. Loiseau, P. Veysière, *Phil. Mag. A* 57 (1988) 499.
- [100] S.H. Whang, Y.D. Hahn, *Scripta Metall. Mater.* 24 (1990) 1679.
- [101] J.W. Christian, D.E. Laughlin, *Acta Metall.* 36 (1988) 1617.
- [102] M.H. Yoo, C.L. Fu, J.K. Lee, in: C.T. Liu, A.I. Taub, N.S. Stoloff, C.C. Koch, *High-Temperature Ordered Intermetallic Alloys III*, Mat. Res. Soc. Symp. Proc., Vol. 133, Pittsburgh, PA, 1989, p. 189.
- [103] K.J. Hemker, B. Viguier, M.J. Mills, *Mat. Sci. Eng. A* 164 (1993) 391.
- [104] M.H. Yoo, *J. Mater. Res.* 4 (1989) 50.
- [105] M.H. Yoo, C.L. Fu, J.K. Lee, in: M.H. Yoo, M. Wuttig (Eds.), *Twinning in Advanced Materials*, TMS, Warrendale, PA, 1994, p. 97.
- [106] B.F. Greenberg, *Phys. Status Solidi B* 55 (1973) 59.
- [107] C.L. Fu, M.H. Yoo, *Phil. Mag. Lett.* 62 (1990) 159.
- [108] M.H. Yoo, C.L. Fu, in: M. Yamaguchi, H. Fukutomi (Eds.), Proc. 3rd Intl. SAMPE Symp., Chiba, 1993, p. 1286.
- [109] T. Hanamura, M. Tanino, *J. Mat. Sci. Lett.* 8 (1989) 24.
- [110] Z.X. Li, J.Y. Kim, S.H. Whang, *Scripta Metall. Mater.* 25 (1991) 2595.
- [111] Y.G. Zhang, M.C. Chaturvedi, C.Q. Chen, *Phil. Mag. A* 67 (1993) 979.

- [112] B.H. Kear, H.G.E. Wilsdorf, *Trans. Metall. Soc. AIME* 224 (1962) 382.
- [113] Z.C. Li, S.H. Whang, *Mat. Sci. Eng.* A152 (1992) 18.
- [114] Z.X. Li, S.H. Whang, *Mat. Sci. Eng.* A152 (1992) 182.
- [115] S. Siram, V.K. Vasudevan, D.M. Dimiduk, in: J.A. Horton, I. Baker, S. Hanada, R.D. Noebe, D.S. Schwartz (Eds.), *High-Temperature Ordered Intermetallic Alloys VI*, Mat. Res. Soc. Symp. Proc., Vol. 364, Pittsburgh, PA, 1995, p. 647.
- [116] V. Paidar, D.P. Pope, V. Vitek, *Acta Metall.* 32 (1984) 435.
- [117] P.B. Hirsch, *Phil. Mag. A* 74 (1996) 1019.
- [118] V.K. Vasudevan, M.A. Stucke, S.A. Court, H.L. Fraser, *Phil. Mag. Lett.* 59 (1989) 299.
- [119] G. Hug, P. Veysiére, in: U. Messerschmidt, F. Appel, J. Heydenreich, V. Schmidt (Eds.), *Electron Microscopy in Plasticity and Fracture Research, Physical Research*, Vol. 14, Berlin, Akademie-Verlag, 1990, p. 451.
- [120] B.J. Inkson, C.J. Humphreys, *Phil. Mag. Lett.* 71 (1995) 307.
- [121] G. Hug, A. Loiseau, A. Lasalmonie, *Phil. Mag. A* 54 (1986) 47.
- [122] J.P. Simmons, M.J. Mills, S.I. Rao, in: J.A. Horton, I. Baker, S. Hanada, R.D. Noebe, D.S. Schwartz (Eds.), *High-Temperature Ordered Intermetallic Alloys VI*, Mat. Res. Soc. Symp. Proc., Vol. 364, Pittsburgh, PA, 1995, p. 137.
- [123] J. Panova, D. Farkas, in: J.A. Horton, I. Baker, S. Hanada, R.D. Noebe, D.S. Schwartz (Eds.), *High-Temperature Ordered Intermetallic Alloys VI*, Mat. Res. Soc. Symp. Proc., Vol. 364, Pittsburgh, PA, 1995, p. 151.
- [124] J.P. Simmons, S.I. Rao, D.M. Dimiduk, in: I. Baker, R. Darolia, J.D. Whittenberger, M.H. Yoo (Eds.), *High-Temperature Ordered Intermetallic Alloys V*, Mat. Res. Soc. Symp. Proc., Vol. 288, Pittsburgh, PA, 1993, p. 335.
- [125] A. Grischkin, V. Vitek, in: J.A. Horton, I. Baker, S. Hanada, R.D. Noebe, D.S. Schwartz (Eds.), *High-Temperature Ordered Intermetallic Alloys VI*, Mat. Res. Soc. Symp. Proc., Vol. 364, Pittsburgh, PA, 1995, p. 145.
- [126] J.P. Simmons, S.I. Rao, D.M. Dimiduk, *Phil. Mag. A* 75 (1997) 1299.
- [127] S. Rao, C. Woodward, J. Simmons, D.M. Dimiduk, in: J.A. Horton, I. Baker, S. Hanada, R.D. Noebe, D.S. Schwartz (Eds.), *High-Temperature Ordered Intermetallic Alloys VI*, Mat. Res. Soc. Symp. Proc., Vol. 364, Pittsburgh, PA, 1995, p. 129.
- [128] C. Woodward, J.M. MacLaren, S.I. Rao, *J. Mater. Res.* 7 (1992) 1735.
- [129] C. Woodward, J.M. MacLaren, D.M. Dimiduk, in: I. Baker, R. Darolia, J.D. Whittenberger, M.H. Yoo (Eds.), *High-Temperature Ordered Intermetallic Alloys V*, Mat. Res. Soc. Symp. Proc., Vol. 288, Pittsburgh, PA, 1993, p. 171.
- [130] J.M.K. Wiezorek, C.J. Humphreys, *Scripta Metall. Mater.* 33 (1995) 451.
- [131] I. Phan, Thesis, University Paris, 1993.
- [132] B.A. Greenberg, V.I. Anisimov, Yu.N. Gornostirev, G.G. Taluts, *Scripta Metall.* 22 (1988) 859.
- [133] S.A. Court, V.K. Vasudevan, H.L. Fraser, *Phil. Mag. A* 61 (1990) 141.
- [134] P.A. Beaven, Th. Pfullmann, *J. Mater. Sci. Technol.* 10 (1994) 321.
- [135] H. Inui, K. Kishida, M. Misaki, M. Kobayashi, M. Shirai, M. Yamaguchi, *Phil. Mag. A* 72 (1995) 1609.
- [136] K.-F. Yao, H. Inui, K. Kishida, M. Yamaguchi, *Acta Metall. Mater.* 43 (1995) 1074.
- [137] S.M.L. Sastry, H.A. Lipsitt, in: H. Kimura, O. Iszumi (Eds.), *Titanium '80*, Metallurgical Society of AIME, Warrendale, PA, 1980, p. 1231.
- [138] S.C. Huang, E.L. Hall, *Metall. Trans. A* 22 (1991) 427.
- [139] J.Y. Kim, Y.D. Han, S.H. Whang, *Scripta Metall. Mater.* 25 (1991) 543.
- [140] W.T. Donlon, W.E. Dowling, J.E. Allison, in: Y.-W. Kim, R.R. Boyer (Eds.), *Microstructure/Property Relationships in Titanium Aluminide and Alloys*, TMS, Warrendale, PA, 1991, 75.
- [141] F. Appel, P.A. Beaven, R. Wagner, *Acta Metall. Mater.* 41 (1993) 1721.
- [142] W. Wunderlich, Th. Kremser, G. Frommeyer, *Acta Metall. Mater.* 41 (1993) 1791.
- [143] R.K. Ham, *Phil. Mag.* 6 (1961) 1183.
- [144] J.M.K. Wiezorek, P.M. DeLuca, M.J. Mills, H.L. Fraser, *Phil. Mag. Lett.* 75 (1997) 271.
- [145] S. Wardle, I. Phan, G. Hug, *Phil. Mag. A* 67 (1993) 497.
- [146] Y.Q. Sun, P.M. Hazzledine, J.W. Christian, *Phil. Mag. A* 68 (1993) 471.
- [147] Y.Y. Zhang, M. Chaturvedi, *Phil. Mag. A* 68 (1993) 915.
- [148] M. Lonbradon, R. Bonnet, J.M. Pénisson, *Phil. Mag. A* 72 (1995) 1381.
- [149] J.W. Christian, S. Mahajan, *Prog. Mat. Sci.* 39 (1995) 1.
- [150] F. Appel, R. Wagner, in: M.H. Yoo, M. Wuttig (Eds.), *Twinning in Advanced Materials*, TMS, Warrendale, PA, 1994, p. 317.
- [151] F. Appel, U. Lorenz, U. Spaska, R. Wagner, in: H. Oikawa, K. Maruyama, S. Takeuchi, M. Yamaguchi (Eds.), *Strength of Materials*, Proc. ICSMA 10, The Japan Institute of Metals, Sendai, 1994, p. 341.
- [152] F. Appel, R. Wagner, in: Y.-W. Kim, R. Wagner, M. Yamaguchi (Eds.), *Gamma Titanium Aluminides*, TMS, Warrendale PA, 1995, p. 231.
- [153] J. Seeger, H. Mecking, *Scripta Metall. Mater.* 29 (1993) 13.
- [154] H. Mecking, Ch. Hartig, U.F. Kocks, *Acta Mater.* 44 (1996) 1309.
- [155] F. Appel, U. Christoph, R. Wagner, in: S.P. Murarka, K. Rose, T. Ohmi, S. Seidel (Eds.), *Interface Control of Electrical, Chemical and Mechanical Properties*, Mater. Res. Soc. Symp. Proc., Vol. 318, Pittsburgh, PA, 1994, p. 691.

- [156] B. Viguier, M. Cieslar, K.J. Hemker, J.L. Martin, in: J.A. Horton, I. Baker, S. Hanada, R.D. Noebe, D.S. Schwartz (Eds.), High-Temperature Ordered Intermetallic Alloys VI, Mat. Res. Soc. Symp. Proc., Vol. 364, Pittsburgh, PA, 1995, p. 653.
- [157] B.K. Kad, H.L. Fraser, Phil. Mag. A 69 (1994) 689.
- [158] S.R. Singh, J.M. Howe, Phil. Mag. Lett. 65 (1992) 233.
- [159] G. Chen, J. Wang, L. Zhang, H. Ye, Acta Metall. Sinica 8 (1995) 273.
- [160] E. Abe, S. Kajiwara, T. Kumagai, N. Nakamura, Phil. Mag. A 75 (1997) 975.
- [161] G. Schöck, Phys. Status Solidi 8 (1965) 499.
- [162] F. Appel, R. Wagner, Phys. Scripta 49T (1993) 387.
- [163] F. Appel, U. Lorenz, M. Oehring, U. Sparka, R. Wagner, Mat. Sci. Eng., A 233 (1997) 1.
- [164] J. Paul, F. Appel, R. Wagner, Acta Mater., in press.
- [165] R.E. Schafrik, Metall. Trans. 8A (1977) 1003.
- [166] M.A. Morris, T. Lipe, Scripta Metall. Mater. 31 (1994) 689.
- [167] F.R.N. Nabarro, Z.S. Bassinski, D. Holt, Adv. Phys. 13 (1964) 193.
- [168] Y.-W. Kim, in: M. Yamaguchi, H. Fukutomi (Eds.), Proc. 3rd. Intl. SAMPE Symp., Chiba, 1993, p. 1310.
- [169] J. Friedel, Dislocations, Pergamon, Oxford, 1967.
- [170] P.G. McCormick, Acta Metall. 20 (1972) 351.
- [171] A.H. Cottrell, B.A. Bilby, Proc. Phys. Soc. London, Sect. A 62 (1949) 49.
- [172] A. Kalk, Ch. Schwink, Phil. Mag. A 72 (1995) 315.
- [173] M.A. Morris, T. Lipe, D.G. Morris, Scripta Mater. 34 (1996) 1337.
- [174] S. Kroll, H. Mehrer, N. Stolwijk, Ch. Herzig, R. Rosenkranz, G. Frommeyer, Z. Metallkd. 83 (1992) 591.
- [175] P. Moine, J.P. Eymery, P. Grosbas, Phys. Status Solidi B 46 (1971) 177.
- [176] J.J. Gilman, W.G. Johnston, Solid State Phys. 13 (1962) 147.
- [177] J. Bardeen, C. Herring, in: Imperfections in Nearly Perfect Crystals, Wiley, New York, 1952, p. 261.
- [178] J.P. Hirth, J. Lothe, Theory of Dislocations, 2nd edn., Krieger Publishing, Malabar, 1992.
- [179] B. Viguier, J. Bonneville, K.J. Hemker, J.-L. Martin, in: J.A. Horton, I. Baker, S. Hanada, R.D. Noebe, D.S. Schwartz (Eds.), High-Temperature Ordered Intermetallic Alloys VI, Mat. Res. Soc. Symp. Proc., Vol. 364, Pittsburgh, PA, 1995, p. 629.
- [180] B. Viguier, K.J. Hemker, J. Bonneville, F. Louchet, J.-L. Martin, Phil. Mag. A 71 (1995) 1295.
- [181] J.A. Graves, L.A. Bendersky, F.S. Biancaniello, J.H. Perepezko, W.J. Boettger, Mat. Sci. Eng. 98 (1988) 265.
- [182] J.C. Mishurda, J.H. Perepezko, in: Y.-W. Kim, R.R. Boyer (Eds.), Microstructure/Property Relationships in Titanium Aluminides and Alloys, TMS, Warrendale, PA, 1991, Vol. 3, p. 30.
- [183] S.A. Court, J.P.A. Lövander, M.A. Stucke, P. Kurath, H.L. Fraser, in: C.T. Liu, A.J. Taub, N.S. Stoloff, C.C. Koch (Eds.), High-Temperature Ordered Intermetallic Alloys III, Mat. Res. Soc. Symp. Proc., Vol. 133, Pittsburgh, PA, 1989, p. 675.
- [184] G.J. Mahon, J.M. Howe, Metall. Trans. A 8 (1990) 199.
- [185] L. Zhao, K. Tangri, Acta Metall. Mater. 39 (1991) 2209.
- [186] L. Zhao, K. Tangri, Phil. Mag. A 64 (1991) 361.
- [187] H. Inui, A. Nakamura, M.H. Oh, M. Yamaguchi, Ultramicroscopy 39 (1991) 268.
- [188] B.K. Kad, P.M. Hazzledine, Phil. Mag. Lett. 66 (1992) 133.
- [189] S.R. Singh, J.M. Howe, Phil. Mag. A 66 (1992) 739.
- [190] L.L. He, H.Q. Ye, X.G. Ning, M.Z. Cao, D. Han, Phil. Mag. A 67 (1993) 1161.
- [191] F.C. Frank, J.H. van der Merwe, Proc. R. Soc. London, Ser. A 198 (1949) 216.
- [192] D.M. Dimiduk, Y. Sun, P. Hazzledine, in: J.A. Horton, I. Baker, S. Hanada, R.D. Noebe, D.S. Schwartz (Eds.), High-Temperature Ordered Intermetallic Alloys VI, Mat. Res. Soc. Symp. Proc., Vol. 364, Pittsburgh, PA, 1995, p. 599.
- [193] G. DeWitt, J.S. Koehler, Phys. Rev. 116 (1959) 1113.
- [194] P.M. Hazzledine, B.K. Kad, H.L. Fraser, D.M. Dimiduk, MRS Symp. 273 (1992) 81.
- [195] M.H. Yoo, C.L. Fu, J.K. Lee, J. Phys. III 1 (1991) 1065.
- [196] S.R. Singh, J.M. Howe, Scripta Metall. Mater. 25 (1991) 485.
- [197] M.H. Yoo, C.L. Fu, Metall. Trans. A, 1997, in press.
- [198] S. Farenc, A. Coniou, A. Courret, Phil. Mag. A 67 (1993) 172.
- [199] Z. Jin, T.R. Bieler, Phil. Mag. A 71 (1995) 925.
- [200] A. Bartels, H. Mecking, in: C.T. Liu, et al. (Eds.), Ordered Intermetallics—Physical Metallurgy and Mechanical Behavior, Kluwer Academic Publishers, 1992, p. 633.
- [201] Y. Minonishi, Phil. Mag. A 63 (1991) 1085.
- [202] Y. Umakoshi, T. Nakano, T. Takenaka, K. Sumimoto, T. Yamane, Acta Metall. Mater. 41 (1993) 1149.
- [203] H. Inui, Y. Toda, M. Yamaguchi, Phil. Mag. A 67 (1993) 1315.
- [204] H. Inui, Y. Toda, Y. Shirai, M. Yamaguchi, Phil. Mag. A 69 (1994) 1161.
- [205] J.C.M. Li, Y.T. Chou, Met. Trans. 1 (1970) 1145.
- [206] Y.Q. Sun, in: C.C. Koch, C.T. Liu, N.S. Stoloff, A. Wanner (Eds.), High-Temperature Ordered Intermetallic Alloys VII, Mat. Res. Soc. Symp. Proc., Vol. 460, Pittsburgh, PA, 1997,

- [207] B.K. Kad, R.J. Asaro, *Phil. Mag. A* 75 (1997) 87.
- [208] T. Kawabata, T. Tamura, O. Izumi, in: C.T. Liu, A.I. Taub, N.S. Stoloff, C.C. Koch (Eds.), *High-Temperature Ordered Intermetallic Alloys III*, Mat. Res. Soc. Symp. Proc., Vol. 133, Pittsburgh, PA, 1989, p. 330.
- [209] Y. Zheng, L. Zhao, K. Tangri, *Scripta Metall. Mater.*, 1992, p. 222.
- [210] C.M. Sabinash, S.M.L. Sastry, K.L. Jerina, *Scripta Metall. Mater.* 32 (1995) 1381.
- [211] G. Chen, W. Zhang, Y. Wang, J. Wang, Z. Sun, in: R. Darolia, J.J. Lewandowski, C.T. Liu, P.L. Martin, D.B. Miracle, M.V. Nathal (Eds.), *Structural Intermetallics*, TMS, Warrendale, PA, 1993, p. 318.
- [212] K.D. Hahn, S.H. Whang, in: C.T. Liu, A.I. Taub, N.S. Stoloff, C.C. Koch (Eds.), *High-Temperature Ordered Intermetallic Alloys III*, Mat. Res. Soc. Symp. Proc., Vol. 133, Pittsburgh, PA, 1989, p. 385.
- [213] E. Mohandas, P.A. Beaven, *Scripta Metall. Mater.* 25 (1991) 2023.
- [214] Y. Makino, *Intermetallics* 4 (1996) 11.
- [215] A. Denquin, S. Naka, A. Huguet, A. Menand, *Scripta Metall. Mater.* 28 (1993) 1131.
- [216] T. Kawabata, T. Abumiya, O. Izumi, *Acta Metall. Mater.* 40 (1992) 2557.
- [217] B.K. Kad, H.L. Fraser, *Phil. Mag. Lett.* 70 (1994) 211.
- [218] W.H. Tian, T. Sano, M. Nemoto, *Phil. Mag. A* 68 (1993) 965.
- [219] B.D. Worth, J.W. Jones, J.E. Allison, *Metall. Mater. Trans. A*, 26, 1995, 2947 and 2961.
- [220] D.E. Larsen, *Mater. Res. Soc. Symp. Proc.* 194 (1990) 285.
- [221] P.J. Maziasz, R.V. Ramanuyan, C.T. Liu, J.L. Wright, *Intermetallics* 5 (1997) 83.
- [222] D.S. Schwartz, D.S. Shih, in: J.A. Horton, I. Baker, S. Hanada, R.D. Noebe, D.S. Schwartz (Eds.), *High-Temperature Ordered Intermetallic Alloys VI*, Mat. Res. Soc. Symp. Proc., Vol. 364, Pittsburgh, PA, 1995, p. 787.
- [223] B. Inkson, C.B. Boothroyd, C.J. Humphreys, *Acta Metall. Mater.* 43 (1995) 1429.
- [224] A.B. Godfrey, M.H. Loretto, *Intermetallics* 4 (1996) 47.
- [225] S. Tsuyama, S. Mitao, K. Minakawa, *Mater. Sci. Eng. A* 153 (1992) 451.
- [226] T. Noda, M. Okabe, S. Isobe, M. Sayashi, *Mater. Sci. Eng. A* 192/193 (1995) 774.
- [227] F. Appel, *Phil. Mag. A* 63 (1991) 71.
- [228] F. Appel, *Phys. Status Solidi A* 116 (1989) 153.
- [229] B.A. Greenberg, *Phys. Status Solidi* 42 (1970) 459.
- [230] B.A. Greenberg, Y.N. Gornostirev, *Scripta Metall.* 22 (1988) 853.
- [231] B.A. Greenberg, O.V. Antonova, V.N. Indenbaum, L.E. Karkina, A.B. Notkin, M.V. Ponomarev, *Acta Metall. Mater.* 39 (1991) 233.
- [232] F. Kroupa, *Acta Metall.* 14 (1966) 60.
- [233] A.G. Evans, R.D. Rawlings, *Phys. Status Solidi* 34 (1969) 9.
- [234] T. Kawabata, T. Abuyima, O. Izumi, *Acta Metall. Mater.* 40 (1992) 2557.
- [235] E. Orowan, in *Symposium on Internal Stresses*, published by Inst. of Metals, London, 1948, p. 451.
- [236] M.F. Ashby, in: A.S. Argon (Ed.), *Physics of Strength and Plasticity*, MIT, Cambridge, MA, 1969, p. 113.
- [237] L.M. Brown, W.M. Stobbs, *Phil. Mag.* 23 (1971) 1185.
- [238] L.M. Brown, W.M. Stobbs, *Phil. Mag.* 23 (1971) 1201.
- [239] H. Oikawa, K. Maruyama, in: Y.-W. Kim, R. Wagner, M. Yamaguchi (Eds.), *Gamma Titanium Aluminides*, TMS, Warrendale, PA, 1995, p. 919.
- [240] J.S. Huang, Y.-W. Kim, *Scripta Metall. Mater.* 25 (1991) 1901.
- [241] M. Es-Souni, A. Bartels, R. Wagner, *Mat. Sci. Eng. A* 192/193 (1995) 698.
- [242] M. Es-Souni, A. Bartels, R. Wagner, *Mat. Sci. Eng. A* 171 (1993) 127.
- [243] M. Es-Souni, A. Bartels, R. Wagner, *Acta Metall. Mater.* 43 (1995) 153.
- [244] J. Beddoes, W. Wallace, L. Zhao, *Int. Mat. Rev.* 40 (1995) 197.
- [245] W.E. Dowling, B.D. Worth, J.E. Allison, J.W. Jones, in: Y.-W. Kim, R.R. Boyer (Eds.), *Titanium Aluminides and Alloys*, TMS, Warrendale, PA, 1990, p. 123.
- [246] G. Viswanathan, V.K. Vasudevan in: I. Baker, R. Darolia, J.D. Whittenberger, M.H. Yoo (Eds.), *High-Temperature Ordered Intermetallic Alloys V*, Mat. Res. Soc. Symp. Proc., Vol. 288, Pittsburgh, PA, 1993, p. 787.
- [247] R.W. Hayes, B. London, *Acta Metall. Mater.* 40 (1992) 2167.
- [248] S.W. Schwenker, Y.-W. Kim, in: Y.-W. Kim, R. Wagner, M. Yamaguchi (Eds.), *Gamma Titanium Aluminides*, TMS, Warrendale, PA, 1995, p. 985.
- [249] T. Tsujimoto, K. Hashimoto, in: C.T. Liu, A.I. Taub, N.S. Stoloff, C.C. Koch (Eds.), *High-Temperature Ordered Intermetallic Alloys III*, Mat. Res. Soc. Symp. Proc., Vol. 133, Pittsburgh, PA, 1989, p. 391.
- [250] H. Deve, A.G. Evans, *Acta Metall. Mater.* 39 (1991) 1171.
- [251] M. Oehring, P.J. Ennis, F. Appel, R. Wagner, in: C.C. Koch, N.S. Stoloff, C.T. Liu, A. Wanner (Eds.), *High-Temperature Ordered Intermetallic Alloys VII*, Mat. Res. Soc. Symp. Proc., Vol. 460, Pittsburgh, PA, 1997, p. 257.
- [252] R.V. Ramanujan, P.J. Maziasz, C.T. Liu, *Acta Mater.* 44 (1996) 2611.
- [253] Z. Jin, Th.R. Bieler, *Scripta Metall. Mater.* 27 (1992) 1301.
- [254] R.W. Hayes, P.L. Martin, in: Y.-W. Kim, R. Wagner, M. Yamaguchi (Eds.), *Gamma Titanium Aluminides*, TMS, Warrendale, PA, 1995, p. 939.
- [255] G.B. Gibbs, *Phys. Status Solidi* 10 (1995) 507.

- [256] F. Appel, R. Wagner, in: D.J. Smith, R.J. Hamers (Eds.), *Atomic Resolution Microscopy of Surfaces and Interfaces*, Mat. Res. Soc. Symp. Proc., Vol. 466, Pittsburgh, PA, 1997, p. 145.
- [257] D. McLean, *Prog. Phys.* 29 (1966) 1.
- [258] A.K. Mukherjee, J.E. Bird, J.E. Dorn, *Trans. ASM* 62 (1969) 155.
- [259] M.F. Bartholomeusz, Q. Yang, J.A. Wert, *Scripta Metall. Mater.* 29 (1993) 389.
- [260] J.N. Wang, A.J. Schatz, T.G. Nieh, C.T. Liu, V.K. Sikka, D. Clemens, in: Y.-W. Kim, R. Wagner, M. Yamaguchi (Eds.), *Gamma Titanium Aluminides*, TMS, Warrendale, PA, 1995, p. 949.
- [261] D.A. Wheeler, B. London, D.E. Larsen, *Scripta Metall. Mater.* 26 (1992) 939.
- [262] R.W. Hayes, P.A. McQuay, *Scripta Metall. Mater.* 30 (1994) 259.
- [263] J. Wolfenstine, G. Gonzales, *Mater. Lett.* 18 (1994) 286.
- [264] M.H. Yoo, C.L. Fu, *Mater. Sci. Eng.* A153 (1992) 470.
- [265] H. Liebowitz, *Fracture*, Vol. 2, Mathematical Fundamentals, Academic Press, New York, 1968.